MODELING OF NANOSCALE ELECTRICAL JUNCTIONS AND ELECTRICAL CONTACTS

By

Sneha Banerjee

A DISSERTATION

Submitted to
Michigan State University
in partial fulfillment of the requirements
for the degree of

Electrical Engineering – Doctor of Philosophy

2021

ABSTRACT

MODELING OF NANOSCALE ELECTRICAL JUNCTIONS AND ELECTRICAL CONTACTS

By

Sneha Banerjee

Nano-scale electrical contacts are essential for next generation electronics. Based on the materials of the contact members and the interfacial layers, these junctions can be of ohmic, Schottky or tunneling type. Nonuniform current distribution and current crowding across electrical contacts lead to nonuniform heat deposition, formation of local thermal hotspots, aggravation of electromigration, and in the worst scenario, lead to thermal runaway and breakdown of the device. Contact resistance, on the other hand, severely restricts the current flow, and affects the overall device properties. Devices based on thin film junctions, nanotubes or nanowires, and two-dimensional (2D) materials are especially sensitive to the current transport at electrical contacts, due to their reduced dimensions and increased geometrical confinement for the current flow. The goal of this thesis is to develop theoretical models to understand, improve, and control current transport and to reduce contact resistance in nanoscale electrical contacts.

First, we study the current density-voltage $(J-V)$ characteristics of dissimilar metal-insulator-metal (MIM) nanoscale tunneling junctions using a self-consistent quantum model. Tunneling type contacts are ubiquitous as they can be formed when a thin insulator layer or gap exists between two contacting members. Our model includes electron emissions from both the cathode and anode, and the effects of image charge potential, space charge and exchange correlation potential. The $J-V$ curves span three regimes: direct tunneling, field emission, and space-charge-limited regime. Unlike similar MIM junctions, the $J-V$ curves are polarity dependent. The forward and reverse bias $J-V$ curves and their crossover behaviors are examined

in detail for various regimes, over a wide range of material properties. It is found that the asymmetry between the current density profiles increases with the work function difference between the electrodes, insulator layer thickness, and relative permittivity of the insulator. This asymmetry is profound in the field emission regime and is insignificant in the direct tunneling, and space charge limited regimes.

Next, we study the current distribution and contact resistance in ohmic, tunneling and two-dimensional (2D) material-based Schottky contacts. We modify the standard transmission line model (TLM) to include the effects of spatially varying specific contact resistivity ρ_c along the contact length. Both Cartesian and circular (or annular) contacts are analyzed. The local voltage-dependent ρ_c along the contact length is calculated self-consistently by solving the lumped circuit TLM equations coupled with the quantum tunneling model for MIM junctions, or the thermionic emission current injection model for 2D materials. We find that current distribution and contact resistance depend strongly on input voltage, contact dimension and geometry, and material properties. We also propose to reduce contact resistance in 2D-material-based electrical contacts by roughness engineering of the contact interfaces. The results for ohmic contact are verified with finite element method (FEM) based simulations, and the 2D-material based calculations are validated with existing theory and experiments.

We further extend this work and demonstrate a method to mitigate current crowding, by engineering the interface layer properties and geometry. We find that current steering and redistribution can be realized by strategically designing the specific contact resistivity ρ_c along the contact length. We also find that introducing a nanometer scale thin insulating tunneling gap between highly conductive contact members can greatly reduce current crowding while maintaining similar total contact resistance.

To Maa and Baba: Lakshmi and Swapan Banerjee

ACKNOWLEDGEMENTS

It would not have been possible to write this doctoral thesis without the help and support of the kind people around me. I would like to show my gratitude here.

Above all, I would like to thank my parents for their constant support, patience, and encouragement. Their love, care, and uplifting words have always motivated me to move forward. My grateful hugs to all my cousins, uncles, and aunts who are undoubtedly the warmest people on earth.

This thesis would not have been possible without the help, support, patience, advice, and guidance of my advisor, Professor Peng Zhang. During the four years of my graduate study at Michigan State University, Prof. Zhang has always been there for me whenever I needed help. I learned a lot from his mentorship. His advice has been invaluable to me on both academic and personal levels. I convey my sincerest gratitude to him.

I would also like to thank my doctoral committee members Prof. Verboncoeur, Dr. Luginsland, Prof. Li, and Prof. Fan for their valuable suggestions and time. I thank the faculty and administrative members of the Electrical Engineering department, for all the help and support they provided. I thank my colleagues (my academic family at MSU) Yi, Asif, Patrick, Janez, Yang, Yangyang and Deqi. I could not have asked for a more supportive group. My special thanks to Yi and Asif for taking the courses with me, doing the homeworks and preparing for the exams together, and most importantly, for making my journey joyful. I also thank Xenofon and Tanvi from the Electrical Engineering department, for their help with homeworks, Qualifier A preparation, and for being wonderful friends.

Finally, I thank all my friends who have supported me, believed in me, fed me, reminded me to file tax returns, celebrated the small achievements with me, and listened to my complaints (about life). I thank – Moyukh, Sampa, Ankita, Lahar, Srivalli, Gouree, Apoorva, Renu, Bharath, Abhijnan, Sudhakar, Abhiroop, Aditya, Affan, Sushant, Shayonee, Chirag, Pradyumna, Anson, Sunanda, Haritha, and Vivek.

This work has been supported by the Air Force Office of Scientific Research (AFOSR) YIP Award No. FA9550-18-1-0061. The Michigan Institute for Plasma Science and Engineering Fellowship (MIPSE) Fellowship, and the Michigan State University's Graduate Writing Fellowship are also acknowledged.

TABLE OF CONTENTS

LIST OF TABLES

LIST OF FIGURES

CHAPTER 1

INTRODUCTION

Nanoscale electrical junctions are prevalent in a diverse set of electronic devices. They are naturally formed in transistors [1], [2], scanning tunneling microscopes [3], [4], thin film contacts, and two-dimensional (2D) material, nanowire, nanofiber, or nanorod based novel devices [5]–[7], as shown in Figures 1.1 and 1.2 below. Based on the materials of the contact members and the interfacial layers, these junctions can be of ohmic, Schottky or tunneling type. Tunneling type contacts are especially common where the contacting members are separated by very thin insulating layers [8]–[10]. The objective of this work, and the motivation behind, are discussed in detail in the following section.

1.1 Motivation and Background

This thesis theoretically studies the current transport in nano-scale electrical junctions and electrical contacts. First, we focus on the quantum tunneling induced electron transport in metal-insulator-metal junctions. Next, we study the effects and parametric dependence of current distribution and contact resistance for ohmic, tunneling, and Schottky type contacts. The objective is to better characterize electrical contacts and to optimize the current flow in such electrical junctions by improving controllability.

1.1.1 Quantum tunneling in metal-insulator-metal junctions

Quantum tunneling phenomenon, which becomes important in nano scale junctions and circuits, imposes some serious challenges to the modern-day electronics. Due to the ever-increasing demands for physical scaling down, electrodes in the scale of 10 nm or sub-10 nm are common these days in silicon industry [1], [2], [11], [12]. The circuits in this range are so small that quantum mechanical effects become critical and cause device malfunction. On the other hand, the charge transport through tunnel junctions are utilized to develop novel devices that offer several advantages over the shortcomings of scaling. Next-generation transistors, such as, tunnel field-effect transistors (TFETs) [13], [14], single electron transistors (SETs) [15]–[18], and graphene-based field effect transistors, rely on quantum tunneling for their operation. TFETs, which outperform the traditional Si transistors at low power and can further extend the Moor's law, switch by modulating the quantum tunneling current [14]. Recently, researchers were able to develop a highly sensitive detector for terahertz (THz) frequency utilizing the quantum tunneling effect in a graphene based TFET [13], [19]. Ultrasensitive detectors based on SETs are also attracting great attention [20]–[22]. Nanoscale devices based on quantum tunneling principles are expected to become increasingly important in future electronics industry. To enable the practical use of such devices, a comprehensive study of the quantum current transport is necessary.

Tunneling resistivity is one of the major obstacles for the development of low dimensional material-based devices. The performance of transistors based on carbon nanotubes (CNTs), carbon nanofibers (CNFs), and graphene greatly depend on the tunneling current. In these transistors, parallel arrays of nanowires or dense networks of nanotubes (c.f. Fig. 1.1) are used for the channel material. The current transport is critically dependent upon the tunneling resistivity between these nanostructures [8], [23]–[25]. An example is shown in Fig. 1.1 for illustration. Using carbon nanotube network channels, Tang and colleagues fabricated high-speed flexible CMOS ICs that offer sub-10 ns stage delays [26]. They found on-state current of the transistors and thus the speed of the device, relied on electron tunneling between the nanotubes. To realize the excellent electrical properties of novel low-dimensional materials on the circuit level and to develop flexible electronics based on them, contact engineering is crucial [27].

Tunneling electron emission through vacuum nanogap is also common in miniaturized vacuum and plasma electronic devices [28]–[32] and plasmonic nanogaps [33]. Many new technologies combine the advantages of ballistic transport through vacuum with the scalability, reliability, and low cost of silicon technology [28]. Study of the tunneling induced charge transport across nanometer length scale is critical for the development of such technologies.

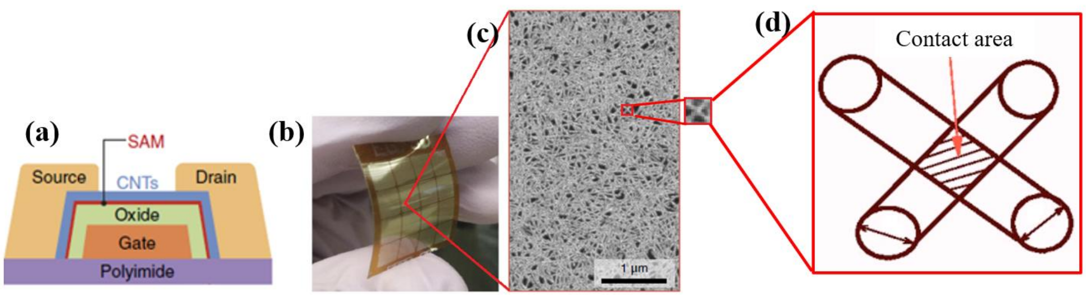

Figure 1.1 High-speed transistors circuit made from carbon nanotubes. (a) Structure of a carbon nanotube transistor. CNTs, carbon nanotubes; SAM, self-assembled monolayer. (b) Optical image of nanotube transistors circuit fabricated on a flexible polyimide substrate, and (c) a scanning electron microscopy image of the nanotube thin film used in these transistors and circuits. [26] (d) A typical CNT-CNT contact present in the thin film.

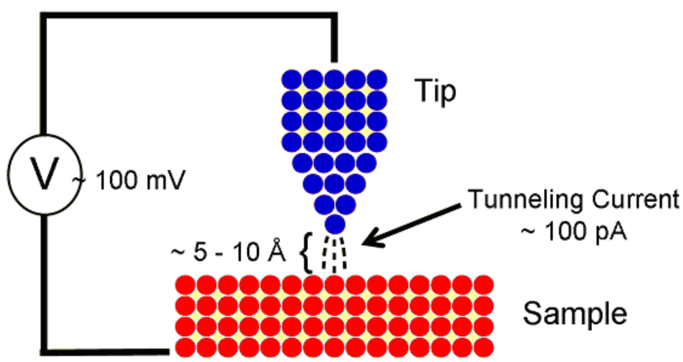

Figure 1.2 A schematic scanning tunneling microscope setup. When a tip is brought several angstroms away from a sample and a voltage is applied between them, a very small current flows between the last atom of the tip and the sample. As the tip is scanned over the surface, image of the surface is recorded with atomic spatial resolution [34].

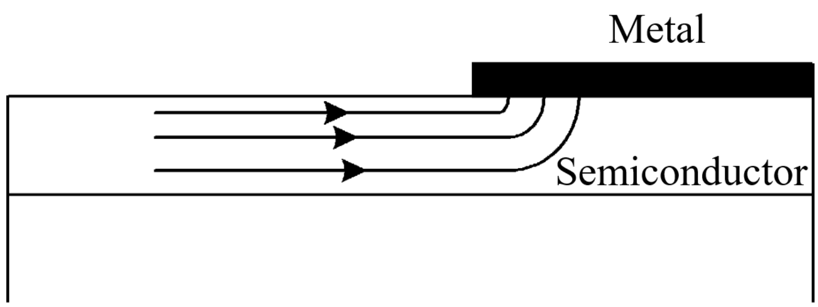

Figure 1.3 Current crowding at a metal-semiconductor contact.

1.1.2 Current distribution and contact resistance

Current flow in an electrical circuit is usually non-homogeneous. Localized increase of current density or the current crowding effect [35]–[38] is a serious and persistent problem in the electronics industry. Current crowds near a bend or a constriction, and it is especially strong at the vicinity of contact edges [39]–[43]. An example of current crowding in a typical metal-semiconductor contact is shown in Fig. 1.3. Due to the resistivity mismatch between the contact members, the current transport is confined only near the front edge of the contact structure. Since Joule heating is proportional to the square of current density [44], current crowding leads to non-uniform heat generation in the contact area. On the other hand, the excessive amount of Joule heating deposited at the contact region because of the large contact resistance is another critical concern of very-large-scale-integrated (VLSI) circuit engineers [45]–[47]. There are various factors that can increase the total contact resistance, such as, formation of oxide layers between the contact members, dielectric coating of the electrodes, presence of surface roughness, etc. The individual or combined effects of current crowding, non-uniform Joule heating, and contact resistance are responsible for about 40% of all electrical/electronics failure, ranging from small scale modern consumer electronics, like, hand-held or wearable devices, personal computers etc.

to large scale space vehicles, particle accelerators, nuclear facilities, and military systems [28], [43], [48]–[54].

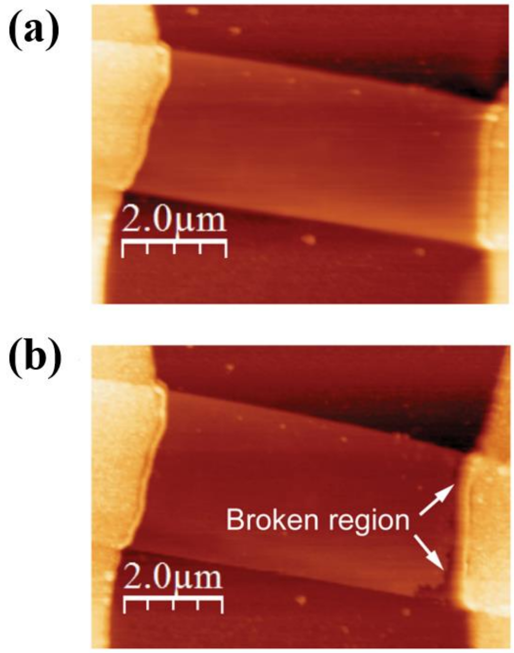

Figure 1.4 Atomic Force Microscopy (AFM) topography images of a device before (a) and after (b) device failure. Current crowding induced thermal hotspot in two-dimensional black-phosphorus field-effect transistors. [55]

In modern semiconductor industry, the contact problems have become more prominent nowadays with the growing demands for advanced computation, high speed, and high packing density. 2D materials, such as, molybdenum disulfide (MoS_2), black phosphorus, boron nitride, graphene have been demonstrated to be excellent channel materials for ultrathin field-effect transistors [2], [31], [55], [56]. However, the current crowding effect and the unusually high contact resistance at the 3D metal and the 2D semiconductor interfaces [55]–[58] hinder the development of such electronics. Figure 1.4 shows current crowding induced break down in two-dimensional black-phosphorus field-effect transistors [55].

To reduce cost and enhance performance, engineers are developing technologies that are shifting towards three-dimensional (3D) integrated circuits (ICs), where the dies are stacked on top of each other [51]. Both horizontal and vertical interconnects are used. In such densely packed structures, the power density is significantly increased, albeit with limited choices of dissipation options. Heat dissipation is especially difficult for mobile units [51]. This leads to increase of the circuit temperature. Current crowding makes the situation worse by heating the junction nonuniformly. The thermal gradient at the contact area may result in thermal crosstalk and thermomigration. Interconnect junctions in 3D ICs, such as, flip chip joints and solder bumps, suffer from electromigration [51], [59]–[63] which moves atoms based on the flow of current through a material. In high current density region, the generated heat breaks atoms from the material repeatedly and move them from their initial locations. This creates both 'vacancies' (Fig. 1.5) and 'deposits' (Fig. 1.6). The vacancies or voids can grow and eventually break circuit connections resulting in open-circuits, while the deposits or hillocks can grow and eventually close circuit connections resulting in short-circuits. Divergences in atomic flux, induced by current crowding, accelerates this process. These issues cause serious safety and reliability concerns [51], [63].

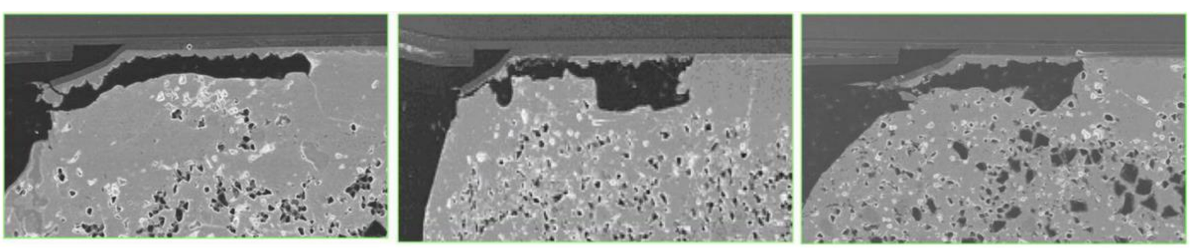

Figure 1.5 Enlarged scanning electron microscope (SEM) images of flip chip solder joints showing pancake-type of void formation due to current crowding induced electromigration. [51]

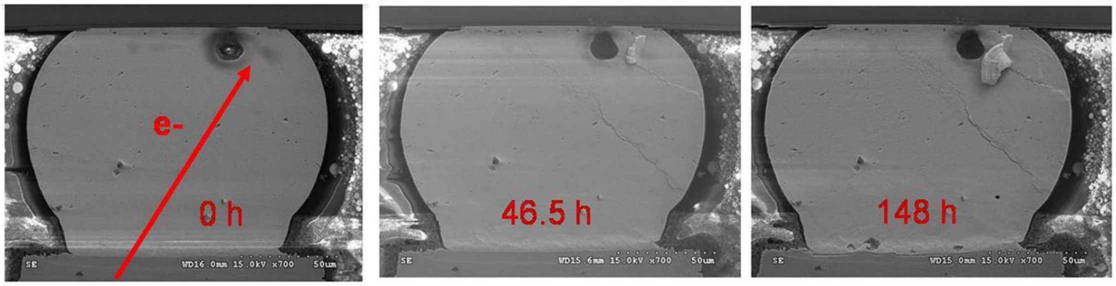

Figure 1.6 A set of three scanning electron microscope (SEM) images of the initiation and growth of a whisker at the upper right corner a solder joint as a result of current crowding induced electromigration. [51]

Furthermore, the combined effect of electromigration and Joule heating can lead to catastrophic burn-out type failure [51]. Localized void formation at the copper (Cu) interconnects leads to thinning of the conductor which increases the resistance and the corresponding Joule heating. Due to the high packing density and poor heat dissipation, the increased Joule heating increases the temperature, which in turn increases the electromigration rate. Electromigration, on the other hand, reduces the thickness of the electrode, further increasing the resistance and Joule heating. This positive feed-back causes thinning of Cu lines in the 3D integrated chips, builds up mechanical stress, and eventually, causes burn-out failure [51]. Failures due to "pancake-type" void formation and "whisker-type" growth formation are shown in Fig. 1.5 (Fig. 11 of Ref. [51]) and Fig. 1.6 (Fig. 12 of Ref. [51]), respectively.

In addition to electromigration, strong current crowding effect can also lead to localized overheating and formation of hotspots [55]. Several theoretical and experimental studies have found that the hotspots are usually formed at the contact edges. Figure 1.4 (Fig. 4 of Ref. [55]) shows a failed device with a broken region at the inner contact edge after a prolonged operation at high voltage. The failure is often caused by thermal runaway. The contact electrode's resistance typically increases with temperature which causes more heating of the junction, which further increases the junction temperature, in a positive feedback loop. If a circuit produces more heat than the heatsink can dissipate, then thermal hotspots are formed leading to component breakdown, or in the worst-case scenario, a small explosion [51]. In high power microwave sources and pulsed power systems, poor electrical contact also prevents efficient power coupling to the load [52], produces unwanted plasma [64], and in the worst-case scenario, damages the electrodes and circuits.

Therefore, a comprehensive and systematic modeling of the current transport and electrical contacts in nano scale electrical junctions is necessary to further advance modern electronics.

1.2 Prior Works

1.2.1 Quantum tunneling in metal-insulator-metal junctions

The work on quantum tunneling started as early as 1926, when Schrodinger published his landmark equation for wave function in quantum mechanics [65]. The same year, Wenzel, Kramers, and Brillouin developed a semiclassical method (WKB method) for finding approximations to the one-dimensional time independent Schrödinger equation [66], [67]. This WKB method is widely used to calculate transmission and reflection coefficients through a smooth and slowly varying potential barrier. In 1933 Sommerfeld and Bethe published theoretical study of tunneling in metal-insulator-metal (MIM) junctions for very low and high voltages using WKB approximation [68]. In 1935 Holm extended the theory to include intermediate voltages [69]. The challenge for this kind of study was to determine the actual shape of the potential barrier in the vacuum gap or insulator.

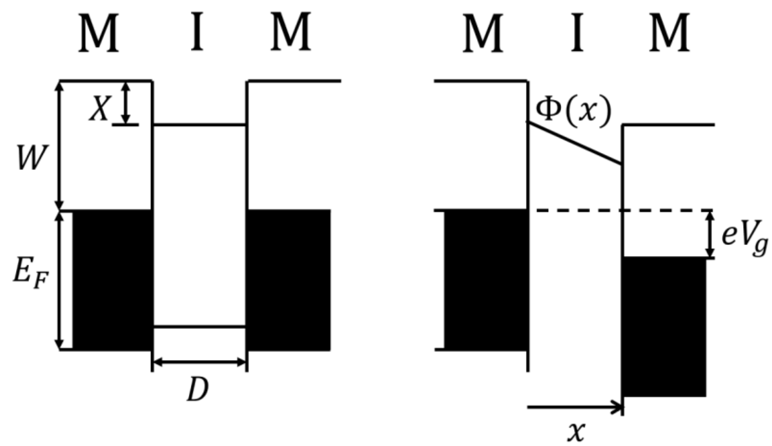

Figure 1.7 Sommerfeld and Bethe's rectangular potential barrier theory for metal-insulator-metal (MIM) junctions [68]. $\boldsymbol{V_g}$ **is the bias voltage,** $\boldsymbol{D}$ **is the insulator layer thickness,** $\boldsymbol{W}$ **is the work function of the metal electrodes,** $\boldsymbol{X}$ **is the electron affinity of the insulator,** $\boldsymbol{E_F}$ **is the Fermi level energy, and** $\boldsymbol{\Phi(x)}$ **is the potential barrier.**

Sommerfeld and Bethe first derived equations for the current density transmitted by a trapezoidal barrier $\Phi(x) = E_F + W - X + eV_g(x)$ (c.f. Fig. 1.7), where V_g is the bias voltage, D is the insulator layer thickness, W is the work function of the metal electrodes, X is the electron affinity of the insulator, and E_F is the Fermi level energy [68]. However, image charge potential rounds off the corners of a trapezoidal barrier and increases the flow of current between the electrodes. To obtain an analytic solution, Sommerfeld and Bethe approximated the barrier by a symmetric parabola. Later, Holm and Kirschstein, using the same method, improved upon the results of Sommerfeld and Bethe by using a symmetric parabola that was a closer fit to the potential barrier [69]. In 1963, Simmons modified the shape of the barrier and improved accuracy [9].

Tunneling effects between electrodes separated by thin insulating films have been studied extensively by Simmons [9], [70] in 1960s. His formulas have since been widely used for evaluating tunneling current in MIM junctions. From his study he concluded: a) tunneling current increases exponentially when gap distance D decreases, b) for low voltages, MIM junctions can be approximated as ohmic, c) tunneling current is polarity dependent for dissimilar electrodes. The tunneling current in Al-Al_2O_3-Al structures have been experimentally studied and evaluated using Simmons' theory [71]. Although widely used, Simmons' theory has some limitations: a) The formulas are derived by considering only the emission process from the electrodes, where the effects of image charge are considered, but the electron space charge potential and the electron exchange-correlation potential inside the insulator thin films are ignored. b) This model is reliable only in the low voltage regime for limited parameter space [10]. c) It fails to predict the maximum possible tunneling current in a metal-insulator-metal junction.

There are several theoretical [72]–[74] and experimental [75], [76] studies on space charge effects in a vacuum nanogap. Child-Langmuir (CL) law gives the space-charge limited current (SCLC) in a plane-parallel vacuum diode. This classical value for the limiting current can be exceeded by a large factor in nanoscale vacuum gap because of tunneling. The new limit is referred as the quantum CL (QCL) law [72], [73]. The effects of exchange correlation potential in a vacuum nanogap have also been studied systematically [77]. In 2015, a general scaling law for the quantum tunneling current in nano- and sub-nanoscale MIM junctions has been developed by self-consistently solving the coupled Schrödinger and Poisson equations [10]. Zhang's model [10] was formulated for similar electrodes. It includes the effects of space charge and exchange-correlation potential, as well as current emission from both electrodes. The current-voltage (J-V) characteristics has three distinct regimes: a) the direct tunneling regime, where it follows Simmons's formula [9], b) field emission regime, where it becomes close to Fowler–Nordheim law [78], and c) space charge limited (SCL) regime, where it approaches quantum Child–Langmuir law [72], [73].

This thesis extends Zhang's work to include the effects of dissimilar metal electrodes [79]. The rectification properties of such junctions have been studied for various materials and input parameters [79].

1.2.2 Contact resistance

Different theoretical models have been developed over time to characterize micro and nanoscale thin film-based contacts. In these thin-film contacts, the current flow lines bend sharply in the immediate vicinity of the contact edges [50]. Hall [80], [81] used conformal mapping technique to investigate the two-dimensional (2D) thin film resistance for various patterns in Cartesian geometry. Denhoff [82] studied the spreading resistance of a round thin film contact by solving Laplace equation. Zhang [50] provided extensive generalization of Hall's models on 2D Cartesian thin-film contacts including the effects of dissimilar materials. By using Fourier series analysis, Zhang and Lau [83] in 2010, derived simple analytical scaling laws for the total resistance for arbitrary values of dimensions and resistivities. The models were then extended to horizontal [39], [84], [85] and vertical [38] type thin film contacts. Current crowding has been comprehensively studied by calculating the current flow patterns [28], [37], [85]. Kennedy and Murley [86], in 1968, investigated the electrical properties of the diffused semiconductor resistor using a two-dimensional mathematical analysis. They calculated the constant voltage contours in the ohmic contact region of a diffused silicon resistor and found that only a small portion of the contact actively contributes to the electrical properties of the structure. The potential distribution is concentrated at the leading edge of the contact, resulting in extensive current crowding. They concluded that increasing the length of the ohmic contact has negligible influence on the current density at the metal-semiconductor interface.

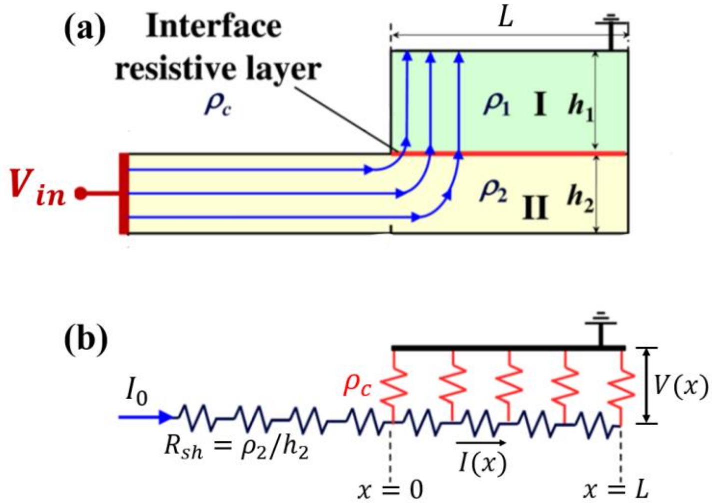

Figure 1.8 (a) Electrical contact and (b) its TLM. In (a), an infinitesimally thin resistive interface layer is sandwiched between Regions I and II. ρ_c is the specific contact resistivity. [84]

On the other hand, simple transmission line model (TLM) theory, in plenty of variant or extended forms, has been widely used for analyzing metal-semiconductor planar contacts. In 1969, Murrmann and Widmann [36] used a simple steady state TLM to characterize planar metal-semiconductor contacts. Although the formulation is simple, it can extract important contact characterization parameters, such as, contact resistance R_c in ohm, semiconductor sheet resistance beneath the contact R_{sh} in “ohm per square” (denoted by $\Omega/\square$), and specific contact resistivity ρ_c in Ω/cm^2, as shown in Fig. 1.8. $\rho_c = \frac{dV}{dJ_c}$ is an important parameter in contact characterization, where J_c is the contact current density. Berger [87], in 1972, provided a thorough characterization of contact resistance and contact resistivity. The governing equations of the structure shown in Fig. 1.8 b are:

$$\frac{dV}{dx} = -\frac{I(x)R_{sh}}{w}, \frac{dI}{dx} = \frac{V(x)}{\rho_c}w \tag{1.1}$$

where $V(x)$ and $I(x)$ are the voltage drop and current flowing along the semiconductor at x, w is the width or the transverse dimension of the contact. The solution to Eq. (1.1) is [35], [88],

$$V(x) = \frac{I_0\sqrt{\rho_c R_{sh}}}{w} \cosh\left[\frac{(L-x)}{L_T}\right] / \sinh\,(L/L_T), \tag{1.2}$$

where L is the contact length, w the contact width, and I_0 the current flowing into the contact, and $L_T = \sqrt{\rho_c/R_{sh}}$ is the transfer length.

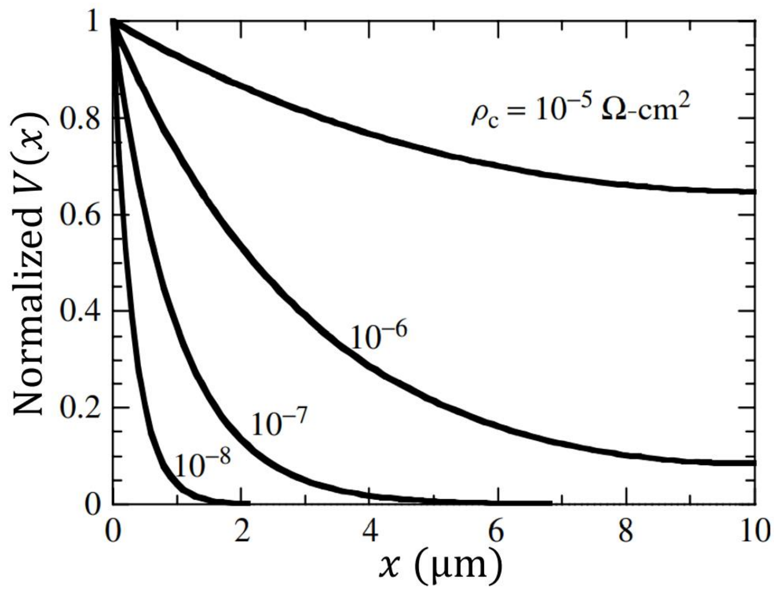

Figure 1.9 Normalized potential under a contact versus x as function of ρ_c, $L = 10$ μm and $R_{sh} = 10\ \Omega/\square$. [35]

The current transfer from semiconductor to metal takes place over L_T, indicating strong current crowding. Equation 1.2 is plotted in Fig. 1.9 (Fig. 3.15 of Ref. [35]). In 1980, Reeves extended the formulation for Cartesian contacts to circular contact structures [89]. In 1995, Reeves and Harrison [90] further extended the theory to alloyed ohmic contacts using a trilayer transmission line model (TTLM). TTLM [90]–[92] considers three layers (metal layer, alloyed semiconductor layer, and unalloyed semiconductor layer) and two interfaces between the three layers.

Although TLM theory is one of the most commonly used models to characterize planar contacts, allowing important contact parameters (ρ_c, R_{sh}, R_c) to be extracted or calculated, this simple model has some limitations: a) the sheet thickness of the contact material is assumed to be zero, forcing current flow to be one-dimensional, b) it is applicable only for planar ohmic contacts or contacts that can be approximated as ohmic, c) specific contact resistivity is assumed to be constant along the contact length. Various modification of this theory have been attempted to overcome some of the limitations.

a) *Overcoming zero sheet thickness limitation:* For the sake of simplicity, Overmeyer [93], in 1970, set $\rho_c = 0$ and calculated the current density in the contact area as a function of semiconductor layer thickness h_2 and contact length L. Later, the "zero sheet thickness" restriction was relaxed by Berger in his extended transmission line model (ETLM) with current still restricted to one dimensional flow [87]. Berger added a virtual specific contact resistivity of $0.19\,\rho_2 h_2$, which yields, $\rho_c' = \rho_c + 0.19\,\rho_2 h_2$, where ρ_2 is the resistivity and h_2 is the thickness of the semiconductor layer. This ETLM has been widely used in the literature [84], [94]. In 1986, Pimbley [95] extended Berger's idea and formulated a more sophisticated dual-level transmission line model (DLTLM). His method introduces two-dimensional characteristics to the standard TLM by postulating two parallel lines (at one-quarter and three-quarters of the semiconductor thickness) to carry the semiconductor current instead of just one. DLTLM produces around 12% corrections to the TLM with source resistivity, thickness, and specific contact resistivity typical of 1 μm technologies. In 2014, Zhang and Lau [84] did a comprehensive comparative study (c.f. Fig. 1.10) of contact resistance using exact field solution, TLM and ETLM for several geometric ratios and resistivity ratios. The solid, dashed, and dotted lines in Fig. 1.10 (Fig. 3 in Ref. [84]) are for field solution, TLM and ETLM, respectively. The ratio $\eta = \rho_c/\rho_2 h_2$ determines the parameter regime where the TLM theory can be used with good accuracy [87]. They found that TLM can be used to evaluate contact resistance if $\eta > 2$ and ETLM can be used when $\eta > 0.2$ and $L/h_2 \geq 0.2$. Electrical junctions between thin films, nanotubes, and nanorods generally have $\eta = \rho_c/\rho_2 h_2 \gg 2$ since the height of the contact members are in nanometer. Hence, it is expected that these nanoscale electrical contacts can be modeled with the "one-dimensional current flow" restriction of standard TLM. Recently, transmission line theory has been used to model and measure various low-dimensional material based contacts, such as, metal-CNT [96], metal-nanofiber, Gold-MoS_2 [56], [97], [98], Indium- MoS_2 [56], Nickel- MoS_2 [98], and graphene-metal ohmic contacts [99].

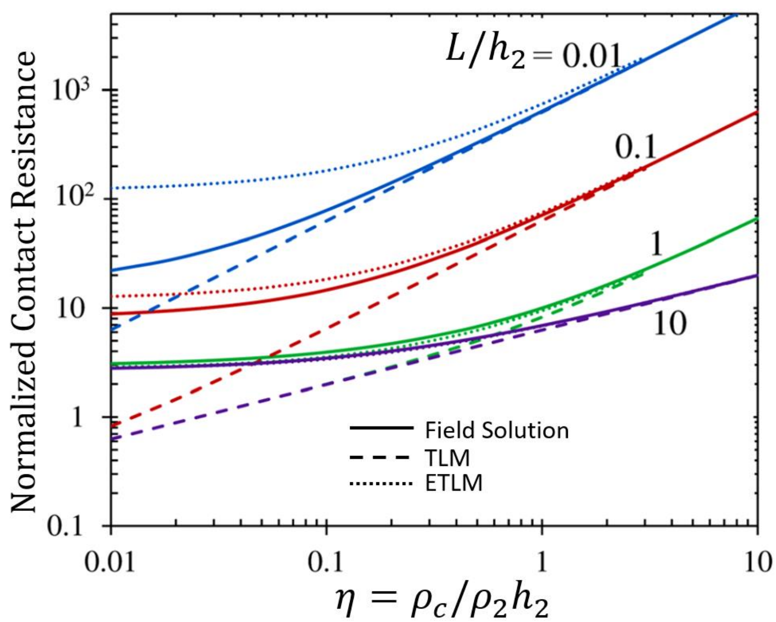

Figure 1.10 Normalized contact resistance as a function of $\eta = \rho_c/\rho_2 h_2$ for various L/h_2 (Fig. 1.8a). [84]

b) *Overcoming ohmic contact limitation, considering non-linear current transport:* The figure of merit used for contacts characterization is the specific contact resistivity ρ_c, defined as the ratio of the voltage drop to current density. It has a constant value for strictly linear contacts. If the junction is highly non-linear, the ohmic approximation fails to give accurate characterization of the contact. The dependence $\rho_c = V_c/J_c(V_c)$ needs to be considered. In 1999, Onomura et al. [100] found ρ_c for Pt to p-GaN contacts changing nearly 3 orders of magnitude for current varying from ≈ 0 to $10\,\mathrm{kA/cm^2}$. Piotrzkowski et al. [101], in 2011, presented analytical generalization of the TLM formulas which include functional dependence of $J_c(\mathrm{V_c})$, where J_c and V_c are the contact current density and contact voltage, respectively. In standard TLM measurement, $\rho_c = wR_c^2/\rho_2$, where w is the width of the TLM test pattern, R_c is the contact resistance, and ρ_2 is the resistivity of the semiconductor. Ref [101]'s method obtains $\rho_c = wR_cR_c^*/\rho_2$, where R_c^* is the differential resistance of the planar contact. In 2014, He et al. [102] proposed a numerical method to characterize non-linear metal-semiconductor contacts. They added a Schottky diode to the standard TLM in series with the original pure resistance to account for the nonlinearity, as shown in Fig. 1.11 (Fig. 1 of Ref. [102]). Interfacial oxidation or sintering processes lead to ρ_c. In their model, voltage $V = V_s + \rho_c J_c(V_s)$, where V_s is the voltage across the Schottky diode.

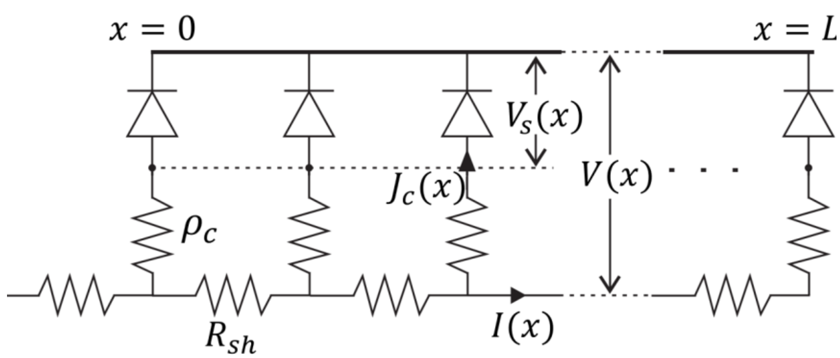

Figure 1.11 Modified transmission line model (TLM) including the non-linear characteristics of the contact. [102]

c) *Overcoming constant specific contact resistivity assumption along the contact length:* The third and the most important limitation of the standard TLM theory is its constant ρ_c assumption along the entire contact length. ρ_c is calculated from the applied voltage and the corresponding current density for the two contacting members, treating the junction as one-dimensional. This treatment is valid only for ohmic contacts with uniform interfacial layer properties. In practical contacts, ρ_c depends on local voltage drop and local contact current density, and therefore, varies spatially. Physically, this spatial dependence of ρ_c may be introduced by a variety of factors, such as, the inherent non-linearity of the current density-voltage ($J - V$) profiles of tunneling and Schottky junctions, rough interfacial layer, nonuniform distribution of oxides, contaminants or impurities in the contact layer etc. The effects of this non-uniform ρ_c along the contact length need to be considered for a more accurate characterization of the electrical properties in a contact structure. This important issue has not been addressed in the existing literature.

Here, we propose a two-dimensional TLM theory by including the effects of spatially varying specific contact resistivity along the contact length [103]–[106]. We use the two dimensional TLM [103], [104] for ohmic contacts, and TLM coupled with the thermionic injection model [105], [107] for Schottky contacts and the quantum self-consistent model [10], [79] for tunneling type contacts. We demonstrate a method to control current distribution, by engineering the interface layer properties and geometry. We find that current crowding can be mitigated by strategically designing the specific contact resistivity ρ_c along the contact length.

1.3 Organization of this thesis

Chapter 2 presents the study of quantum tunneling induced current transport in nano- and subnano-meter metal-insulator-metal (MIM) junctions with dissimilar metal electrodes. A self-consistent model is formulated to calculate the tunneling current density. The results are compared with Simmons' analytical formula. The polarity dependent current density – bias voltage (*J-V*) curves are examined in detail for various parameters in different voltage regimes.

Chapter 3 presents the study of current transport and contact resistance in nanoscale parallel electrical contacts in Cartesian geometry. Traditional lumped circuit transmission line model (TLM) is modified to include the effects of spatially varying specific contact resistivity ρ_c. At first, simple analytical solutions for parallel contacts are derived for the special case of uniform ρ_c. Next, self-consistent numerical solutions are obtained for contacts with linearly varying ρ_c along the contact length. Finally, local voltage-dependent tunneling resistivity along the contact length is examined by solving the TLM equations coupled with the tunneling current self consistently. The current and voltage distribution and the overall contact resistance are analyzed in detail, for various input voltage, electrical contact dimension, and material properties. The results for ohmic contact are verified with finite element method (FEM) based simulations [103].

Chapter 4 extends the method of chapter 3 to circular contacts. Reeves's circular transmission line model [89], [108] (CTLM) is modified to include the effects of radially varying ρ_c. First, ohmic contacts are analyzed and Bessel function based analytical solutions are derived for the special case of uniform ρ_c. Then, tunneling type contacts are analyzed and local voltage-dependent tunneling resistivity along the contact length is examined by solving the TLM equations coupled with the tunneling current self consistently. The current and voltage distributions in such contacts and their overall contact resistance are studied in detail, for various input voltages, contact dimensions, and material properties.

Chapter 5 presents a theoretical study of the contact resistance and the current flow distribution for electrical contacts between two-dimensional (2D) materials and three-dimensional (3D) metals. Self-consistent solutions are obtained by coupling the modified TLM developed in chapter 3 with the improved thermionic current injection model for 2D materials [109]. First, we study the current and voltage distributions in such contacts and their overall contact resistance for various input voltages, temperatures, contact dimensions, and material properties. Then, we propose to reduce contact resistance in 2D-material-based electrical contacts by roughness engineering of the contact interfaces. Results are compared with existing theoretical models and validated with experimental data [105].

Chapter 6 demonstrates a method to mitigate current crowding, by engineering the interface layer properties and geometry [106], [110]. Ohmic, Schottky and tunneling type contacts are studied based on the formulation derived in chapter 2, 3, 4 and 5. First, current steering and redistribution are realized by strategically designing the specific contact resistivity ρ_c along the contact length. Then, a nanometer thin insulating tunneling gap is introduced between highly conductive contact members to reduce the severe current crowding effects while maintaining similar total contact resistance.

The conclusion and suggestions for future work are given in Chapter 7.

REFERENCES

REFERENCES

[1] M. Ieong, B. Doris, J. Kedzierski, K. Rim, and M. Yang, “Silicon device scaling to the sub-10-nm regime,” *Science*, vol. 306, no. 5704, pp. 2057–2060, Dec. 2004, doi: 10.1126/science.1100731.

[2] J. Zheng *et al.*, “Sub-10 nm Gate Length Graphene Transistors: Operating at Terahertz Frequencies with Current Saturation,” *Sci. Rep.*, vol. 3, no. 1, Art. no. 1, Feb. 2013, doi: 10.1038/srep01314.

[3] Tersoff and S. B. Hamann, “Theory of the scanning tunneling microscope.,” *Phys. Rev. B Condens. Matter*, vol. 31, no. 2, pp. 805–813, 1985.

[4] T. L. Cocker *et al.*, “An ultrafast terahertz scanning tunnelling microscope,” *Nat. Photonics*, vol. 7, no. 8, pp. 620–625, Aug. 2013, doi: 10.1038/nphoton.2013.151.

[5] M. S. Ghamsari and S. Dhara, *Nanorods and Nanocomposites*. 2020.

[6] M. A. Mackey, M. R. K. Ali, L. A. Austin, R. D. Near, and M. A. El-Sayed, “The Most Effective Gold Nanorod Size for Plasmonic Photothermal Therapy: Theory and In Vitro Experiments,” *J. Phys. Chem. B*, vol. 118, no. 5, pp. 1319–1326, Feb. 2014, doi: 10.1021/jp409298f.

[7] S. E. Wawra, L. Pflug, T. Thajudeen, C. Kryschi, M. Stingl, and W. Peukert, “Determination of the two-dimensional distributions of gold nanorods by multiwavelength analytical ultracentrifugation,” *Nat. Commun.*, vol. 9, no. 1, Art. no. 1, Nov. 2018, doi: 10.1038/s41467-018-07366-9.

[8] C. Li, E. T. Thostenson, and T.-W. Chou, “Dominant role of tunneling resistance in the electrical conductivity of carbon nanotube–based composites,” *Appl. Phys. Lett.*, vol. 91, no. 22, p. 223114, Nov. 2007, doi: 10.1063/1.2819690.

[9] J. G. Simmons, “Generalized Formula for the Electric Tunnel Effect between Similar Electrodes Separated by a Thin Insulating Film,” *J. Appl. Phys.*, vol. 34, no. 6, pp. 1793–1803, Jun. 1963, doi: 10.1063/1.1702682.

[10] P. Zhang, “Scaling for quantum tunneling current in nano- and subnano-scale plasmonic junctions,” *Sci. Rep.*, vol. 5, p. 9826, May 2015, doi: 10.1038/srep09826.

[11] “Making Chips At 3nm And Beyond,” *Semiconductor Engineering*, Apr. 16, 2020. https://semiengineering.com/making-chips-at-3nm-and-beyond/.

[12] “TSMC Details 3nm Process Technology: Full Node Scaling for 2H22 Volume Production.” https://www.anandtech.com/show/16024/tsmc-details-3nm-process-technology-details-full-node-scaling-for-2h22.

[13] I. Gayduchenko *et al.*, “Tunnel field-effect transistors for sensitive terahertz detection,” *Nat. Commun.*, vol. 12, no. 1, Art. no. 1, Jan. 2021, doi: 10.1038/s41467-020-20721-z.

[14] A. Seabaugh, “The Tunneling Transistor,” *IEEE Spectrum: Technology, Engineering, and Science News*, Sep. 30, 2013. https://spectrum.ieee.org/semiconductors/devices/the-tunneling-transistor.

[15] T. Ihn *et al.*, “Graphene single-electron transistors,” *Mater. Today*, vol. 13, no. 3, pp. 44–50, Mar. 2010, doi: 10.1016/S1369-7021(10)70033-X.

[16] C. Thelander *et al.*, “Single-electron transistors in heterostructure nanowires,” *Appl. Phys. Lett.*, vol. 83, no. 10, pp. 2052–2054, Sep. 2003, doi: 10.1063/1.1606889.

[17] H. W. C. Postma, T. Teepen, Z. Yao, M. Grifoni, and C. Dekker, “Carbon Nanotube Single-Electron Transistors at Room Temperature,” *Science*, vol. 293, no. 5527, pp. 76–79, Jul. 2001, doi: 10.1126/science.1061797.

[18] R. Patel, Y. Agrawal, and R. Parekh, “Single-electron transistor: review in perspective of theory, modelling, design and fabrication,” *Microsyst. Technol.*, Sep. 2020, doi: 10.1007/s00542-020-05002-5.

[19] M. I. of Physics and Technology, “Quantum Tunneling in Graphene Advances the Age of High Speed Terahertz Wireless Communications,” *SciTechDaily*, Feb. 28, 2021. https://scitechdaily.com/quantum-tunneling-in-graphene-advances-the-age-of-high-speed-terahertz-wireless-communications/.

[20] J. M. Hergenrother, J. G. Lu, and M. Tinkham, “The single-electron transistor as an ultrasensitive microwave detector,” *IEEE Trans. Appl. Supercond.*, vol. 5, no. 2, pp. 2604–2607, Jun. 1995, doi: 10.1109/77.403123.

[21] M. A. Sillanpää, L. Roschier, and P. J. Hakonen, “Charge sensitivity of the inductive single-electron transistor,” *Appl. Phys. Lett.*, vol. 87, no. 9, p. 092502, Aug. 2005, doi: 10.1063/1.2034096.

[22] D. Mozyrsky, I. Martin, and M. B. Hastings, “Quantum-limited sensitivity of single-electron-transistor-based displacement detectors,” *Phys. Rev. Lett.*, vol. 92, no. 1, p. 018303, Jan. 2004, doi: 10.1103/PhysRevLett.92.018303.

[23] J. Yoon *et al.*, “Determination of individual contact interfaces in carbon nanotube network-based transistors,” *Sci. Rep.*, vol. 7, no. 1, Art. no. 1, Jul. 2017, doi: 10.1038/s41598-017-05653-x.

[24] B. E. Kilbride *et al.*, “Experimental observation of scaling laws for alternating current and direct current conductivity in polymer-carbon nanotube composite thin films,” *J. Appl. Phys.*, vol. 92, no. 7, pp. 4024–4030, Sep. 2002, doi: 10.1063/1.1506397.

[25] M. Foygel, R. D. Morris, D. Anez, S. French, and V. L. Sobolev, “Theoretical and computational studies of carbon nanotube composites and suspensions: Electrical and

thermal conductivity," *Phys. Rev. B*, vol. 71, no. 10, Mar. 2005, doi: 10.1103/PhysRevB.71.104201.

[26] J. Tang *et al.*, "Flexible CMOS integrated circuits based on carbon nanotubes with sub-10 ns stage delays," *Nat. Electron.*, vol. 1, no. 3, pp. 191–196, Mar. 2018, doi: 10.1038/s41928-018-0038-8.

[27] L.-M. Peng, "A new stage for flexible nanotube devices," *Nat. Electron.*, vol. 1, no. 3, pp. 158–159, Mar. 2018, doi: 10.1038/s41928-018-0045-9.

[28] P. Zhang and Y. Y. Lau, "Ultrafast and nanoscale diodes," *J. Plasma Phys.*, vol. 82, no. 5, Oct. 2016, doi: 10.1017/S002237781600091X.

[29] S. Srisonphan, Y. S. Jung, and H. K. Kim, "Metal–oxide–semiconductor field-effect transistor with a vacuum channel," *Nat. Nanotechnol.*, vol. 7, no. 8, Art. no. 8, Aug. 2012, doi: 10.1038/nnano.2012.107.

[30] B. R. Stoner and J. T. Glass, "Nothing is like a vacuum," *Nat. Nanotechnol.*, vol. 7, no. 8, Art. no. 8, Aug. 2012, doi: 10.1038/nnano.2012.130.

[31] G. Wu, X. Wei, S. Gao, Q. Chen, and L. Peng, "Tunable graphene micro-emitters with fast temporal response and controllable electron emission," *Nat. Commun.*, vol. 7, no. 1, Art. no. 1, May 2016, doi: 10.1038/ncomms11513.

[32] P. 23 J. 2014 | 16:14 GMT, "Introducing the Vacuum Transistor: A Device Made of Nothing - IEEE Spectrum," *IEEE Spectrum: Technology, Engineering, and Science News*. https://spectrum.ieee.org/semiconductors/devices/introducing-the-vacuum-transistor-a-device-made-of-nothing.

[33] G. Aguirregabiria, D. C. Marinica, R. Esteban, A. K. Kazansky, J. Aizpurua, and A. G. Borisov, "Role of electron tunneling in the nonlinear response of plasmonic nanogaps," *Phys. Rev. B*, vol. 97, no. 11, p. 115430, Mar. 2018, doi: 10.1103/PhysRevB.97.115430.

[34] "Hudson Group: Research Background." https://www.personal.psu.edu/ewh10/ResearchBackground.htm.

[35] D. K. Schroder, *Semiconductor Material and Device Characterization*. Wiley-Blackwell, 1998.

[36] H. Murrmann and D. Widmann, "Current crowding on metal contacts to planar devices," *IEEE Trans. Electron Devices*, vol. 16, no. 12, pp. 1022–1024, Dec. 1969, doi: 10.1109/T-ED.1969.16904.

[37] P. Zhang, Y. Y. Lau, and R. M. Gilgenbach, "Analysis of current crowding in thin film contacts from exact field solution," *J. Phys. Appl. Phys.*, vol. 48, no. 47, p. 475501, Oct. 2015, doi: 10.1088/0022-3727/48/47/475501.

[38] P. Zhang and Y. Y. Lau, “Constriction Resistance and Current Crowding in Vertical Thin Film Contact,” *IEEE J. Electron Devices Soc.*, vol. 1, no. 3, pp. 83–90, Mar. 2013, doi: 10.1109/JEDS.2013.2261435.

[39] P. Zhang, Y. Y. Lau, and R. S. Timsit, “On the Spreading Resistance of Thin-Film Contacts,” *IEEE Trans. Electron Devices*, vol. 59, no. 7, pp. 1936–1940, Jul. 2012, doi: 10.1109/TED.2012.2195317.

[40] R. Holm, *Electric Contacts: Theory and Application*, 4th ed. Berlin Heidelberg: Springer-Verlag, 1967.

[41] R. S. Timsit, “Electrical contact resistance: properties of stationary interfaces,” *IEEE Trans. Compon. Packag. Technol.*, vol. 22, no. 1, pp. 85–98, Mar. 1999, doi: 10.1109/6144.759357.

[42] A. M. Rosenfeld and R. S. Timsit, “The potential distribution in a constricted cylinder: an exact solution,” *Q. Appl. Math.*, vol. 39, no. 3, pp. 405–417, 1981.

[43] R. S. Timsit, “Electrical Contacts: Scientific Fundamentals,” in *Encyclopedia of Tribology*, Q. J. Wang and Y.-W. Chung, Eds. Boston, MA: Springer US, 2013, pp. 903–905.

[44] P. Zhang, Q. Gu, Y. Y. Lau, and Y. Fainman, “Constriction Resistance and Current Crowding in Electrically Pumped Semiconductor Nanolasers with the Presence of Undercut and Sidewall Tilt,” *IEEE J. Quantum Electron.*, vol. 52, no. 3, pp. 1–7, Mar. 2016, doi: 10.1109/JQE.2016.2516443.

[45] F. Antoulinakis, D. Chernin, P. Zhang, and Y. Y. Lau, “Effects of temperature dependence of electrical and thermal conductivities on the Joule heating of a one dimensional conductor,” *J. Appl. Phys.*, vol. 120, no. 13, p. 135105, Oct. 2016, doi: 10.1063/1.4964112.

[46] M. Pedram, “Power Minimization in IC Design: Principles and Applications,” *ACM Trans. Des. Autom. Electron. Syst.*, vol. 1, pp. 3–56, 1996.

[47] M. Pedram and S. Nazarian, “Thermal Modeling, Analysis, and Management in VLSI Circuits: Principles and Methods,” *Proc. IEEE*, vol. 94, no. 8, pp. 1487–1501, Aug. 2006, doi: 10.1109/JPROC.2006.879797.

[48] “2000 Review of federal programs for wire system safety National Science and Technology Council Final Report.”

[49] J. S. Kuzniar and G. A. Slenski, “Wire integrity field survey of USAF legacy aircraft ReportADP014075," 2001.

[50] P. Zhang, “Effects of Surface Roughness on Electrical Contact, RF Heating and Field Enhancement,” PhD thesis, University of Michigan, 2012.

[51] K. N. Tu, Y. Liu, and M. Li, “Effect of Joule heating and current crowding on electromigration in mobile technology,” *Appl. Phys. Rev.*, vol. 4, no. 1, p. 011101, Jan. 2017, doi: 10.1063/1.4974168.

[52] M. R. Gomez, J. C. Zier, R. M. Gilgenbach, D. M. French, W. Tang, and Y. Y. Lau, “Effect of soft metal gasket contacts on contact resistance, energy deposition, and plasma expansion profile in a wire array Z pinch,” *Rev. Sci. Instrum.*, vol. 79, no. 9, p. 093512, Sep. 2008, doi: 10.1063/1.2991110.

[53] M. Park *et al.*, “Effects of a carbon nanotube layer on electrical contact resistance between copper substrates,” *Nanotechnology*, vol. 17, no. 9, pp. 2294–2303, Apr. 2006, doi: 10.1088/0957-4484/17/9/038.

[54] F. Antoulinakis and Y. Y. Lau, “A theory of contact resistance under AC conditions,” *J. Appl. Phys.*, vol. 127, no. 12, p. 125107, Mar. 2020, doi: 10.1063/1.5142511.

[55] Q. Wang, X. Tao, L. Yang, and Y. Gu, “Current crowding in two-dimensional black-phosphorus field-effect transistors,” *Appl. Phys. Lett.*, vol. 108, no. 10, p. 103109, Mar. 2016, doi: 10.1063/1.4943655.

[56] Y. Wang *et al.*, “Van der Waals contacts between three-dimensional metals and two-dimensional semiconductors,” *Nature*, vol. 568, no. 7750, pp. 70–74, Apr. 2019, doi: 10.1038/s41586-019-1052-3.

[57] K. L. Grosse, M.-H. Bae, F. Lian, E. Pop, and W. P. King, “Nanoscale Joule heating, Peltier cooling and current crowding at graphene–metal contacts,” *Nat. Nanotechnol.*, vol. 6, no. 5, Art. no. 5, May 2011, doi: 10.1038/nnano.2011.39.

[58] P. Karnatak, T. P. Sai, S. Goswami, S. Ghatak, S. Kaushal, and A. Ghosh, “Current crowding mediated large contact noise in graphene field-effect transistors,” *Nat. Commun.*, vol. 7, no. 1, Art. no. 1, Dec. 2016, doi: 10.1038/ncomms13703.

[59] J. S. Huang, E. C. C. Yeh, Z. B. Zhang, and K. N. Tu, “The effect of contact resistance on current crowding and electromigration in ULSI multi-level interconnects,” *Mater. Chem. Phys.*, vol. 77, no. 2, pp. 377–383, Jan. 2003, doi: 10.1016/S0254-0584(02)00018-4.

[60] Y. Park, J. Joh, J. Chung, and S. Krishnan, “Current Crowding Impact on Electromigration in Al Interconnects,” in *2019 IEEE International Reliability Physics Symposium (IRPS)*, Mar. 2019, pp. 1–6, doi: 10.1109/IRPS.2019.8720448.

[61] S. W. Liang, Y. W. Chang, and C. Chen, “Relieving Hot-Spot Temperature and Current Crowding Effects During Electromigration in Solder Bumps by Using Cu Columns,” *J. Electron. Mater.*, vol. 36, no. 10, pp. 1348–1354, Oct. 2007, doi: 10.1007/s11664-007-0232-3.

[62] E. C. C. Yeh, W. J. Choi, K. N. Tu, P. Elenius, and H. Balkan, “Current-crowding-induced electromigration failure in flip chip solder joints,” *Appl. Phys. Lett.*, vol. 80, no. 4, pp. 580–582, Jan. 2002, doi: 10.1063/1.1432443.

[63] K. N. Tu, “Recent advances on electromigration in very-large-scale-integration of interconnects,” *J. Appl. Phys.*, vol. 94, no. 9, pp. 5451–5473, Oct. 2003, doi: 10.1063/1.1611263.

[64] M. D. Haworth *et al.*, “Significant pulse-lengthening in a multigigawatt magnetically insulated transmission line oscillator,” *IEEE Trans. Plasma Sci.*, vol. 26, no. 3, pp. 312–319, Jun. 1998, doi: 10.1109/27.700759.

[65] E. Schrödinger, “An Undulatory Theory of the Mechanics of Atoms and Molecules,” *Phys. Rev.*, vol. 28, no. 6, pp. 1049–1070, Dec. 1926, doi: 10.1103/PhysRev.28.1049.

[66] H. A. Kramers, “Wellenmechanik und halbzahlige Quantisierung,” *Z. Für Phys.*, vol. 39, no. 10, pp. 828–840, Oct. 1926, doi: 10.1007/BF01451751.

[67] G. Wentzel, “Eine Verallgemeinerung der Quantenbedingungen für die Zwecke der Wellenmechanik,” *Z. Für Phys.*, vol. 38, no. 6, pp. 518–529, Jun. 1926, doi: 10.1007/BF01397171.

[68] Sommerfield A., Bethe H., *Handbuch der Physik*. 1933.

[69] Holm R. and Kirschstein B., *Z Tech Phys.*, no. 16, 488, 1935.

[70] J. G. Simmons, “Electric Tunnel Effect between Dissimilar Electrodes Separated by a Thin Insulating Film,” *J. Appl. Phys.*, vol. 34, no. 9, pp. 2581–2590, Sep. 1963, doi: 10.1063/1.1729774.

[71] V. D. Das and M. S. Jagadeesh, “Tunneling in Al□Al2O3□Al MIM structures,” *Phys. Status Solidi A*, vol. 66, no. 1, pp. 327–333, 1981, doi: 10.1002/pssa.2210660140.

[72] Y. Y. Lau, D. Chernin, D. G. Colombant, and P.-T. Ho, “Quantum extension of Child-Langmuir law,” *Phys. Rev. Lett.*, vol. 66, pp. 1446–1449, Mar. 1991, doi: 10.1103/PhysRevLett.66.1446.

[73] L. K. Ang, T. J. T. Kwan, and Y. Y. Lau, “New Scaling of Child-Langmuir Law in the Quantum Regime,” *Phys. Rev. Lett.*, vol. 91, no. 20, p. 208303, Nov. 2003, doi: 10.1103/PhysRevLett.91.208303.

[74] L. K. Ang and P. Zhang, “Ultrashort-Pulse Child-Langmuir Law in the Quantum and Relativistic Regimes,” *Phys. Rev. Lett.*, vol. 98, no. 16, p. 164802, Apr. 2007, doi: 10.1103/PhysRevLett.98.164802.

[75] S. Bhattacharjee and T. Chowdhury, “Experimental investigation of transition from Fowler–Nordheim field emission to space-charge-limited flows in a nanogap,” *Appl. Phys. Lett.*, vol. 95, no. 6, p. 061501, Aug. 2009, doi: 10.1063/1.3194297.

[76] S. Bhattacharjee, A. Vartak, and V. Mukherjee, “Experimental study of space-charge-limited flows in a nanogap,” *Appl. Phys. Lett.*, vol. 92, no. 19, p. 191503, May 2008, doi: 10.1063/1.2928232.

[77] L. K. Ang, Y. Y. Lau, and T. J. T. Kwan, “Simple derivation of quantum scaling in Child-Langmuir law,” *IEEE Trans. Plasma Sci.*, vol. 32, no. 2, pp. 410–412, Apr. 2004, doi: 10.1109/TPS.2004.826366.

[78] R. H. Fowler and L. Nordheim, “Electron Emission in Intense Electric Fields,” *Proc. R. Soc. Lond. Ser. Contain. Pap. Math. Phys. Character*, vol. 119, no. 781, pp. 173–181, 1928.

[79] S. Banerjee and P. Zhang, “A generalized self-consistent model for quantum tunneling current in dissimilar metal-insulator-metal junction,” *AIP Adv.*, vol. 9, no. 8, p. 085302, Aug. 2019, doi: 10.1063/1.5116204.

[80] P. M. Hall, “Resistance calculations for thin film patterns,” *Thin Solid Films*, vol. 1, no. 4, pp. 277–295, Jan. 1968, doi: 10.1016/0040-6090(68)90046-1.

[81] P. M. Hall, “Resistance calculations for thin film rectangles,” *Thin Solid Films*, vol. 300, no. 1, pp. 256–264, May 1997, doi: 10.1016/S0040-6090(96)09495-3.

[82] M. W. Denhoff, “An accurate calculation of spreading resistance,” *J. Phys. Appl. Phys.*, vol. 39, no. 9, pp. 1761–1765, Apr. 2006, doi: 10.1088/0022-3727/39/9/009.

[83] P. Zhang, Y. Y. Lau, and R. M. Gilgenbach, “Minimization of thin film contact resistance,” *Appl. Phys. Lett.*, vol. 97, no. 20, p. 204103, Nov. 2010, doi: 10.1063/1.3517497.

[84] P. Zhang and Y. Y. Lau, “An exact field solution of contact resistance and comparison with the transmission line model,” *Appl. Phys. Lett.*, vol. 104, no. 20, p. 204102, May 2014, doi: 10.1063/1.4878841.

[85] P. Zhang, D. M. H. Hung, and Y. Y. Lau, “Current flow in a 3-terminal thin film contact with dissimilar materials and general geometric aspect ratios,” *J. Phys. Appl. Phys.*, vol. 46, no. 6, p. 065502, Feb. 2013, doi: 10.1088/0022-3727/46/6/065502.

[86] D. P. Kennedy and P. C. Murley, “A Two-Dimensional Mathematical Analysis of the Diffused Semiconductor Resistor,” *IBM J. Res. Dev.*, vol. 12, no. 3, pp. 242–250, May 1968, doi: 10.1147/rd.123.0242.

[87] H. H. Berger, “Contact Resistance and Contact Resistivity,” *J. Electrochem. Soc.*, vol. 119, no. 4, pp. 507–514, Apr. 1972, doi: 10.1149/1.2404240.

[88] D. K. Schroder and D. L. Meier, “Solar cell contact resistance—A review,” *IEEE Trans. Electron Devices*, vol. 31, no. 5, pp. 637–647, May 1984, doi: 10.1109/T-ED.1984.21583.

[89] G. K. Reeves, “Specific contact resistance using a circular transmission line model,” *Solid-State Electron.*, vol. 23, no. 5, pp. 487–490, May 1980, doi: 10.1016/0038-1101(80)90086-6.

[90] G. K. Reeves and B. Harrison, “An analytical model for alloyed ohmic contacts using a trilayer transmission line model,” *IEEE Trans. Electron Devices*, vol. 42, no. 8, pp. 1536–1547, Aug. 1995, doi: 10.1109/16.398670.

[91] G. K. Reeves, P. W. Leech, and H. B. Harrison, “Understanding the sheet resistance parameter of alloyed ohmic contacts using a transmission line model,” *Solid-State Electron.*, vol. 38, no. 4, pp. 745–751, Apr. 1995, doi: 10.1016/0038-1101(94)00234-7.

[92] G. K. Reeves and H. B. Harrison, “Using TLM principles to determine MOSFET contact and parasitic resistance,” *Solid-State Electron.*, vol. 41, no. 8, pp. 1067–1074, Aug. 1997, doi: 10.1016/S0038-1101(97)00062-2.

[93] J. Overmeyer, “Calculation of the Current Density in the Contacts of a Thin Film Resistor,” *IBM J. Res. Dev.*, vol. 14, no. 1, pp. 66–69, Jan. 1970, doi: 10.1147/rd.141.0066.

[94] E. G. Woelk, H. Krautle, and H. Beneking, “Measurement of low resistive ohmic contacts on semiconductors,” *IEEE Trans. Electron Devices*, vol. 33, no. 1, pp. 19–22, Jan. 1986, doi: 10.1109/T-ED.1986.22430.

[95] J. M. Pimbley, “Dual-level transmission line model for current flow in metal-semiconductor contacts,” *IEEE Trans. Electron Devices*, vol. 33, no. 11, pp. 1795–1800, Nov. 1986, doi: 10.1109/T-ED.1986.22742.

[96] C. Lan, P. Srisungsitthisunti, P. B. Amama, T. S. Fisher, X. Xu, and R. G. Reifenberger, “Measurement of metal/carbon nanotube contact resistance by adjusting contact length using laser ablation,” *Nanotechnology*, vol. 19, no. 12, p. 125703, Mar. 2008, doi: 10.1088/0957-4484/19/12/125703.

[97] C. D. English, G. Shine, V. E. Dorgan, K. C. Saraswat, and E. Pop, “Improved Contacts to MoS2 Transistors by Ultra-High Vacuum Metal Deposition,” *Nano Lett.*, vol. 16, no. 6, pp. 3824–3830, Jun. 2016, doi: 10.1021/acs.nanolett.6b01309.

[98] D. Somvanshi *et al.*, “Nature of carrier injection in metal/2D-semiconductor interface and its implications for the limits of contact resistance,” *Phys. Rev. B*, vol. 96, no. 20, p. 205423, Nov. 2017, doi: 10.1103/PhysRevB.96.205423.

[99] J. S. Moon *et al.*, “Ultra-low resistance ohmic contacts in graphene field effect transistors,” *Appl. Phys. Lett.*, vol. 100, no. 20, p. 203512, May 2012, doi: 10.1063/1.4719579.

[100] M. Onomura *et al.*, “The analysis of contact resistivity between a p-type GaN layer and electrode in InGaN MQW laser diodes,” *Mater. Sci. Eng. B*, vol. 59, no. 1, pp. 366–369, May 1999, doi: 10.1016/S0921-5107(98)00353-5.

[101] R. Piotrzkowski, E. Litwin-Staszewska, and Sz. Grzanka, “Towards proper characterization of nonlinear metal-semiconductor contacts. Generalization of the transmission line method,” *Appl. Phys. Lett.*, vol. 99, no. 5, p. 052101, Aug. 2011, doi: 10.1063/1.3619813.

[102] K. He *et al.*, “Numerical approach to generalized transmission line model and its application to Au/Sn/p-HgCdTe contact,” *J. Appl. Phys.*, vol. 115, no. 16, p. 164506, Apr. 2014, doi: 10.1063/1.4873303.

[103] S. Banerjee, J. Luginsland, and P. Zhang, “A Two Dimensional Tunneling Resistance Transmission Line Model for Nanoscale Parallel Electrical Contacts,” *Sci. Rep.*, vol. 9, no. 14484, pp. 1–14, Oct. 2019, doi: 10.1038/s41598-019-50934-2.

[104] S. Banerjee, P. Y. Wong, and P. Zhang, “Contact resistance and current crowding in tunneling type circular nano-contacts,” *J. Phys. Appl. Phys.*, vol. 53, no. 35, p. 355301, Jun. 2020, doi: 10.1088/1361-6463/ab8fe0.

[105] S. Banerjee, L. Cao, Y. S. Ang, L. K. Ang, and P. Zhang, “Reducing Contact Resistance in Two-Dimensional-Material-Based Electrical Contacts by Roughness Engineering,” *Phys. Rev. Appl.*, vol. 13, no. 6, p. 064021, Jun. 2020, doi: 10.1103/PhysRevApplied.13.064021.

[106] P. Zhang, S. Banerjee, and J. Luginsland, “Tunneling Electrical Contacts,” Patent US 10,755,975 B2, Aug. 25, 2020.

[107] Y. S. Ang, H. Y. Yang, and L. K. Ang, “Universal Scaling Laws in Schottky Heterostructures Based on Two-Dimensional Materials,” *Phys. Rev. Lett.*, vol. 121, no. 5, p. 056802, Aug. 2018, doi: 10.1103/PhysRevLett.121.056802.

[108] C. Xu, J. Wang, M. Wang, H. Jin, Y. Hao, and C. P. Wen, “Reeves’s circular transmission line model and its scope of application to extract specific contact resistance,” *Solid-State Electron.*, vol. 50, no. 5, pp. 843–847, May 2006, doi: 10.1016/j.sse.2006.03.007.

[109] Y. S. Ang, H. Y. Yang, and L. K. Ang, “Universal Scaling Laws in Schottky Heterostructures Based on Two-Dimensional Materials,” *Phys. Rev. Lett.*, vol. 121, no. 5, p. 056802, Aug. 2018, doi: 10.1103/PhysRevLett.121.056802.

[110] S. Banerjee, J. Luginsland, and P. Zhang, “Interface Engineering of Electrical Contacts,” *Manuscript Under Preparation*, 2021.

CHAPTER 2

QUANTUM TUNNELING IN METAL-INSULATOR-METAL NANOJUNCTIONS

This chapter is based on the published journal paper "A generalized self-consistent model for quantum tunneling current in dissimilar metal-insulator-metal junction," *AIP Adv.*, vol. 9, no. 8, p. 085302, Aug. 2019, doi: 10.1063/1.5116204, by **S. Banerjee** and P. Zhang [1]. It is presented here with the permission of the copyright holder.

2.1 Introduction

Quantum tunneling [2], [3] is important to nanoelectronic circuit designs, tunneling electrical contacts [4], scanning tunneling microscopes (STMs) [5], [6], plasmonic resonators[7]–[9], carbon nanotubes[10]–[14], graphene [15], [16] and other two-dimensional (2D) materials based devices [17], [18] and novel vacuum nano-devices [19]–[23]. Quantum tunneling effects impose serious challenges to the physical scaling down of traditional electronic circuits [24]. However, it enables the development of future tunneling field-effect transistors (TFETs), which are envisioned to further extend Moore's law[25]. Tunneling in electrical contacts can be utilized to mitigate current crowding and nonuniform heat deposition in the contact region[4], [26]. Tunneling phenomenon may also introduce new regimes in quantum plasmonics [27]. Hence, it is critical to accurately characterize the current density-voltage $(J-V)$ behaviors in nano-scale metal-insulator-metal (MIM) junctions, for a variety of material properties and junction dimensions.

Tunneling effects between electrodes separated by thin insulating films have been studied extensively by Simmons[3], [28]–[31] in 1960s. Although in Simmons' theory the effects of image charge potential are considered, the electron space charge potential and the electron exchange-correlation potential inside the insulator thin films, are ignored. Simmons' model is reliable only in low voltage regime for limited parameter space (insulator gap > 1 nm , barrier height > 3 eV)[27]. The effects of space charge in a vacuum nanogap have been studied [32]–[34] extensively, with extensions to short pulse [35]. Recently, Zhang [27] proposed a self-consistent model (SCM) to characterize quantum tunneling current in similar MIM junctions, considering current flowing from both the electrodes. It is found that the $J - V$ characteristics may be divided into three regimes: direct tunneling, field emission, and space-charge-limited regime [27].

However, the SCM for similar MIM junctions is not sufficient to characterize electron tunneling through MIM junctions formed between two electrodes with different work functions, where the $J - V$ characteristic is dependent upon the polarity of the bias voltage [28]. The asymmetry of the polarity-dependent $J - V$ behavior is important to harmonic mixers, rectifiers, millimeter wave and infrared detectors [36]. Several efforts have been made to enhance this asymmetry in dissimilar MIM tunnel diodes [36]–[38]. Moreover, dissimilar MIM junctions are naturally formed between scanning tunneling microscope's tip and substrate [5], [6] and in nanoscale electrical contacts [4], [39], [40].

In this Chapter, we extend the theory of Zhang [27] to dissimilar MIM junctions (Figure 2.1). Following Simmons [28], we define the forward bias (FB) and reverse bias (RB) of the MIM junction, when the metal electrode with higher work function is negatively and positively biased, respectively. We provide a detailed study of FB and RB asymmetry and its dependence on a wide range of input parameters (work functions of the electrodes, thickness and relative permittivity of the insulator), for different voltage regimes. The FB and RB characteristics are found to cross over at high voltages in the field emission regime. The asymmetry between the current density profiles increases with the work function difference of the electrodes, the thickness or permittivity of the insulator layer.

2.2 The Self-Consistent Model

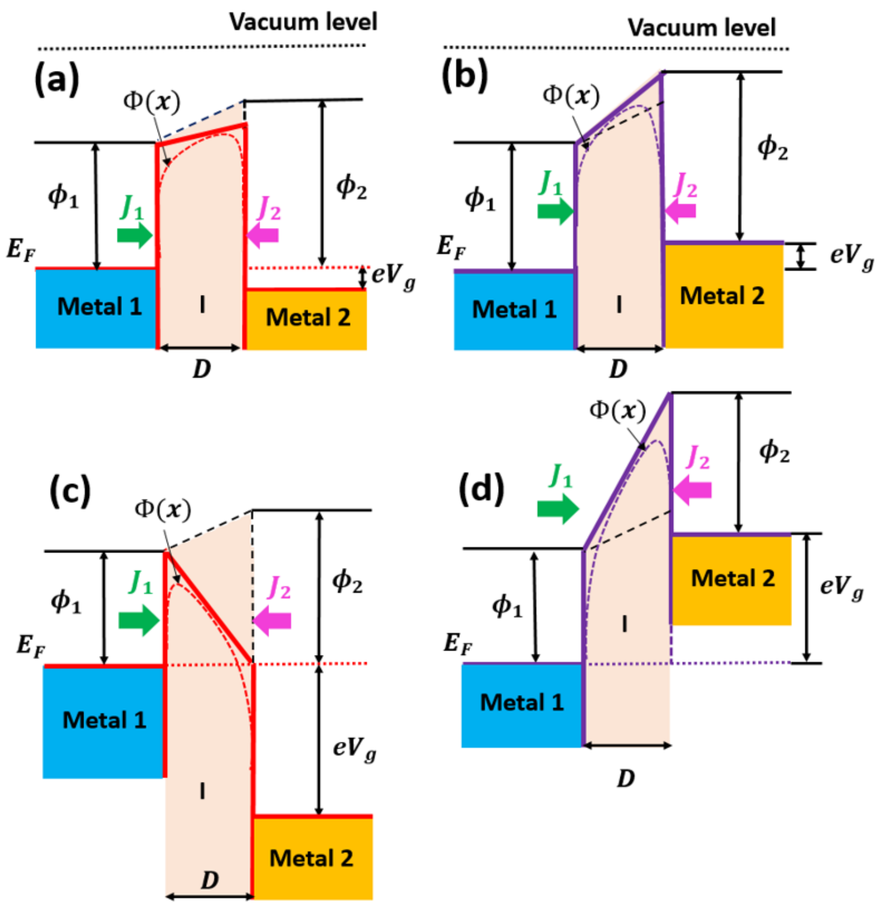

Figure 2.1 Dissimilar metal-insulator-metal (MIM) tunneling junction. The metal electrodes have equilibrium Fermi level E_F and work function W_1 and W_2 (in these schematics we assume $W_2 > W_1$). $\phi_1 = W_1 - X, \phi_2 = W_2 - X$, where X is electron affinity of the insulator. The insulator thin film thickness is D. The applied voltage bias is V_g. The current densities emitted from the electrode 1 and 2 into the gap are J_1 and J_2, respectively. (a), (c) reverse bias (W_2 is positively biased) condition; (b),(d) forward bias (W_2 is negatively biased) condition. (a), (b) represent low and (c), (d) represent high bias voltage conditions. [1]

Our self-consistent model (SCM) formulation is based on the formulation of similar MIM junctions[27]. The potential barrier formed between the two electrodes is,

$$\Phi(x) = E_F + \Phi_w(x) + \Phi_{image}(x) + eV(x) + \Phi_{xc}(x), \tag{2.1}$$

where E_F is the equilibrium Fermi level; $\Phi_w(x) = \phi_1 + (\phi_2 - \phi_1)x/D$; $\phi_1 = W_1 - X, \phi_2 = W_2 - X$; W_1 and W_2 are the work functions of metal electrode 1 and 2 respectively; X is electron affinity of the insulator; $\Phi_{image}(x) = (-e^2/8\pi\epsilon_r\epsilon_0)[1/2x + \sum_{n=1}^{\infty}(nD/(n^2D^2 - x^2) - 1/nD)]$ is the image charge potential energy including the effect of anode screening[34], where e is the electron charge, ϵ_0 is the permittivity of free space, ϵ_r is the relative permittivity of the insulator, and D is the gap distance; the electric potential $eV(x) = eV_g x/D + eV_{sc}(x)$, where the two terms are the potential due to the external applied voltage V_g and the potential due to the electron space charge, respectively; and $\Phi_{xc}(x) = (\epsilon_{xc} - (r_s/3)\, d\epsilon_{xc}/dr_s) \times E_H$ is the electron exchange-correlation potential calculated by the Kohn-Sham local density approximation (LDA)[41], where $r_s(x)$ is the local Seitz radius $[4\pi n(x)(r_s a_0)^3/3 = 1]$ in terms of the Bohr radius $a_0 = 0.0529$ nm, $n(x)$ is the electron density, $E_H = 27.2$ eV is the Hartree energy, and $\epsilon_{xc} = \epsilon_x + \epsilon_c$ is the exchange-correlation energy [41]–[43]. $\epsilon_x = -(3/4)(3/2\pi)^{2/3}(1/r_s)$, and $\epsilon_c = -2A(1 + a_1 r_s)\ln[1 + 1/2\kappa A]$ are the exchange energy and the correlation energy respectively, for a uniform electron gas of density n, where $\kappa = b_1 {r_s}^{1/2} + b_2 r_s + b_3 {r_s}^{3/2} + b_4 {r_s}^{c+1}$, and A, c, a_1, b_1, b_2, b_3, and b_4 are constants obtained from[41].

The probability $D(E_x)$ that an electron with longitudinal energy E_x (normal to the surface) can penetrate the potential barrier $\Phi(x)$ is given by the WKBJ approximation [44],

$$D(E_x) = \exp[-\frac{2}{\hbar}\int_{x_1}^{x_2}\sqrt{2m_e[\Phi(x) - E_x]}\, dx], \tag{2.2}$$

where x_1 and x_2 are the two roots of $E_x - \Phi(x) = 0$, m_e is the electron rest mass. The tunneling current density from electrode 1 to the right, and from electrode 2 to the left, are respectively [3], [27], [34],

$$J_1 = e\int_{-\infty}^{\infty} N_1(E_x)D(E_x)dE_x, \tag{2.3a}$$

$$J_2 = e\int_{-\infty}^{\infty} N_2(E_x)D(E_x)dE_x, \tag{2.3b}$$

$$N_1(E_x) = \frac{m_e k_B T}{2\pi^2\hbar^3}\ln\left(1 + e^{-(E_x - E_F)/k_B T}\right), \tag{2.3c}$$

$$N_2(E_x) = \frac{m_e k_B T}{2\pi^2\hbar^3}\ln\left(1 + e^{-\left(E_x + eV_g - E_F\right)/k_B T}\right), \tag{2.3d}$$

where $D(E_x)$ is given in Eq. (2.2), $N_{1,2}(E_x)dE_x$ is the total number of electrons inside electrode 1 (electrode 2) with longitudinal energy between E_x and $E_x + dE_x$ impinging on the surface of electrode 1 (2) across a unit area per unit time, calculated by the free-electron theory of metal [45], m_e is the electron rest mass, $\hbar$ is the reduced Planch constant, k_B is the Boltzmann constant, and T is the electrode temperature.

Inside the insulator, $0 < x < D$, we solve the coupled Schrödinger equation and the Poisson equation, for the electric potential $eV(x)$ and the exchange-correlation potential $\Phi_{xc}(x)$,

$$-\frac{\hbar^2}{2m_e}\frac{d^2\psi}{dx^2} - [eV(x) - \Phi_{xc}(x)]\psi = E_0\psi, \tag{2.4}$$

$$\frac{d^2V(x)}{dx^2} = \frac{e\psi\psi^*}{\varepsilon_r\varepsilon_0}, \tag{2.5}$$

where ψ is the complex electron wave function, $n = \psi\psi^*$ is the electron density, and E_0 is the electron emission energy (with respect to the Fermi energy E_F). We assume $E_0 = 0$ in the calculation.

For a bias voltage V_g, the boundary conditions are, $V(0) = 0$, and $V(D) = V_g$. We also have the boundary conditions that both ψ and $d\psi/dx$ are continuous at $x = 0$, and $x = D$. Due to charge conservation, the net current density $J_{net} = J_1 - J_2 = e(i\hbar/2m_e)(\psi\psi^{*\prime} - \psi^*\psi')$ is constant for all *x*, where a prime denotes a derivative with respect to *x*, and $i = \sqrt{-1}$.

For convenience we use nondimensional quantities[27], $\bar{x} = x/D$, $\phi = V(x)/V_g$, $\phi_{xc} = \Phi_{xc}/E_H$, $\phi_g = eV_g/E_H$, $\gamma = J/J_{CL}$, $\overline{E_0} = E_0/eV_g$, $\bar{n} = n/n_0 = \psi\psi^*/n_0$, $\lambda = D/\lambda_0$ where $\lambda_0 = \sqrt{\hbar^2/2em_eV_g}$, $J_{CL} = (4/9)\epsilon_0\sqrt{2e/m_e}\, V_g^{3/2}/D^2$ is the Child-Langmuir law[46], [47], $n_0 = (2\epsilon_0/3e)V_g/D^2$, and E_H is the Hartree energy. The wave function in the normalized form is $\psi(\bar{x}) = \sqrt{n_0}q(\bar{x})e^{i\theta(\bar{x})}$, where $q(\bar{x})$ and $\theta(\bar{x})$ are the nondimensional amplitude and phase respectively, both assumed real. Equations 2.4 and 2.5 are normalized to read,

$$\frac{d^2q}{d\,\bar{x}^2} + \lambda^2\left[\phi - \frac{\phi_{xc}}{\phi_g} - \frac{4}{9}\frac{\gamma_{net}^2}{q^4} + \overline{E_0}\right]q = 0, \tag{2.6}$$

$$\frac{d^2\phi}{d\bar{x}^2} = \frac{2}{3}\frac{q^2}{\varepsilon_r}, \tag{2.7}$$

where $\gamma_{net} = \gamma_1 - \gamma_2$ is the net normalized current density. The boundary conditions to eqs. (2.6) and (2.7) are, $\phi(0) = 0$, $\phi(1) = 1$, $q(1) = \left\{\left(\frac{2}{3\sqrt{1+\overline{E_0}}}\right)\left[\gamma_1 + \gamma_2 + 2\sqrt{\gamma_1\gamma_2}\cos\left(2\lambda\sqrt{1+\overline{E_0}}\right)\right]\right\}^{1/2}$, and $q'(1) = \left(\frac{4}{3}\right)\left(\frac{\lambda\sqrt{\gamma_1\gamma_2}}{q(1)}\right)\sin\left(2\lambda\sqrt{1+\overline{E_0}}\right)$. The normalized emission current density γ_1 and γ_2 are,

$$\gamma_1 = \frac{9}{4\pi}\frac{\lambda^2}{\sqrt{2\phi_g}}\,\bar{T}\int_{-\infty}^{\infty}\ln\left(1 + e^{-\frac{\overline{E_x}-\overline{E_F}}{\bar{T}}}\right)D(\overline{E_x})d\overline{E_x}, \tag{2.8a}$$

$$\gamma_2 = \frac{9}{4\pi}\frac{\lambda^2}{\sqrt{2\phi_g}}\,\bar{T}\int_{-\infty}^{\infty}\ln\left(1 + e^{-\frac{\overline{E_x}+1-\overline{E_F}}{\bar{T}}}\right)D(\overline{E_x})d\overline{E_x}, \tag{2.8b}$$

where $\overline{T} = k_B T/eV_g$, $\overline{E_x} = E_x/eV_g$, and $\overline{E_F} = E_F/eV_g$. By solving Eqs. (2.6) - (2.8) iteratively with the boundary conditions, we can self-consistently obtain the complete potential barrier profile $\Phi(x)$, the current density emitted from both electrodes J_1 and J_2, for any metal electrodes (W_1, W_2), insulator layer (ε_r, X, D), and bias voltage (V_g). It is found the tunneling current emission is insensitive to the temperature and the Fermi level[27]. In our calculations, we assume room temperature $T = 300$ K and $E_F = 5.53$ eV.

It is worthwhile to note that, although the proposed model is developed for DC condition, it is applicable to the excitation of up to the Near Infrared frequency, since in typical metallic tunnel junctions, the tunneling events occur on a timescale much shorter than the period of the driving fields[27], [48], [49].

In this formulation, we have assumed, 1) the electron transmission probability during the emission process can be approximated by the WKBJ solution, where the metal electrodes are based on the free electron gas model; 2) the surfaces of the electrodes are flat and the problem is one-dimensional; 3) the image potential can be approximated by the classical image charge methods; and 4) the two metallic electrodes are separated by a sufficiently thin insulating film (in the nano- or subnano- meter scale), so that charge trapping in the insulator are ignored[30], [50].

2.3 Results and Discussion

Figure 2.2a shows the normalized current density γ as a function of applied gap voltage V_g, for two electrodes having work functions, $W_1 = 4.1$ eV and $W_2 = 5.1$ eV (Au), separated by 1 nm vacuum gap (ϵ_r = 1, $X = 0$ eV). Metal 2 is given a positive bias (i.e. reverse bias, equivalent to Figs. 2.1a and 2.1c). The current densities are calculated from the SCM with both space charge potential and exchange correlation potential V_{xc} included. The $J-V$ curves may be roughly divided into three regimes: direct tunneling regime ($V_g < 1$V), field emission regime (1V $< V_g <$ 10V), and space-charge-limited regime ($V_g > 10$V), similar to the MIM with electrodes of the same material [27].

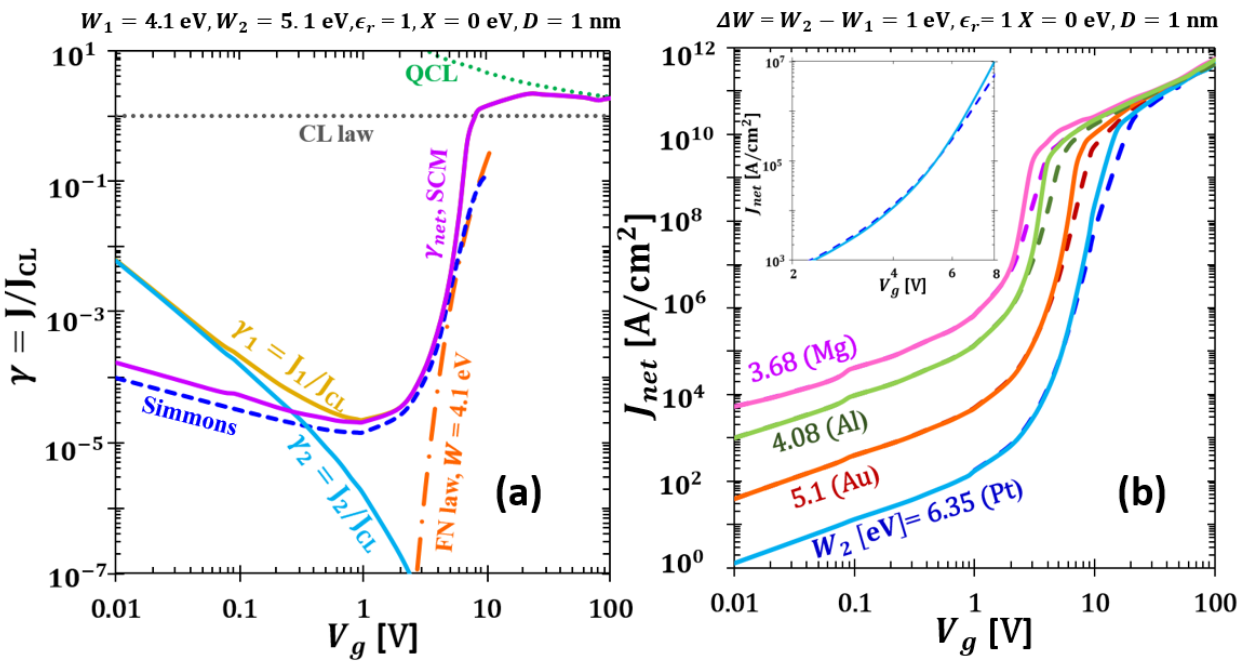

Figure 2.2(a) Normalized (in terms of CL law) current density γ as a function of applied gap voltage V_g, for two electrodes having work functions, $W_1 = 4.1$ eV and $W_2 = 5.1$ eV (Au), separated by 1 nm vacuum gap (ϵ_r = 1, $X = 0$ eV). Metal 2 is positively biased. The calculations are from SCM with both space charge and V_{xc} included. Simmons' formula (dashed line) is from Ref [28], Fowler-Nordheim (FN) law (dash-dotted line) is from Ref. [51]–[53], calculated with the cathode work function W = 4.1 eV, and the quantum CL law (green dotted line) is from Ref. [32], [33]. (b) Current density J_{net} in A/cm^2 as a function of applied gap voltage V_g, for D = 1 nm and vacuum gap (ϵ_r=1, $X = 0$ eV). Solid and dashed lines in (b) represent RB and FB conditions respectively. Top to bottom, W_2 = 3.68 eV (Mg), 4.08 eV (Al), 5.1 eV (Au), 6.35 eV (Pt). The work function difference between the two metals is kept fixed, ΔW= $W_2 - W_1$ = 1 eV. The inset in (b) represents the zoomed in view of the cross over behavior for the case of $W_2 = 6.35$ eV. [1]

In the direct tunneling regime, just like similar MIM junctions[27], the tunneling current density from cathode γ_1 and that from anode γ_2 are comparable. The net current density γ_{net} can be orders of magnitude lower than both γ_1 and γ_2. Therefore, in this regime, both anode emission and cathode emission need to be considered for an accurate estimation of the tunneling current in the dissimilar MIM junction. In the direct tunneling regime, γ_{net} increases linearly with V_g, which implies that the dissimilar electrode MIM junction behaves like an ohmic resister. The $J-V$ characteristic matches well with the Simmons' formula in the direct tunneling regime[28]. In the field emission regime, γ_2 is much smaller compared to γ_1, because the effective barrier height at the cathode is reduced by the bias voltage. The net current density γ_{net} is approaching the Fowler-Nordheim (FN) law [51]–[53] as V_g increases. However, in the field emission regime, Simmons' formula gives a more accurate fit to the self-consistent SCM result, which is due to the inclusion of anode screening in Simmons' formula. Simmons' formula breaks down around $V_g = 4$V. When the gap voltage reaches $V_g = 4$V, the effective barrier height is depressed by V_g below the Fermi level of the cathode (i.e. equivalent to Fig. 2.1c). In the space-charge-limited (SCL) regime, when V_g reaches 100V, the cathode current and therefore the net current approaches the quantum CL law (QCL) [32], [33], which gives the maximum current density that can be transported across a vacuum nano-gap for a given V_g and D, with quantum corrections.

Figure 2.2b shows the net current density J_{net} in $\mathrm{A/cm^2}$ as a function of applied gap voltage V_g, in dissimilar MIM junctions separated by a 1 nm wide vacuum gap for a fixed $\Delta W = W_2 - W_1$ = 1 eV. Solid and dashed lines are for reverse biased (RB) (i.e. higher work function metal is positively biased) and forward biased (FB) (i.e. higher work function metal is negatively biased) current densities, respectively. The tunneling current density of a dissimilar MIM junction is very sensitive to its apparent barrier height. Figure 2.2b shows that, at low voltages ($eV_g < \Delta W$), the characteristics are almost identical for the FB and RB conditions. In the region of $\Delta W < eV_g <$

$W_1 - X$, the FB current exceeds slightly. At a higher voltage, the FB and RB characteristics cross over. The inset of Fig. 2.2b shows the zoomed in view of this cross over behavior for the case of $W_2 = 6.35$ eV. It is shown in Fig. 2.2b, as W_2 (and therefore W_1) increases, the FB and RB characteristics intersect at increased values of V_g, which agrees with the results reported by Simmons, in 1960 [28]. The underlying reason for this crossover behavior is, in the high voltage region, the tilt of the potential barrier changes its direction for the RB condition (Figs. 2.1a and 2.1c). For $(W_2 - X) < eV_g < 20$ eV, the asymmetry between FB and RB characteristics becomes significant. In this region, for the same bias voltage, electrons see a lower effective potential barrier height in RB condition than that in the FB condition (Fig. 2.1). The asymmetry between FB and RB characteristics remains insensitive to the value of W_1 or W_2, when the work function difference ΔW is kept fixed. When V_g approaches 100 V, the net current density for both FB and RB conditions converges to the value of QCL, since the SCL current density depends only on V_g and D, but not on work function. The effect of the electron affinity X of the insulating thin film on $J - V$ characteristics would be similar, that is, increasing X would be equivalent to decreasing W_1 and W_2, provided the relative permittivity ϵ_r of the insulator and the insulator thickness are unchanged.

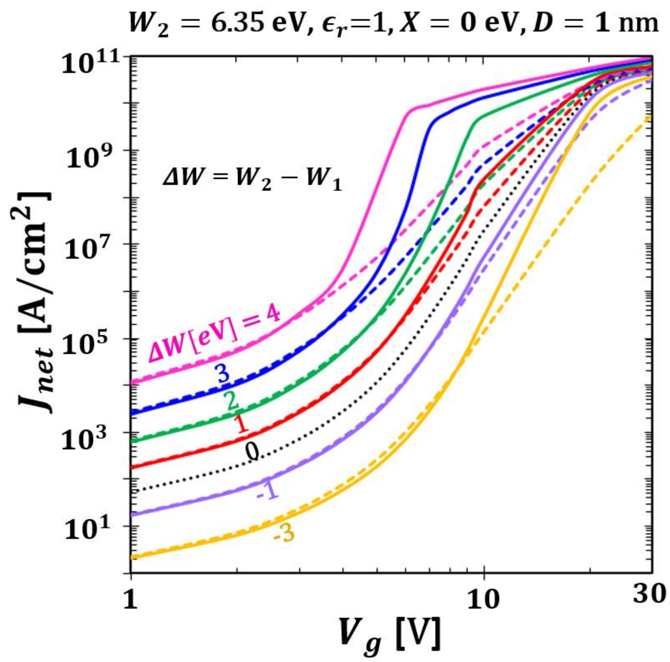

Figure 2.3 The effects of work function difference ΔW on the $J - V$ characteristics of a dissimilar MIM junction with D = 1 nm, vacuum gap (ϵ_r=1, $X = 0$ eV). Top to bottom, ΔW = 4 eV, 3 eV, 2 eV, 1 eV, 0 eV, -1 eV, -3 eV. The work function of metal 2 is kept fixed, W_2 = 6.35eV (Pt). Solid and dashed lines represent RB and FB conditions respectively. [1]

The effects of work function difference ΔW = $W_2 - W_1$ on the $J - V$ characteristics of a MIM junction separated by a 1 nm wide vacuum gap, are shown in Fig. 2.3. The work function of metal 2 is kept fixed, W_2 = 6.35 eV (Pt). Solid and dashed lines represent the RB and FB conditions, respectively. Unlike the previous case of fixed ΔW in Fig. 2.2b, in the field emission regime, the asymmetry between FB and RB currents increases significantly as $|\Delta W|$ increases. Work function difference between the two metal electrodes in a dissimilar MIM junction influences the $J - V$ characteristics more profoundly than the individual work functions. The dotted line in Fig. 2.3 ($\Delta W = 0$) represents the similar MIM junction ($W_1 = W_2 = 6.35$eV) tunneling current density. The curves for J_{net} lie above and below the $\Delta W = 0$ reference, for $W_1 < 6.35$ eV and $W_1 > 6.35$ eV respectively.

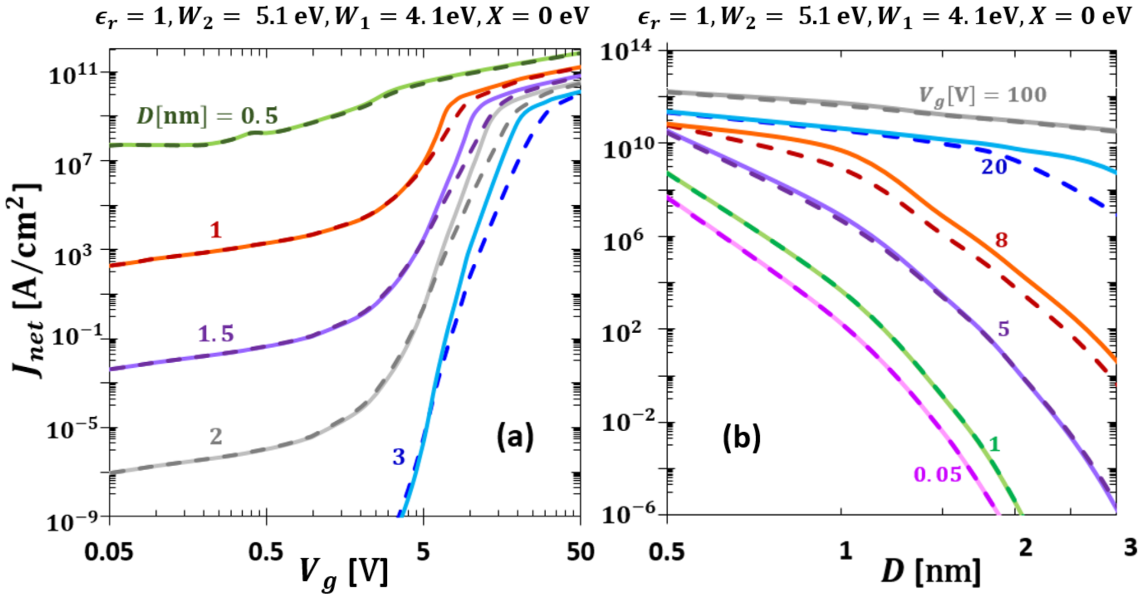

Figure 2.4 The effects of gap width (D) on the $J - V$ characteristics of a dissimilar MIM junction with vacuum gap (a) J_{net} as a function of applied gap voltage V_g. Top to bottom, D = 0.5 nm, 1 nm, 1.5 nm, 2 nm, 3 nm. (b) J_{net} as a function of gap width D for different V_g. Work function of the two electrodes are $W_2 = 5.1$ eV and $W_1 = 4.1$ eV . For the vacuum gap ϵ_r = 1 and $X = 0$ eV. Solid and dashed lines represent RB and FB conditions respectively.

Figure 2.4 shows the effects of gap width (or insulator thickness) D on the tunneling current density in dissimilar MIM junctions. In Fig. 2.4a, RB and FB tunneling current densities are plotted as functions of applied gap voltage V_g for D = 0.5 nm, 1 nm, 1.5 nm, 2 nm and 3 nm. In Fig. 2.4b, tunneling current densities are plotted as functions of D for different externally applied bias voltages V_g. For small gap width ($D = 0.5$ nm in Fig. 2.4a), the asymmetry between FB and RB current densities tend to disappear. However, when D is increased, the asymmetry increases significantly. The FB and RB characteristics tend to crossover at about the same voltage. However, this crossover voltage is not exactly the same for all D (c.f. Fig. 2.4b, $V_g = 5$V), as previously reported by Simmons [28]. Figure 2.4b shows that the asymmetry between the FB and RB tunneling current densities appear only for high voltages. In low voltage regime ($V_g \leq 1$V for our MIM junction current calculations), for any given gap width ($D = 0.5$nm $- 3$nm), the current density profiles are almost identical for the two biases. The asymmetry increases with the applied bias voltage and it tends to disappear as V_g reaches 100V into the SCL regime. Note that, when D is large, the cathode emission current reaches the SCL current at a higher voltage. This explains the increase of asymmetry between FB and RB tunneling densities at high voltages (c.f. Fig. 2.4b, $V_g = 20$V) for large D.

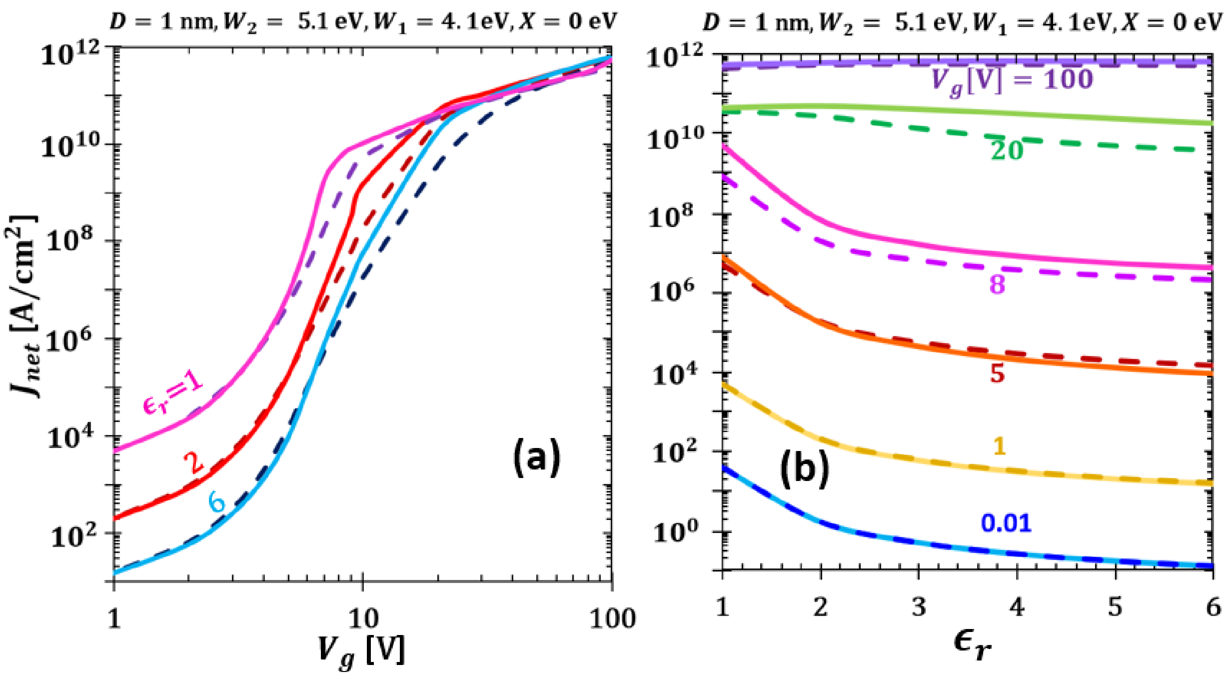

Figure 2.5 The effects of relative permittivity of the insulating thin film ϵ_r on the $J - V$ characteristics of a dissimilar MIM junction with D = 1 nm. (a) J_{net} a function of applied gap voltage V_g. Top to bottom, $\epsilon_r = 1$, 2 and 6 respectively. (b) J_{net} as a function of ϵ_r for different V_g. Work function of the two electrodes are $W_2 = 5.1$ eV and $W_1 = 4.1$ eV . Electron affinity of the insulator is $X = 0$ eV. Solid and dashed lines represent RB and FB conditions respectively.

Figure 2.5 shows the effects of insulator layer permittivity ϵ_r on the tunneling current density in dissimilar MIM junctions. In Fig. 2.5a, RB and FB tunneling current densities are plotted as functions of applied gap voltage V_g for ϵ_r = 1, 2 and 6. In Fig. 2.5b, tunneling current densities are plotted as functions of ϵ_r for different externally applied bias voltages V_g. The relative permittivity of insulating layer greatly influences the image charge potential as well as the space charge potential (Eq. 2.7), which in turn affect the current transport through the potential barrier. The asymmetry between FB and RB tunneling current densities increases with ϵ_r (Fig. 2.5a). However, for low voltages, there is no such asymmetry and the J_{net} profiles are identical, since in this direct tunneling regime the MIM junction is ohmic (Figure 2.5b). The FB and RB characteristics crossover at higher voltages for increasing ϵ_r. It is important to note that, for low and intermediate bias voltages, J_{net} decreases with ϵ_r, but when V_g reaches 100V, this trend reverses because larger ϵ_r reduces the effect of space charge (Eq. 2.7). The asymmetry between FB and RB current densities tend to disappear as V_g reaches the quantum CL limit (Fig. 2.5a and Fig. 2.5b, $V_g = 100\text{V}$).

2.4 Concluding Remarks

Our self-consistent model characterizes the tunneling current in nano- and subnano-scale asymmetric (metal electrodes with dissimilar work functions) MIM junctions, taking into account the effects of both space charge and exchange-correlation potential. It provides accurate estimation of tunneling current density in different regimes over a wide range of input parameters. It is found that the Simmons' formulas provide good approximations of the tunneling current for only a limited parameter space in the direct tunneling regime. Their accuracy decreases when the effective barrier height decreases, where the self-consistent model would give a more accurate evaluation. We demonstrated the influences of electrode work functions (W_1 and W_2), insulator layer properties (ϵ_r, X), insulator thickness (D) and bias voltage (V_g) on the FB and RB tunneling current density profiles. We found that the work function difference ΔW influences the asymmetry between forward and reverse bias $J - V$ characteristics more profoundly than their individual work functions. This asymmetry increases with increasing insulator layer thickness and relative permittivity. However, for very low (for our calculations, $V_g < 1\text{V}$) and very high voltages ($V_g \sim 100\text{V}$), the tunneling current density profiles are almost similar for the two biased cases.

It is worthwhile to note that, although the proposed model is developed for DC condition, it is applicable to the excitation of up to the Near Infrared frequency, since in typical metallic tunnel junctions, the tunneling events occur on a timescale much shorter than the period of the driving fields [48]. The effects of electrodes geometry, possible charge trapping inside the insulator film, frequency dependence will be subjects of future studies.

REFERENCES

REFERENCES

[1] S. Banerjee and P. Zhang, "A generalized self-consistent model for quantum tunneling current in dissimilar metal-insulator-metal junction," *AIP Advances*, vol. 9, no. 8, p. 085302, Aug. 2019, doi: 10.1063/1.5116204.

[2] J. C. Fisher and I. Giaever, "Tunneling Through Thin Insulating Layers," *Journal of Applied Physics*, vol. 32, no. 2, pp. 172–177, Feb. 1961, doi: 10.1063/1.1735973.

[3] J. G. Simmons, "Generalized Formula for the Electric Tunnel Effect between Similar Electrodes Separated by a Thin Insulating Film," *Journal of Applied Physics*, vol. 34, no. 6, pp. 1793–1803, Jun. 1963, doi: 10.1063/1.1702682.

[4] S. Banerjee, J. Luginsland, and P. Zhang, "A Two Dimensional Tunneling Resistance Transmission Line Model for Nanoscale Parallel Electrical Contacts," *Sci Rep*, vol. 9, no. 14484, pp. 1–14, Oct. 2019, doi: 10.1038/s41598-019-50934-2.

[5] Tersoff and S. B. Hamann, "Theory of the scanning tunneling microscope.," *Physical review. B, Condensed matter*, vol. 31, no. 2, pp. 805–813, 1985.

[6] T. L. Cocker *et al.*, "An ultrafast terahertz scanning tunnelling microscope," *Nature Photonics*, vol. 7, no. 8, pp. 620–625, Aug. 2013, doi: 10.1038/nphoton.2013.151.

[7] R. Esteban, A. G. Borisov, P. Nordlander, and J. Aizpurua, "Bridging quantum and classical plasmonics with a quantum-corrected model," *Nature Communications*, vol. 3, p. 825, May 2012, doi: 10.1038/ncomms1806.

[8] K. J. Savage, M. M. Hawkeye, R. Esteban, A. G. Borisov, J. Aizpurua, and J. J. Baumberg, "Revealing the quantum regime in tunnelling plasmonics," *Nature*, vol. 491, no. 7425, pp. 574–577, Nov. 2012, doi: 10.1038/nature11653.

[9] M. S. Tame, K. R. McEnery, S. K. Ozdemir, J. Lee, S. A. Maier, and M. S. Kim, "Quantum Plasmonics," *Nature Physics*, vol. 9, no. 6, pp. 329–340, Jun. 2013, doi: 10.1038/nphys2615.

[10] C. Li, E. T. Thostenson, and T.-W. Chou, "Dominant role of tunneling resistance in the electrical conductivity of carbon nanotube–based composites," *Appl. Phys. Lett.*, vol. 91, no. 22, p. 223114, Nov. 2007, doi: 10.1063/1.2819690.

[11] W. S. Bao, S. A. Meguid, Z. H. Zhu, and G. J. Weng, "Tunneling resistance and its effect on the electrical conductivity of carbon nanotube nanocomposites," *Journal of Applied Physics*, vol. 111, no. 9, p. 093726, May 2012, doi: 10.1063/1.4716010.

[12] N. Hu, Y. Karube, C. Yan, Z. Masuda, and H. Fukunaga, "Tunneling effect in a polymer/carbon nanotube nanocomposite strain sensor," *Acta Materialia*, vol. 56, no. 13, pp. 2929–2936, Aug. 2008, doi: 10.1016/j.actamat.2008.02.030.

[13] P. Zhang *et al.*, “Temperature Comparison of Looped and Vertical Carbon Nanotube Fibers during Field Emission,” *Applied Sciences*, vol. 8, no. 7, p. 1175, Jul. 2018, doi: 10.3390/app8071175.

[14] P. Zhang, S. B. Fairchild, T. C. Back, and Y. Luo, “Field emission from carbon nanotube fibers in varying anode-cathode gap with the consideration of contact resistance,” *AIP Advances*, vol. 7, no. 12, p. 125203, Dec. 2017, doi: 10.1063/1.5008995.

[15] S. Vaziri *et al.*, “Bilayer insulator tunnel barriers for graphene-based vertical hot-electron transistors,” *Nanoscale*, vol. 7, no. 30, pp. 13096–13104, Jul. 2015, doi: 10.1039/C5NR03002A.

[16] V. Enaldiev, A. Bylinkin, and D. Svintsov, “Plasmon-assisted resonant tunneling in graphene-based heterostructures,” *Phys. Rev. B*, vol. 96, no. 12, p. 125437, Sep. 2017, doi: 10.1103/PhysRevB.96.125437.

[17] F. Schwierz, *Two-Dimensional Electronics - Prospects and Challenges*. MDPI, 2018.

[18] M. Houssa, A. Dimoulas, and A. Molle, *2D Materials for Nanoelectronics*. CRC Press, 2016.

[19] P. Zhang, Y. S. Ang, A. L. Garner, Á. Valfells, J. W. Luginsland, and L. K. Ang, “Space–charge limited current in nanodiodes: Ballistic, collisional, and dynamical effects,” *Journal of Applied Physics*, vol. 129, no. 10, p. 100902, Mar. 2021, doi: 10.1063/5.0042355.

[20] P. Zhang and Y. Y. Lau, “Ultrafast and nanoscale diodes,” *Journal of Plasma Physics*, vol. 82, no. 5, Oct. 2016, doi: 10.1017/S002237781600091X.

[21] P. Zhang, Á. Valfells, L. K. Ang, J. W. Luginsland, and Y. Y. Lau, “100 years of the physics of diodes,” *Applied Physics Reviews*, vol. 4, no. 1, p. 011304, Mar. 2017, doi: 10.1063/1.4978231.

[22] J. Lin, P. Y. Wong, P. Yang, Y. Y. Lau, W. Tang, and P. Zhang, “Electric field distribution and current emission in a miniaturized geometrical diode,” *Journal of Applied Physics*, vol. 121, no. 24, p. 244301, Jun. 2017, doi: 10.1063/1.4987127.

[23] Y. Luo and P. Zhang, “Ultrafast strong-field photoelectron emission due to two-color laser fields,” *Phys. Rev. B*, vol. 98, no. 16, p. 165442, Oct. 2018, doi: 10.1103/PhysRevB.98.165442.

[24] D. J. Frank, R. H. Dennard, E. Nowak, P. M. Solomon, and Y. T. and, “Device scaling limits of Si MOSFETs and their application dependencies,” *Proceedings of the IEEE*, vol. 89, no. 3, pp. 259–288, Mar. 2001, doi: 10.1109/5.915374.

[25] A. Seabaugh, “The Tunneling Transistor,” *IEEE Spectrum: Technology, Engineering, and Science News*, Sep. 30, 2013. https://spectrum.ieee.org/semiconductors/devices/the-tunneling-transistor.

[26] P. Zhang, S. Banerjee, and J. Luginsland, “Tunneling Electrical Contacts,” Patent US 10,755,975 B2, Aug. 25, 2020.

[27] P. Zhang, “Scaling for quantum tunneling current in nano- and subnano-scale plasmonic junctions,” *Scientific Reports*, vol. 5, p. 9826, May 2015, doi: 10.1038/srep09826.

[28] J. G. Simmons, “Electric Tunnel Effect between Dissimilar Electrodes Separated by a Thin Insulating Film,” *Journal of Applied Physics*, vol. 34, no. 9, pp. 2581–2590, Sep. 1963, doi: 10.1063/1.1729774.

[29] J. G. Simmons, “Potential Barriers and Emission-Limited Current Flow Between Closely Spaced Parallel Metal Electrodes,” *Journal of Applied Physics*, vol. 35, no. 8, pp. 2472–2481, Aug. 1964, doi: 10.1063/1.1702884.

[30] R. I. Frank and J. G. Simmons, “Space-Charge Effects on Emission-Limited Current Flow in Insulators,” *Journal of Applied Physics*, vol. 38, pp. 832–840, Feb. 1967, doi: 10.1063/1.1709421.

[31] J. G. Simmons, “Conduction in thin dielectric films,” *Journal of Physics D: Applied Physics*, vol. 4, no. 5, pp. 613–657, May 1971, doi: 10.1088/0022-3727/4/5/202.

[32] Y. Y. Lau, D. Chernin, D. G. Colombant, and P.-T. Ho, “Quantum extension of Child-Langmuir law,” *Physical Review Letters*, vol. 66, pp. 1446–1449, Mar. 1991, doi: 10.1103/PhysRevLett.66.1446.

[33] L. K. Ang, T. J. T. Kwan, and Y. Y. Lau, “New Scaling of Child-Langmuir Law in the Quantum Regime,” *Phys. Rev. Lett.*, vol. 91, no. 20, p. 208303, Nov. 2003, doi: 10.1103/PhysRevLett.91.208303.

[34] L. Wu, H. Duan, P. Bai, M. Bosman, J. K. W. Yang, and E. Li, “Fowler-Nordheim tunneling induced charge transfer plasmons between nearly touching nanoparticles,” *ACS Nano*, vol. 7, no. 1, pp. 707–716, Jan. 2013, doi: 10.1021/nn304970v.

[35] L. K. Ang and P. Zhang, “Ultrashort-Pulse Child-Langmuir Law in the Quantum and Relativistic Regimes,” *Phys. Rev. Lett.*, vol. 98, no. 16, p. 164802, Apr. 2007, doi: 10.1103/PhysRevLett.98.164802.

[36] A. Singh, “Improving Current-Asymmetry of Metal-Insulator-Metal Tunnel Junctions,” *FIU Electronic Theses and Dissertations*, Oct. 2016, doi: 10.25148/etd.FIDC001256.

[37] S. Krishnan, S. Bhansali, E. Stefanakos, and Y. Goswami, “Thin Film Metal-Insulator-Metal Junction for Millimeter Wave Detection,” *Procedia Chemistry*, vol. 1, no. 1, pp. 409–412, Sep. 2009, doi: 10.1016/j.proche.2009.07.102.

[38] K. Choi *et al.*, “A Focused Asymmetric Metal–Insulator–Metal Tunneling Diode: Fabrication, DC Characteristics and RF Rectification Analysis,” *IEEE Transactions on Electron Devices*, vol. 58, no. 10, pp. 3519–3528, Oct. 2011, doi: 10.1109/TED.2011.2162414.

[39] S. Banerjee, P. Y. Wong, and P. Zhang, “Contact resistance and current crowding in tunneling type circular nano-contacts,” *J. Phys. D: Appl. Phys.*, vol. 53, no. 35, p. 355301, Jun. 2020, doi: 10.1088/1361-6463/ab8fe0.

[40] S. Banerjee, L. Cao, Y. S. Ang, L. K. Ang, and P. Zhang, “Reducing Contact Resistance in Two-Dimensional-Material-Based Electrical Contacts by Roughness Engineering,” *Phys. Rev. Applied*, vol. 13, no. 6, p. 064021, Jun. 2020, doi: 10.1103/PhysRevApplied.13.064021.

[41] J. P. Perdew and Y. Wang, “Accurate and simple analytic representation of the electron-gas correlation energy,” *Phys. Rev. B*, vol. 45, no. 23, pp. 13244–13249, Jun. 1992, doi: 10.1103/PhysRevB.45.13244.

[42] W. Kohn and L. J. Sham, “Self-Consistent Equations Including Exchange and Correlation Effects,” *Phys. Rev.*, vol. 140, no. 4A, pp. A1133–A1138, Nov. 1965, doi: 10.1103/PhysRev.140.A1133.

[43] P. a. M. Dirac, “Note on Exchange Phenomena in the Thomas Atom,” *Mathematical Proceedings of the Cambridge Philosophical Society*, vol. 26, no. 3, pp. 376–385, Jul. 1930, doi: 10.1017/S0305004100016108.

[44] David Bohm, *Quantum Theory by David Bohm*. 1951.

[45] Omar, *Elementary Solid State Physics.. Principles And Applications M. A. Omar.compressed*. 2016.

[46] C. D. Child, “Discharge From Hot CaO,” *Phys. Rev. (Series I)*, vol. 32, no. 5, pp. 492–511, May 1911, doi: 10.1103/PhysRevSeriesI.32.492.

[47] I. Langmuir, “The Effect of Space Charge and Residual Gases on Thermionic Currents in High Vacuum,” *Phys. Rev.*, vol. 2, no. 6, pp. 450–486, Dec. 1913, doi: 10.1103/PhysRev.2.450.

[48] P. Février and J. Gabelli, “Tunneling time probed by quantum shot noise,” *Nature Communications*, vol. 9, no. 1, p. 4940, Nov. 2018, doi: 10.1038/s41467-018-07369-6.

[49] K. Yoshioka *et al.*, “Real-space coherent manipulation of electrons in a single tunnel junction by single-cycle terahertz electric fields,” *Nature Photonics*, vol. 10, no. 12, pp. 762–765, Dec. 2016, doi: 10.1038/nphoton.2016.205.

[50] A. Rose, “Space-Charge-Limited Currents in Solids,” *Phys. Rev.*, vol. 97, no. 6, pp. 1538–1544, Mar. 1955, doi: 10.1103/PhysRev.97.1538.

[51] E. L. Murphy and R. H. Good, “Thermionic Emission, Field Emission, and the Transition Region,” *Phys. Rev.*, vol. 102, no. 6, pp. 1464–1473, Jun. 1956, doi: 10.1103/PhysRev.102.1464.

[52] R. H. Fowler and L. Nordheim, “Electron Emission in Intense Electric Fields,” *Proceedings of the Royal Society of London. Series A, Containing Papers of a Mathematical and Physical Character*, vol. 119, no. 781, pp. 173–181, 1928.

[53] K. L. Jensen and M. Cahay, “General thermal-field emission equation,” *Appl. Phys. Lett.*, vol. 88, no. 15, p. 154105, Apr. 2006, doi: 10.1063/1.2193776.

CHAPTER 3

PLANAR TUNNELING ELECTRICAL CONTACTS

This chapter is based on the published journal paper "A Two Dimensional Tunneling Resistance Transmission Line Model for Nanoscale Parallel Electrical Contacts," *Sci Rep*, vol. 9, no. 14484, pp. 1–14, Oct. 2019, doi: 10.1038/s41598-019-50934-2, by **S. Banerjee**, J. Luginsland, and P. Zhang [1]. It has been reproduced here with the permission of the copyright holder.

3.1 Introduction

Contact resistance and their electro-thermal effects have become one of the most critical concerns of very large scale integration (VLSI) circuit designers, because of the excessive amount of Joule heating being deposited at the contact region [2]–[7]. The electrical contact properties have been extensively studied in metal-semiconductor [8]–[10], metal-insulator-semiconductor and metal-insulator-metal [11]–[14] junctions. The growing popularity of novel electronic circuits based on graphene, carbon nanotubes (CNTs) and other new materials has made contact engineering crucial. CNT based devices, in particular, experience significant challenges because of the inter-tube connections. On macroscopic level, the exceptional intrinsic electrical properties [15], [16] of CNTs become elusive [4], [15], [17]. Contact resistances between CNTs profoundly affect the electron transport and reduce the electrical conductivity of carbon nanofiber (CNF) [16]–[18], and greatly limit the performance of CNT thin film based Field Effect Transistors (FETs) [19]–[22]. One can naturally expect these issues also arising from other novel two-dimensional materials (boron nitride, molybedenum sulfide, black phosphorus, etc) as well as new nano-composites. While the work presented here is generalizable to these other material systems, here we choose carbon materials as examples.

Tunneling type of electrical contacts[11], [23]–[26] are commonly found for CNT-CNT [17], [25], [27]–[31], CNT-Metal [32]–[34] and CNT-graphene [35][36] contacts, where the contacting members are separated by very thin insulating layers. Tunneling effects in contact junctions significantly lower the electrical conductivity of the CNT/polymer composite thin films [26]. It is also found that tunneling resistance plays a dominant role in the electrical conductivity of CNT-based polymeric or ceramic composites [28].

For decades, the basic models of tunneling current between electrodes separated by thin insulating films have been those of Simmons [37]–[39] in 1960s. Simmon's formula have since been used for evaluating tunneling current in tunneling junctions [24], [30], [40]. Though there have been attempts to extend Simmons' models to the field emission and space-charge-limited regimes [11], [41], [42], it is always assumed that the tunneling junctions are one-dimensional (1D), i.e. there is no variations on the voltages drops along the length of the tunneling junction and the insulating film thickness is uniform. Thus, these existing models of tunneling junctions give no hint on the variation of tunneling current along the contact length and the importance of current crowding near the contact area when the two contacting members are partially overlapping (cf. Fig. 3.1). On the other hand, the widely used transmission line models (TLM) for electrical contacts typically assume the contact resistivity of the interface layers are constant [12], [43]–[45]. It is questionable to apply these models to study the tunneling contacts, as the tunneling resistance depends on the junction voltage that varies spatially along the contact length.

In this chapter, we propose a two-dimensional (2D) transmission line model for partially overlapped parallel contacts with spatially varying specific contact resistivity. Spatial dependence of specific contact resistivity of the contact interface may be introduced by many factors, such as nonuniform distribution of the resistive contaminants, oxides, or foreign objects at the contact interface, formation of contact interfaces with spatially varying thickness, or the presence of tunneling contacts between contact members. In the latter case, because of the nonlinear current-voltage characteristics of the tunneling junctions [11], [37], the specific resistivity along the contact length will become spatially dependent, even for a tunneling layer with uniform thickness (Fig. 3.1). For the tunneling-type contacts, the model considers the variation of potential barrier height and tunneling current along the contact length, by solving the TLM equations coupled with the tunneling current self consistently. We provide comprehensive analysis of the effects of contact geometry (i.e. dimension of the contact, and distance between the contact electrodes), and material properties (i.e. work function, sheet resistance of the contact members, and permittivity of the insulating layer) on the spatial distributions of currents and voltages across these contacts, and the overall contact resistance of parallel contacts.

The formulation of our Cartesian TLM model are given in Sec. 3.2. We would like to point out that, albeit an application of the standard transmission line theory based on the Kirchhoff's laws, the TLM has been used extensively with great success to characterize mesoscale and nanoscale electrical contacts. Here we further extend the TLM model with the effects of spatially dependent contact resistivity. We have considered three cases of Cartesian parallel contacts in Sec. 3.3: 1) constant specific contact resistivity (Sec. 3.3.1); 2) linearly varying specific contact resistivity (Sec. 3.3.2); and 3) tunneling contact resistivity depending on local junction voltages along the contact length (Sec. 3.3.3). The first case of uniform specific contact resistivity along the contact length has been verified with COMSOL [46] 2D simulations. For the third case, for simplicity, we use the Simmons' model to determine the local current-voltage characteristics across the tunneling junction. Though full scale quantum mechanical calculations may have to be used to accurately evaluate the nanoscale circuits, our model based on Simmons formula reveals the fundamental scalings and parametric dependence of current and voltage profiles, as well as electric contact resistance of tunneling contacts. Concluding remarks are given in Section 3.4.

Note that, although this work is focused on the normal Schrodinger tunneling type electrical contacts, the proposed TLM with spatially varying contact resistivity can be used for many other types of electric contacts, such as nanoscale Schottky contacts based on 2D materials heterostructure[47], [48], and Klein tunneling junctions[49].

3.2 The 2D Transmission Line Model

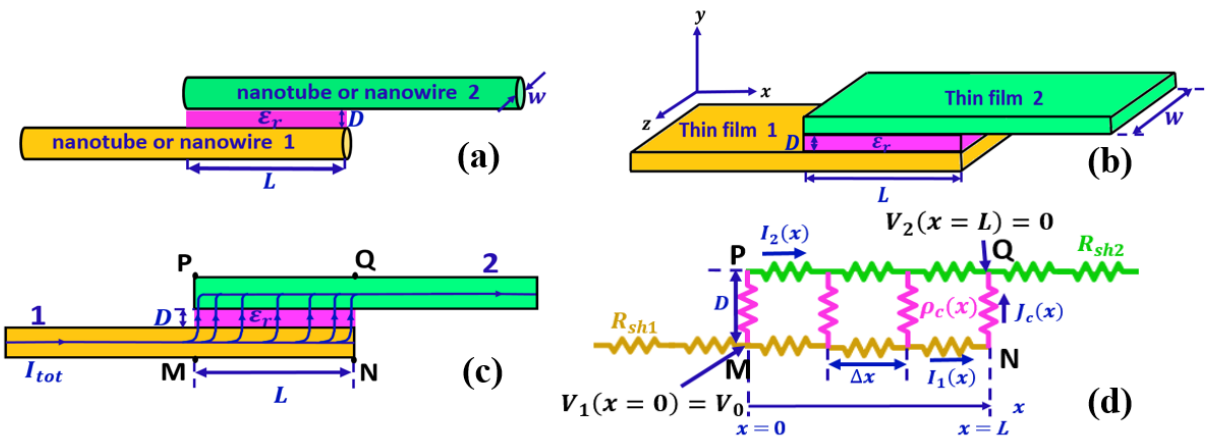

Figure 3.1 A parallel, partially overlapped electric contact. The contacts are formed between (a) nanotube or nanowire 1 and 2, and (b) thin film 1 and 2; (c) side view of the contact; (d) its transmission line model. In (a), (b) and (c) a thin resistive interface layer (or a tunneling layer of permittivity ε_r) is sandwiched between the two contacting members.

Consider a parallel contact formed between two nanowires or nanotubes or between two conducting thin films or layers, as shown in Figs. 3.1(a) and 3.1(b), respectively. The distance between the two contact members is D, and the contact length is L. A thin resistive interface layer is sandwiched between them. Both contacts in Figs. 3.1(a) and 3.1(b) can be described by a two-dimensional (2D) model, as shown in Fig. 3.1(c). Note that the proposed formulation is generally applicable to parallel Cartesian nanojunctions with different shape of the electrodes, for example, electrical contact between a nanowire and a thin film. In the 2D model, the effects of the transverse dimension (perpendicular to the paper) can be included in the effective sheet resistances R_{sh1} and R_{sh2} for conductor 1 and 2, respectively, such that there is no variation along the width w in the transverse dimension. The spatial dependent specific interfacial resistivity (also termed specific contact resistivity) is $\rho_c(x)$, which is either predefined, or calculated from the local tunneling current in case of insulating tunneling layer [37]–[39]. We use the DC equivalent lump circuit transmission line model (TLM) [12], [43]–[45], as shown in Fig. 3.1(d), to model the 2D parallel contact in Fig. 3.1(c).

In the contact region PQNM in Figs. 3.1(c) and 3.1(d), using Kirchoff's laws for current and voltage, we get the following equations,

$$I_1(x) - I_1(x + \Delta x) = \frac{V_1(x) - V_2(x)}{\rho_c(x)} \Delta x\, w, \tag{3.1a}$$

$$V_1(x) - V_1(x + \Delta x) = I_1(x)\; R_{sh1} \Delta x / w, \tag{3.1b}$$

$$I_2(x + \Delta x) - I_2(x) = \frac{V_1(x) - V_2(x)}{\rho_c(x)} \Delta x\, w, \tag{3.1c}$$

$$V_2(x) - V_2(x + \Delta x) = I_2(x)\; R_{sh2} \Delta x / w, \tag{3.1d}$$

where $I_1(x)$ and $I_2(x)$ represent the current flowing at x through the lower contact member, MN and upper contact member, PQ respectively, and $V_1(x)$ and $V_2(x)$ the local voltage at x along MN and PQ, respectively, and w is the effective transverse dimension of the contacts. When $\Delta x \to 0$, Equation (3.1) becomes,

$$\frac{\partial I_1(x)}{\partial x} = -w J_c(x), \tag{3.2a}$$

$$\frac{\partial V_1(x)}{\partial x} = -\frac{I_1(x)R_{sh1}}{w}, \tag{3.2b}$$

$$\frac{\partial I_2(x)}{\partial x} = wJ_c(x), \tag{3.2c}$$

$$\frac{\partial V_2(x)}{\partial x} = -\frac{I_2(x)R_{sh2}}{w}, \tag{3.2d}$$

where $J_c(x) = V_g(x)/\rho_c(x)$ and $V_g(x) = V_1(x) - V_2(x)$ are the local current density and the local voltage drop across the contact interface at x, respectively.

Note that, from Eqs. (3.2a) and (3.2c), $I_1(x) + I_2(x) = I_{tot} =$ constant, where I_{tot} is the total current in the circuit, to be determined from the boundary conditions. The boundary conditions for Eq. (3.2) are,

$$V_1(x = 0) = V_o, \tag{3.3a}$$

$$I_2(x = 0) = 0, \tag{3.3b}$$

$$I_1(x = L) = 0, \tag{3.3c}$$

$$V_2(x = L) = 0, \tag{3.3d}$$

where, without loss of generality, we assume the voltage of the upper contact member at $x = L$ is 0, and the externally applied voltage at $x = 0$ of the lower contact member is V_0. Note that $I_1(x = 0) = I_{tot}$, and $I_2(x = 0) = 0$. From Eqs. (3.2) and (3.3), it is easy to show $V_1'(x = 0) = -I_{tot}R_{sh1}/w$, $V_1'(x = L) = 0$, $V_2'(x = 0) = 0$, $V_2'(x = L) = -I_{tot}R_{sh2}/w$, where a prime denotes a derivative with respect to x. For the contact model in Fig. 3.1(d), the contact resistance is defined as,

$$R_c = \frac{V_1(0) - V_2(L)}{I_{tot}} = \frac{V_o}{I_{tot}}. \tag{3.4}$$

It is convenient to introduce non-dimensional quantities, $\bar{x} = x/L$, $\bar{\rho}_c(\bar{x}) = \rho_c(x)/\rho_{c0}$, $\bar{R}_{sh2} = R_{sh2}/R_{sh1}$, $\overline{I_1}(\bar{x}) = I_1(x)/I_o$, $\overline{I_2}(\bar{x}) = I_2(x)/I_o$, $\overline{J_c}(\bar{x}) = J_c(x)LW/I_o$, $\overline{V_1}(\bar{x}) = V_1(x)/V_o$, $\overline{V_2}(\bar{x}) = V_2(x)/V_o$, $\overline{V_g}(\bar{x}) = V_g(x)/V_o$, and $\overline{R_c} = R_c/R_{c0}$, where we define $I_o = wV_0/R_{sh1}L$, $\rho_{c0} = V_0 wL/I_o$, and $R_{c0} = R_{sh1}L/w$. In normalized forms, Eq. (3.2) can be recast into the following second order differential equations,

$$\frac{\partial^2 \overline{V_1}(\bar{x})}{\partial \bar{x}^2} = \bar{J}_c(\bar{x}), \tag{3.5a}$$

$$\frac{\partial^2 \overline{V}_g(\bar{x})}{\partial \bar{x}^2} = (1 + \bar{R}_{sh2})\bar{J}_c(\bar{x}), \tag{3.5b}$$

$$\bar{\rho}_c(\bar{x})\frac{\partial^2 \overline{I_1}(\bar{x})}{\partial \bar{x}^2} + \frac{\partial \bar{\rho}_c(\bar{x})}{\partial \bar{x}}\frac{\partial \overline{I_1}(\bar{x})}{\partial \bar{x}} - (1 + \bar{R}_{sh2})\,\overline{I_1}(\bar{x}) + \alpha \bar{R}_{sh2} = 0, \tag{3.5c}$$

where $\overline{J_c}(\bar{x}) = \overline{V_g}(\bar{x})/\bar{\rho}_c(\bar{x})$, and $\overline{V_g}(\bar{x}) = \overline{V_1}(\bar{x}) - \overline{V_2}(\bar{x})$. The corresponding boundary conditions to Eqs. 3.5(a)-3.5(c) are respectively,

$$\overline{V_1}(\bar{x} = 0) = 1\ , \overline{V_1}'(\bar{x} = 0) = -\alpha \text{ and } \overline{V_1}(\bar{x} = 1) = \overline{V_g}(\bar{x} = 1), \tag{3.6a}$$

$$\overline{V_g}'(\bar{x} = 0) = -\alpha\ ,\ \ \overline{V_g}'(\bar{x} = 1) = \alpha \bar{R}_{sh2}, \tag{3.6b}$$

$$\overline{I_1}(\bar{x} = 0) = \alpha, \qquad \overline{I_1}(\bar{x} = 1) = 0\ , \tag{3.6c}$$

where the unknown constant $\alpha = I_{tot}/I_o$ is the normalized total current in the circuit, and prime denotes a derivative with respect to $\bar{x}$. Note that integrating Eq. (3.5b) subject to Eq. (3.6b) gives $\int_0^1 \overline{J_c}(\bar{x}) d\bar{x} = \alpha$, which means that the total current is conserved across the contact interface.

Equations (3.5) and (3.6) are solved to give the voltage and current distribution along and across the contact interface as well as the total contact resistance, for a given electrical contact (Fig. 3.1) with spatially dependent interface specific contact resistivity $\bar{\rho}_c(\bar{x})$. An example of the procedure to solve Eqs. (3.5) and (3.6) numerically is as follows. For an initially guess on α, Eq (3.5b) is solved using the shooting method, subject to Eq. (3.6b). Next, Eq (3.5a) is solved with the initial values of $\overline{V_1}(0)$ and $\overline{V_1}'(0)$ from Eq. (3.6a). It is then checked whether $\overline{V_1}(1)$ is equal to $\overline{V_g}(1)$, as in Eq. (3.6a). The above-mentioned process repeats for different input α until the condition $\overline{V_1}(1) = \overline{V_g}(1)$ is satisfied. Finally, Eq (3.5c) is solved to get $\overline{I_1}$ (and $\overline{I_2}$).

In principle, Eqs. (3.5) and (3.6) can be solved numerically for arbitrary spatial dependence of specific contact resistivity $\bar{\rho}_c(\bar{x})$. Here, we focus on a few special cases of practical importance. We first consider the case of constant $\bar{\rho}_c$, where analytical solutions can be obtained (Sec. 3.3.1), which also serve to validate our numerical approach. We then consider the effects of spatially dependent $\bar{\rho}_c(\bar{x})$ on the parallel electrical contacts. We focus on two situations: linearly varying specific contact resistivity along x (Sec. 3.3.2), and thin tunneling junction with uniform thickness (Sec. 3.3.3), where analytical solutions to the TLM current and voltage equations are no longer available, and Eqs. (3.5) and (3.6) are solved numerically.

3.3 Results and Discussion

3.3.1 Constant specific contact resistivity along the contact length

For the special case of constant specific contact resistivity ρ_c, the TLM equations, Eqs. (3.5) and (3.6), can be solved analytically to give,

$$\overline{I_1}(\bar{x}) = \frac{q}{K}\left[\sinh q(1-\bar{x}) + \bar{R}_{sh2}(\sinh q - \sinh q\bar{x})\right] \tag{3.7a}$$

$$\overline{I_2}(\bar{x}) = \frac{q}{K}\left[\sinh q(\bar{x}-1) + \bar{R}_{sh2}\sinh q\bar{x} + \sinh q\right] \tag{3.7b}$$

$$\overline{J_c}(\bar{x}) = \frac{q^2}{K}\left[\cosh q(1-\bar{x}) + \bar{R}_{sh2}\cosh q\bar{x}\right] \tag{3.7c}$$

$$\bar{V}_1(\bar{x}) = \frac{1}{K}[\cosh q(1-\bar{x}) + \bar{R}_{sh2}M + \bar{R}_{sh2}q(1-\bar{x})\sinh q] \tag{3.7d}$$

$$\bar{V}_2(\bar{x}) = \bar{V}_1(\bar{x}) - \bar{\rho}_c\bar{J}_c(\bar{x}) \tag{3.7e}$$

and $$\overline{R_c} = \frac{\left(1+\bar{R}_{sh2}{}^2\right)\cosh q + \bar{R}_{sh2}(2+q\sinh q)}{(1+\bar{R}_{sh2})q\sinh q} \tag{3.8}$$

where $q = \frac{L}{\lambda_0} = \sqrt{\frac{1+\bar{R}_{sh2}}{\bar{\rho}_c}}$, $K = \left(1+\bar{R}_{sh2}{}^2\right)\cosh q + \bar{R}_{sh2}(2+q\sinh q)$ and $M = \cosh q\bar{x} + 1 + \bar{R}_{sh2}\cosh q$.

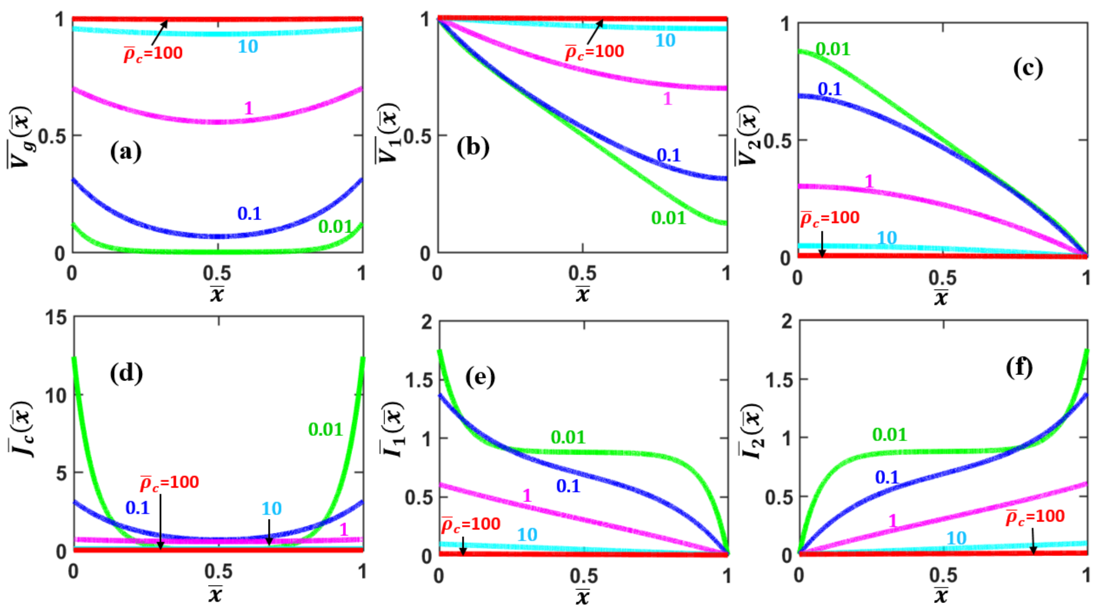

Figure 3.2 (a) Voltage drop across the contact interface $\overline{V_g}(\bar{x})$, voltage along (b) contact member 1 (MN), $\overline{V_1}(\bar{x})$, (c) contact member 2 (PQ), $\overline{V_2}(\bar{x})$, (d) current density across the contact interface $\overline{J_c}(\bar{x})$, current along (e) contact member 1, $\overline{I_1}(\bar{x})$, and (f) contact member 2, $\overline{I_2}(\bar{x})$,for different values of specific contact resistivity $\bar{\rho}_c$, for $\bar{R}_{sh2} = R_{sh2}/R_{sh1} = 1$. All the quantities are in their normalized forms defined in Sec. 3.2. [1]

Figure 3.2 shows the current and voltage distributions along the contact length and across the contact interface for various specific contact resistivity $\bar{\rho}_c$, for a parallel contact formed between similar contact members, $\bar{R}_{sh2} = R_{sh2}/R_{sh1} = 1$. The voltage along both contact members $\bar{V}_1$ and $\bar{V}_2$ decrease with $\bar{x}$, as shown in Figs. 3.2(b) and 3.2(c), respectively. The current $\bar{I}_1$ in contact member 1 decreases with $\bar{x}$ (Fig. 3.2(e)), whereas $\overline{I_2}$ in contact member 2 increases with $\bar{x}$ (Fig. 3.2(f)), with the total current $\overline{I_1}(\bar{x}) + \overline{I_2}(\bar{x})$ being kept a constant along $\bar{x}$. The profiles of both normalized voltage drop $\overline{V_g}(\bar{x})$ and current density $\overline{J_C}(\bar{x})$ across the interface layer, are symmetric along the contact length, with the minimum at the center of the contact structure $\bar{x} = 0.5$ and the maximum at the contact edges, as shown in Figs. 3.2(a) and 3.2(d), respectively. The current crowding effects near the contact edges are well-known phenomena, as the current density is distributed to follow the least resistive path (i.e. minimum overall resistance). It is important to note that as the specific contact resistivity $\bar{\rho}_c$ decreases, the interface current density $\overline{J_c}$ becomes more crowded towards the contact edges, as shown in Fig. 3.2(d). In other words, the less resistive the contact interface layer, the more severe of the current crowding effects, which is in agreement with previous studies using both TLM [44], [45] and field theory [12], [50], [51].

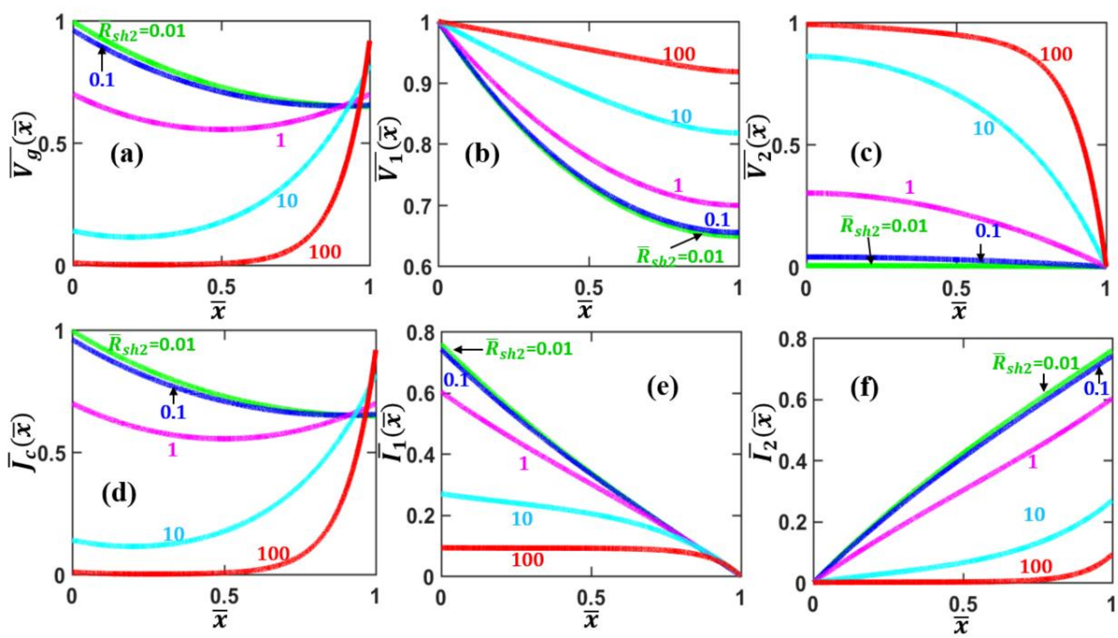

Figure 3.3 (a) Voltage drop across the contact interface $\overline{V_g}(\bar{x})$, voltage along (b) contact member 1 (MN), $\overline{V_1}(\bar{x})$, and (c) contact member 2 (PQ), $\overline{V_2}(\bar{x})$, (d) current density across the contact interface $\overline{J_c}(\bar{x})$, current along (e) contact member 1, $\overline{I_1}(\bar{x})$, and (f) contact member 2, $\overline{I_2}(\bar{x})$, for different values of $\bar{R}_{sh2} = R_{sh2}/R_{sh1}$, for $\bar{\rho}_c = 1$. All the quantities are in their normalized forms defined in Sec. 3.2. [1]

Figure 3.3 shows the current and voltage distributions along the contact length and across the contact interface for various parallel contacts formed between dissimilar materials, $\bar{R}_{sh2} = R_{sh2}/R_{sh1}$, with fixed specific contact resistivity $\bar{\rho}_c = 1$. The voltage $\overline{V_{1,2}}$ and the current $\overline{I_{1,2}}$ along the two contact members show similar behaviors as those in Fig. 3.2. However, the voltage drop across the interface layer $\overline{V_g}(\bar{x})$ and the contact current density $\overline{J_c}(\bar{x})$ are no longer symmetric, as shown in Figs. 3.3(a) and 3.3(d), respectively. When $\bar{R}_{sh2} < 1$, the maximum of $\overline{V_g}(\bar{x})$ and $\overline{J_c}(\bar{x})$ occurs at $\bar{x} = 0$; when $\bar{R}_{sh2} > 1$, the maximum of $\overline{V_g}(\bar{x})$ and $\overline{J_c}(\bar{x})$ occurs at $\bar{x} = 1$. This current crowding effect can again be explained by the fact that current flows are self-arranged to take the least resistive path in the circuit by adjusting the current distribution according to the local resistance.

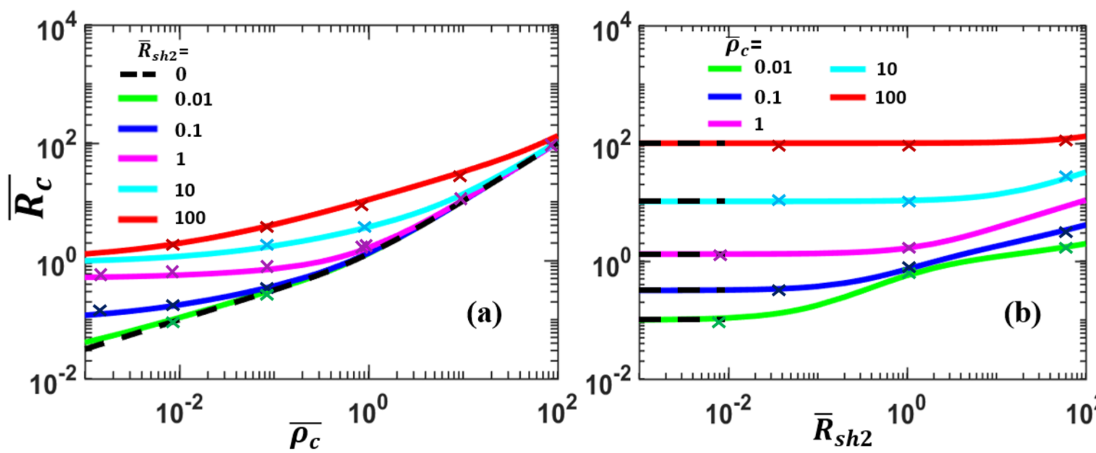

Figure 3.4 Normalized contact resistance $\overline{R_c}$ of the parallel contact (Fig. 3.1). $\overline{R_c}$ as a function of (a) normalized specific contact resistivity, $\bar{\rho}_c$ and (b) normalized sheet resistance of contacting member 2, $\bar{R}_{sh2}$. Dashed lines are for Eq. (3.9), the limiting case of $\bar{R}_{sh2} \to 0$. The cross symbols are from COMSOL[46] 2D simulations. The length and height of both upper and lower contacting members are assumed to be 20 nm and 10 nm respectively, and the thickness of the resistive interfacial layer is assumed to be 0.5 nm. The resistivities of the upper and lower contact members are in the range of $10^{-9}\Omega\text{m} - 10^{-7}\Omega\text{m}$, and the resistivity of the interface layer is in the range of $10^{-9}\Omega\text{m} - 10^{-5}\Omega\text{m}$. [1]

The normalized contact resistance, $\overline{R_c}$ calculated from Eq. (3.8) is plotted in Fig. 3.4 for various $\bar{\rho}_c$ and $\bar{R}_{sh2}$. It is clear that $\overline{R_c}$ increases with both $\bar{\rho}_c$ and $\bar{R}_{sh2}$. In general, the contact resistance $\overline{R_c}$ depends more strongly on the the specific contact resistivity of the interfacial layer $\bar{\rho}_c$ than on the sheet resistance ratio of the contact members $\bar{R}_{sh2}$. For the special case of $\bar{R}_{sh2} = 0$, Eq. (3.8) becomes,

$$\overline{R_c} = \frac{\coth q}{q}, \tag{3.9}$$

with $q = L/\lambda_0 = 1/\sqrt{\bar{\rho}_c}$, which is also plotted in Fig. 3.4. Note that Eq. (3.9) is identical to the expression typically used for metal-semiconductor contact.

To verify the results obtained from our analytical solution, we performed numerical simulations using the COMSOL multiphysics software[46], for various combinations of $\bar{R}_{sh2}$ and $\bar{\rho}_c$ on the geometry shown in Fig. 3.1. The finite-element-method (FEM) based COMSOL 2D simulation results are included in Fig. 3.4 (cross symbols), showing excellent agreement with our theory. The convergence iteration error was less than 10^{-9} for each point.

3.3.2 Specific contact resistivity varies linearly along the contact length

We assume the specific resistivity varies linearly along the contact length (Fig. 3.1) as $\bar{\rho}_c(\bar{x}) = 1 + A\bar{x}$. By solving Eqs. (3.5) and (3.6) numerically, we obtain the current and voltage distributions along the contact interface, as shown in Fig. 3.5. As A increases, the overall contact interface becomes more resistive, therefore, the voltage drop $\overline{V_g}(\bar{x})$ across the interface layer increases (Fig. 3.5a), whereas the current density $\overline{J_C}(\bar{x})$ across the interface layer decreases in general (Fig. 3.5d). The maximum $\overline{V_g}$ occurs at the contact edge with the highest specific resistivity

$\bar{\rho}_c$ (i.e., at $\bar{x} = 0$ when $A < 0$, and at $\bar{x} = 1$ when $A > 0$), while the maximum interface current $\overline{J_C}$ occurs at the contact edge with the lowest $\bar{\rho}_c$ (i.e., at $\bar{x} = 1$ when $A < 0$, and at $\bar{x} = 0$ when $A > 0$). The effects of A on the voltage $\overline{V_{1,2}}$ and the current $\overline{I_{1,2}}$ along the two contact members are also shown in Figs. 3.5 (b), (c), (e) and (f), respectively.

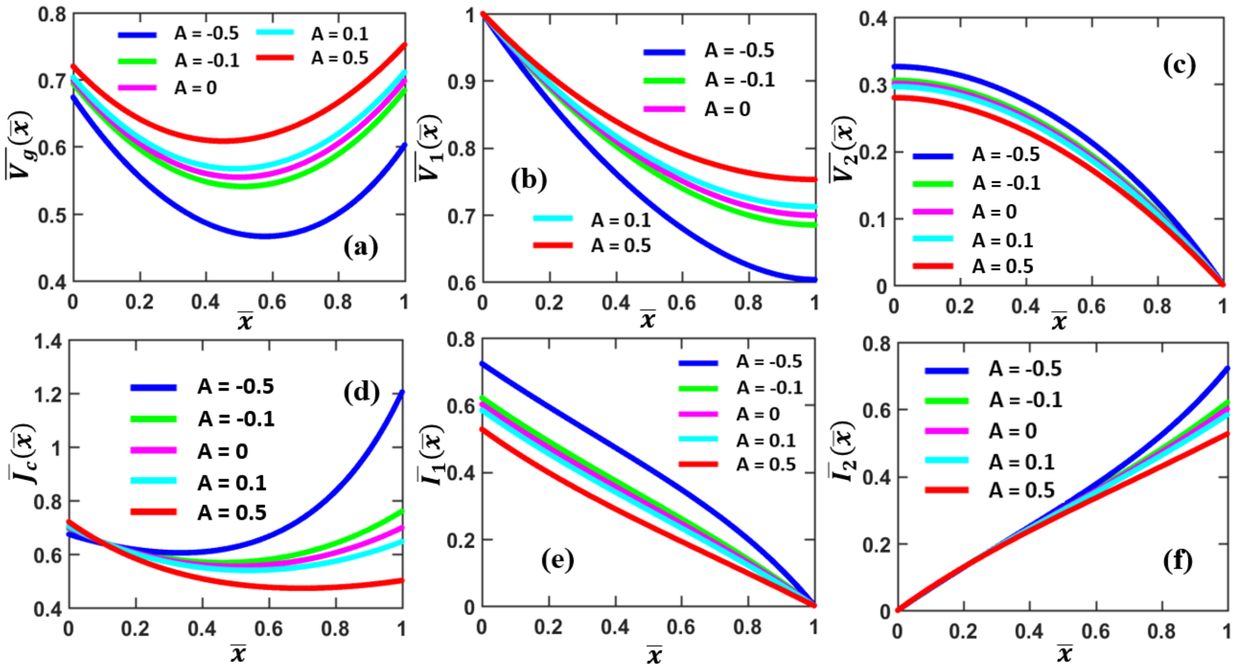

Figure 3.5 (a) Voltage drop across the contact interface $\overline{V_g}(\bar{x})$, voltage along (b) contact member 1 (MN), $\overline{V_1}(\bar{x})$, and (c) contact member 2 (PQ), $\overline{V_2}(\bar{x})$, (d) current density across the contact interface $\overline{J_c}(\bar{x})$, current along (e) contact member 1, $\overline{I_1}(\bar{x})$, and (f) contact member 2, $\overline{I_2}(\bar{x})$, for linear specific contact resistivity $\bar{\rho}_c(\bar{x}) = 1 + A\bar{x}$ with different linear constant A, for $\bar{R}_{sh2} = R_{sh2}/R_{sh1} = 1$. All the quantities are in their normalized forms defined in Sec. 3.2. [1]

The normalized contact resistance, $\overline{R_c}$ calculated from Eq. (3.4) for linear specific contact resistivity $\bar{\rho}_c(\bar{x}) = 1 + A\bar{x}$ is plotted in Fig. 3.6. As A increases, $\overline{R_c}$ increases, since the contact interface becomes more resistive. As $\bar{R}_{sh2}$ increases, the contact resistance $\overline{R_c}$ depends more strongly on the linear constant A.

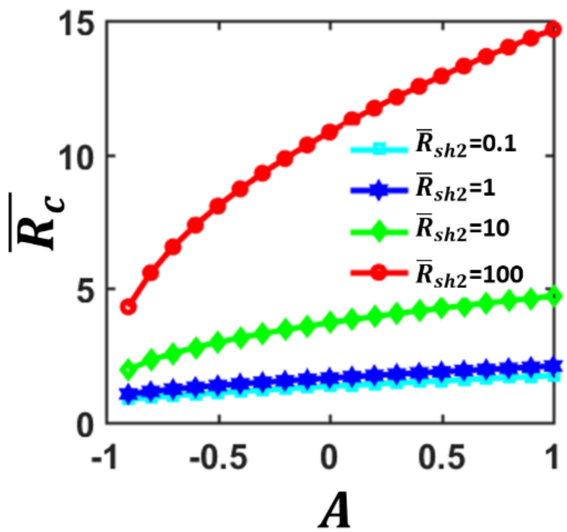

Figure 3.6 Normalized contact resistance $\overline{R_c}$ of the parallel contact (Fig. 3.1) with linear specific contact resistivity $\bar{\rho}_c(\bar{x}) = 1 + A\bar{x}$, for various value of $\bar{R}_{sh2} = R_{sh2}/R_{sh1}$. [1]

3.3.3 Tunneling contact resistance

Here, we assume the parallel contacts are formed through a tunneling interface layer between the two contact members. For simplicity, we have made the following assumptions: 1) the thickness of interfacial insulating film in the contact area is uniform, and 2) the insulating film is sufficiently thin (in the nano- or subnano-meter scale) so that charge trappings are ignored [52][53].

For dissimilar contact members, the (normalized) current density at any location along the contact from contact member 1 to contact member 2 is calculated using Simmons' formula [38],

$$\bar{J}_c(\bar{x}) = B\left[\bar{\varphi}_I e^{-A\Delta\bar{y}\sqrt{\bar{\varphi}_I}} - \left(\bar{\varphi}_I + \bar{V}_g(\bar{x})\right) e^{-A\Delta\bar{y}\sqrt{\bar{\varphi}_I + \bar{V}_g(\bar{x})}}\right] \quad (3.10)$$

where $\bar{V}_g(\bar{x}) = \bar{V}_1(\bar{x}) - \bar{V}_2(\bar{x})$ is the local voltage drop across the contact interface at $\bar{x}$, A $=$ $1.025\sqrt{eV_0\ [\mathrm{eV}]}D[\text{Å}]$, $B = 615\frac{L^2[\mu m]R_{sh1}[\Omega/\square]}{D^2[\text{Å}](\Delta\bar{y})^2}$ and $\Delta\bar{y} = \bar{y}_2 - \bar{y}_1$. Definitions of $\bar{\varphi}_I$, $\bar{y}_1$ and $\bar{y}_2$

for forward bias (when lower work function contacting member is given positive bias) are given below, $\bar{\varphi}_I = \bar{\varphi}_2 - (\bar{V_g}(\bar{x}) + \Delta\bar{\varphi})\frac{\bar{y}_1+\bar{y}_2}{2} - \frac{1.15\bar{\lambda}}{\bar{y}_2-\bar{y}_1}\ln\left(\frac{\bar{y}_2(1-\bar{y}_1)}{\bar{y}_1(1-\bar{y}_2)}\right)$, where $\Delta\bar{\varphi} = \bar{\varphi}_2 - \bar{\varphi}_1$, $\bar{\varphi}_1 = \frac{\varphi_1}{eV_0}$, $\bar{\varphi}_2 = \frac{\varphi_2}{eV_0}$, $\varphi_1 = W_1 - \chi$ and $\varphi_2 = W_2 - \chi$. W_1 and W_2 are the work functions of contacting member 1 and 2 respectively, χ is the electron affinity of the insulating layer, which is 0 for vacuum. For $\bar{V_g}(\bar{x}) \leq \bar{\varphi}_1$: $\bar{y}_1 = \frac{1.2\ \bar{\lambda}}{\bar{\varphi}_2}$, $\bar{y}_2 = 1 - \frac{9.2\bar{\lambda}}{3\bar{\varphi}_2+4\bar{\lambda}-2(\bar{V_g}(\bar{x})+\Delta\bar{\varphi})} + \bar{y}_1$; and for $\bar{V_g}(\bar{x}) > \bar{\varphi}_1$: $\bar{y}_1 = \frac{1.2\ \bar{\lambda}}{\bar{\varphi}_2}$, $\bar{y}_2 = \frac{\bar{\varphi}_2-5.6\bar{\lambda}}{(\bar{V_g}(\bar{x})+\Delta\bar{\varphi})}$, where $\bar{\lambda} = \frac{2.49}{\varepsilon_r D[\text{Å}] eV_0[\text{eV}]}$.

On the other hand, the definitions of $\bar{\varphi}_I$, $\bar{y}_1$ and $\bar{y}_2$ for reverse bias (when higher work function contacting member is given positive bias) are: $\bar{\varphi}_I = \bar{\varphi}_1 + \left(\Delta\bar{\varphi} - \bar{V_g}(\bar{x})\right)\frac{\bar{y}_1+\bar{y}_2}{2} - \frac{1.15\bar{\lambda}}{\bar{y}_2-\bar{y}_1}\ln\left(\frac{\bar{y}_2(1-\bar{y}_1)}{\bar{y}_1(1-\bar{y}_2)}\right)$, for $0 < \bar{V_g}(\bar{x}) \leq \Delta\bar{\varphi}$: $\bar{y}_1 = \frac{9.2\bar{\lambda}}{3\bar{\varphi}_1+4\bar{\lambda}-(\bar{V_g}(\bar{x})-\Delta\bar{\varphi})} - \frac{1.2\ \bar{\lambda}}{\bar{\varphi}_2-\bar{V_g}(\bar{x})}$, $\bar{y}_2 = 1 - \frac{1.2\ \bar{\lambda}}{\bar{\varphi}_2-\bar{V_g}(\bar{x})}$; for $\Delta\bar{\varphi} < \bar{V_g}(\bar{x}) \leq \bar{\varphi}_2$: $\bar{y}_1 = \frac{1.2\ \bar{\lambda}}{\bar{\varphi}_1}$, $\bar{y}_2 = 1 - \frac{9.2\bar{\lambda}}{3\bar{\varphi}_1+4\bar{\lambda}-2(\bar{V_g}(\bar{x})-\Delta\bar{\varphi})} + \bar{y}_1$; and for $\bar{V_g}(\bar{x}) > \bar{\varphi}_2$: $\bar{y}_1 = \frac{1.2\ \bar{\lambda}}{\bar{\varphi}_1}$, $\bar{y}_2 = \frac{\bar{\varphi}_1-5.6\bar{\lambda}}{(\bar{V_g}(\bar{x})-\Delta\bar{\varphi})}$.

For the special case of the same material for contact members 1 and 2, in Eq. (3.10), $\bar{\varphi}_I = \bar{\varphi}_0 - \bar{V_g}(\bar{x})\frac{\bar{y}_1+\bar{y}_2}{2} - \frac{1.15\bar{\lambda}}{\bar{y}_2-\bar{y}_1}\ln\left(\frac{\bar{y}_2(1-\bar{y}_1)}{\bar{y}_1(1-\bar{y}_2)}\right)$ where $\bar{\varphi}_0 = \frac{\varphi_0}{eV_0}$, $\varphi_0 = W - \chi$, W is the work function of contacting member 1 and 2, and, $\bar{y}_1 = \frac{1.2\ \bar{\lambda}}{\bar{\varphi}_0}$, $\bar{y}_2 = 1 - \frac{9.2\bar{\lambda}}{3\bar{\varphi}_0+4\bar{\lambda}-2\bar{V_g}(\bar{x})} + \bar{y}_1$ for $\bar{V_g}(\bar{x}) \leq \bar{\varphi}_0$, $\bar{y}_2 = \frac{\bar{\varphi}_0-5.6\bar{\lambda}}{\bar{V_g}(\bar{x})}$ for $\bar{V_g}(\bar{x}) \leq \bar{\varphi}_0$. Note that we use Simmon's formula, Eq. (3.10) here for simplicity, which is reliable only when the barrier height is relative high and the gap voltage is low in the direct tunneling regime [11], [23]. More accurate results for the tunneling current may be calculated using quantum models developed in Chapter 2 by solving the coupled Schrodinger equation and Poisson equation with the inclusion of space charge and exchange-correlation effects [11], [23].

We keep the normalization consistent with our previous calculations in Sec. 3.2. For a given parallel tunneling contact (Fig. 3.1), the inputs of our model are the applied voltage V_0, sheet resistance (R_{sh1}, R_{sh2}) and work function (W_1, W_2) of contacting members 1 and 2, permittivity (ε_r), thickness (D), and electron affinity (χ) of the interfacial insulator layer, and the contact length L. Using Eq. (3.10), the specific contact resistivity is obtained from $\bar{\rho}_c(\bar{x}) = \overline{V_g}(\bar{x})/\overline{J_c}(\bar{x})$, which is inserted into the TLM equations, Eqs. (3.5) and (3.6), to give a self-consistent solution to the voltage and current profiles, as well as the contact resistance for the parallel tunneling contact.

We consider CNT-vacuum-CNT parallel contact as an example. Both contact members are made of the same single-walled CNTs. Using the typical value of linear resistivity of single-walled CNT $\rho_L = 20$ kΩ/μm [54][55], and diameter (or the width w) of 3 nm, an equivalent sheet resistance for both CNT contact members are estimated as $R_{sh1} = R_{sh2} = \rho_L w = 60\ \Omega/\square$, where the unit of the sheet resistance $\Omega/\square$ means "ohm per square" [12], [45]. The work function of CNTs is $W_1 = W_2 = 4.5$ eV [56]. The interfacial layer is assumed to be vacuum (relative permittivity ε_r = 1.0, and electron affinity $\chi = 0$). The voltage drop $V_g(x)$ across and the tunneling current density $J_c(x)$ through the contact interface are shown in Fig. 3.7 for various contact length L, vacuum gap distance D, and applied voltage V_0. The profiles of both $V_g(x)$ and $J_c(x)$ are symmetric about the center of the contact, as expected for similar contact members (similar to Figs. 3.2a and 3.2d above). As the contact length L increases, the local voltage drop $V_g(x)$ across the contact interface decreases, so does the tunneling current density $J_c(x)$, as shown in Figs. 3.7a and 3.7b. However, the total current in the contact structure, $I_{tot} = \int_0^L J_c(x)dx$ increases with L, since the total contact resistance of the tunneling junction decreases as the contact length increases (cf. Fig. 3.8a below). As shown in Figs. 3.7c and 3.7d, when the gap distance D increases, the voltage drop $V_g(x)$ increases, but the current density $J_c(x)$ decreases, which is because the tunneling junction becomes more resistive (See Chapter 2). Figures 3.7e and 3.7f shows both voltage drop $V_g(x)$ and current density $J_c(x)$ increase when the applied voltage V_o increases. More importantly, both $V_g(x)$ and $J_c(x)$ exhibit a stronger spatial dependence as V_0 increases. This strong voltage dependence of electrical properties of the tunneling junction is in sharp contrast with those of ohmic contacts, where the profiles of $V_g(x)$ and $J_c(x)$, and the total contact resistance is independent of the applied voltage, and the current density scales linearly with the voltage drops, as discussed in Sec. 3.3.1 and Sec. 3.3.2 above.

Also plotted in Fig. 3.7 are the analytical results from Eq. (3.7), by assuming constant tunneling contact resistivity across the contact length L (i.e. the typically assumed one-dimensional tunneling junction [24]), by (a), setting $V_g = V_0$ and using Eq. (3.10) (dashed lines) and (b), using ohmic approximations for the tunneling junction, in the limit of $V_g \rightarrow 0$ (dotted lines)[37], [38]. In the latter case, the tunneling current density is a linear function of V_g,

$$\bar{J_c}(\bar{x}) = B\bar{\varphi}_I e^{-A\Delta\bar{y}\sqrt{\bar{\varphi}_I}}\, \bar{V_g}(\bar{x}) \ \ , V_g \rightarrow 0 \tag{3.11}$$

where $= 315.60\sqrt{V_0 \frac{L^2[\mu m]R_{sh1}[\frac{\Omega}{\square}]}{D[\mathring{A}]\Delta y}}$. A and $\Delta\bar{y}$ are the same as for Eq (3.10). $\bar{\varphi}_I$ is calculated from the same expression for Eq (3.10) by setting $V_g = 0$. $\bar{y}_1 = \frac{1.2\ \bar{\lambda}}{\bar{\varphi}_2}$, $\bar{y}_2 = 1 - \frac{9.2\bar{\lambda}}{3\bar{\varphi}_2+4\bar{\lambda}-2\Delta\bar{\varphi}} + \bar{y}_1$ for forward bias; $\bar{y}_1 = \frac{9.2\bar{\lambda}}{3\bar{\varphi}_1+4\bar{\lambda}+\Delta\bar{\varphi}} - \frac{1.2\ \bar{\lambda}}{\bar{\varphi}_2}$, $\bar{y}_2 = 1 - \frac{1.2\ \bar{\lambda}}{\bar{\varphi}_2}$ for reverse bias; and $\bar{y}_1 = \frac{1.2\ \bar{\lambda}}{\bar{\varphi}_0}$, $\bar{y}_2 = 1 - \frac{1.2\ \bar{\lambda}}{\bar{\varphi}_0}$ for similar contacting members. $\bar{\lambda}$, $\Delta\bar{\varphi}$, $\bar{\varphi}_2$, $\bar{\varphi}_1$, $\bar{\varphi}_0$ have the same definition as in Eq. (3.10).

It is found that both assumptions of constant contact resistivity are not sufficiently reliable, especially when the tunneling thickness D decreases or the applied voltage V_o increases. As the tunneling junction resistance becomes nonlinear in these cases, it is necessary to use the coupled TLM equations, Eqs. (3.5) and (3.6), and the localized tunneling equation, Eq. (3.10), to provide more accurate predictions.

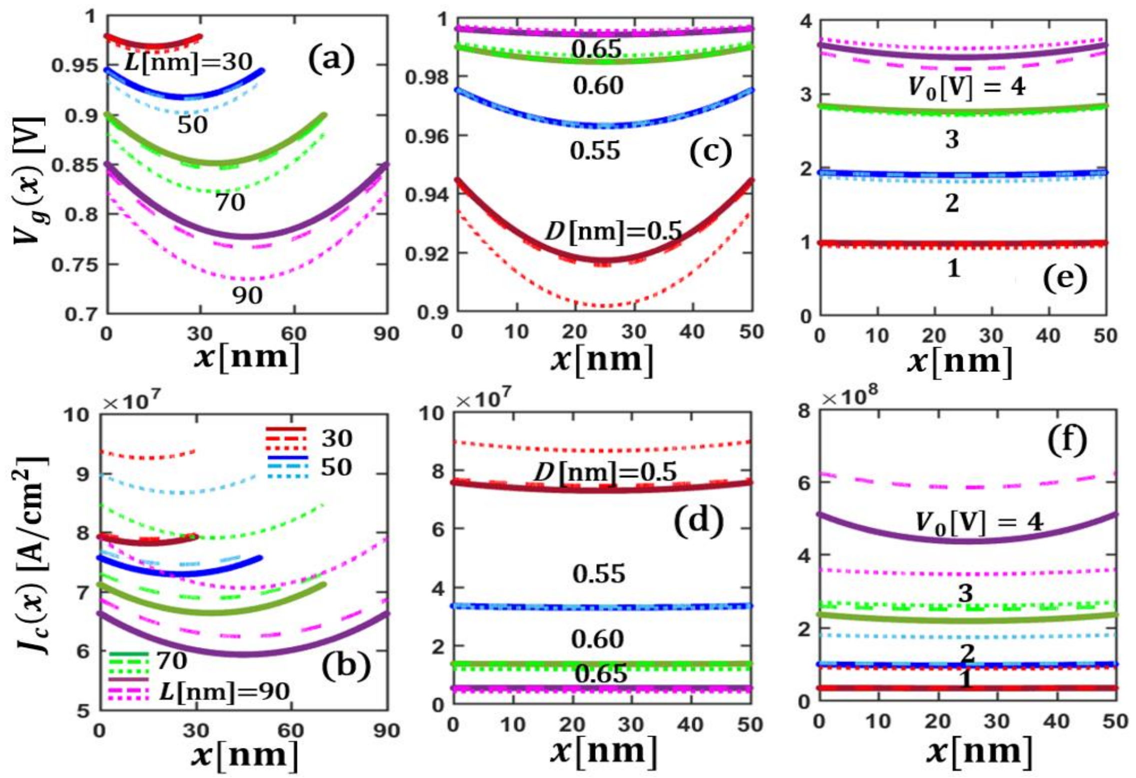

Figure 3.7 Similar material CNT-vacuum-CNT parallel tunneling contacts. (a) Voltage drop across the contact interface $V_g(x)$, and (b) tunneling current density across the contact interface $J_c(x)$ for different contact length L, with fixed $V_0 = 1$V, and D = 0.5 nm; (c) $V_g(x)$ and (d) $J_c(x)$ for different D, with fixed $V_0 = 1$V and L = 50 nm; (e) $V_g(x)$ and (f) $J_c(x)$ for different applied voltage V_0 with fixed $D = 0.55$ nm, and $L = 50$ nm. All the material properties are specified in the main text. Solid lines are for self-consistent numerical calculations using Eqs. 3.5, 3.6, and 3.10, dashed and dotted lines are for analytical calculations from Eq. 3.7 with ρ_c calculated using $V_g = V_0$ in Eq 3.10 and ohmic approximations for the tunneling junction, Eq. 3.11, in the limit of $V_g \to 0$, respectively. [1]

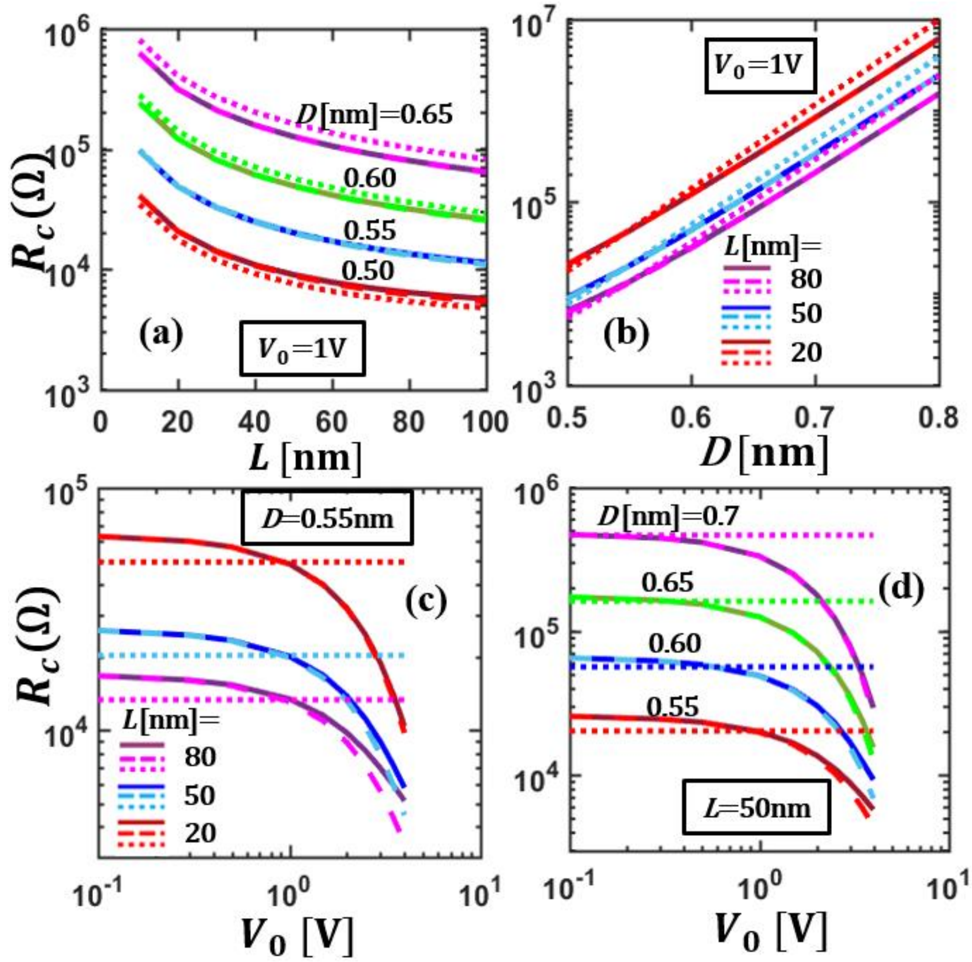

Figure 3.8 The total contact resistance R_c of the CNT-vacuum-CNT parallel contact. Contact resistance is plotted as a function of (a) contact length, L, for different insulating layer thickness, D, (b) D, for different L, for a fixed applied voltage, $V_0 = 1\text{V}$; (c) and (d) applied voltage V_0 for different L and D respectively, in CNT-vacuum-CNT contacts. Solid lines are for self-consistent numerical calculations using Eqs. 3.5, 3.6, and 3.10, dashed and dotted lines are for analytical calculations from Eq. 3.8 with ρ_c calculated using $V_g = V_0$ in Eq 3.10 and ohmic approximations for the tunneling junction, Eq. 3.11, in the limit of $V_g \to 0$, respectively. [1]

The total contact resistance R_c of the CNT-vacuum-CNT parallel contact is shown in Fig. 3.8, as functions of contact length L, vacuum gap distance D, and applied voltage V_0. The total contact resistance R_c increases very rapidly with increasing insulating layer thickness, D, and decreases with contact length, L. For the low applied voltage regime ($V_0 < 0.3$ V), R_c is almost independent of V_0, as shown in Figs. 3.8c and 3.8d. When the applied voltage $V_0 > 0.3$ V, R_c decreases sharply with V_0. This is because the junction is no longer ohmic and the tunneling resistivity ρ_c decreases nonlinearly with the junction voltage, as a function of position along the contact length. Ohmic approximations (Eqs. 3.8, 3.11) fail to give accurate results in the latter case and it is necessary to use the self-consistent numerical model. As L increases, the dependence of contact resistance on L becomes less significant. Similar profiles of contact resistance with L were observed in other experimental and theoretical works [12], [25], [32]. The contact resistance lies between 5 kΩ to 10 MΩ for the cases shown in Fig. 3.8, which agrees with previously reported experimental and theoretical works [24], [27], [30]. The existing 1D models give an inaccurate estimation of the contact resistance because they do not consider the variation of tunneling current density along the contact length.

Next, we extend our calculations for contacts of CNT with different metals – calcium (Ca), aluminum (Al), copper (Cu) and gold (Au). The work functions of Ca, Al, Cu and Au are taken as 2.9, 4.08, 4.7 and 5.1 eV respectively [57]. The work functions and dimensions of the CNT are kept same as before. In addition, the dimensions of the CNT and contacting-metal-2 are assumed to be same (width of 3 nm, thickness of 3 nm) for the simplicity of calculations. The resistivity of Ca, Al, Cu and Au are known to be $3.36 \times 10^{-8}\ \Omega m$, $2.7 \times 10^{-8}\ \Omega m$, $1.68 \times 10^{-8}\ \Omega m$ and $2.2 \times 10^{-8}\ \Omega m$ respectively [57], [58].

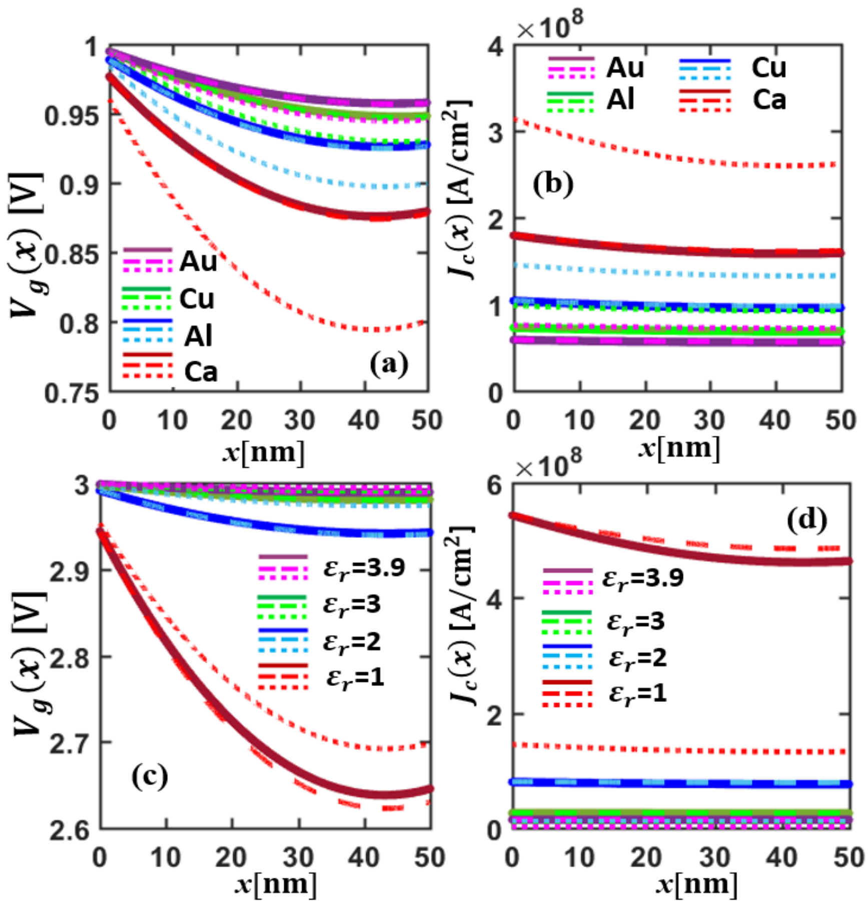

Figure 3.9 Dissimilar material CNT-insulator-metal parallel tunneling contacts. (a) Voltage drop across the interfacial insulating layer $V_g(x)$, and (b) tunneling current density $J_c(x)$, in CNT-insulator-Metal contacts, for fixed D = 0.5nm, L =50nm, V_0 = 1V and different contacting metals (Ca, Al, Cu, Au). (c) $V_g(x)$, and (d) $J_c(x)$, in CNT-insulator-Al contacts, for different insulating layer permittivity ε_r, with fixed D = 0.5nm, L =50nm, V_0 = 3V. Solid lines are for self-consistent numerical calculations using Eqs. 3.5, 3.6, and 3.10, dashed and dotted lines are for analytical calculations from Eq. 3.7 with ρ_c calculated using $V_g = V_0$ in Eq 3.10 and ohmic approximations for the tunneling junction, Eq. 3.11, in the limit of $V_g \to 0$, respectively. [1]

Figure 3.9 shows the effects of the work function of contacting member 2 (W_2) and the permittivity of the thin insulating layer (ε_r), on the current and voltage characteristics in CNT-insulator-metal contacts. As the two contact members are different, the voltage drop $V_g(x)$ and the tunneling current density $J_c(x)$ are no longer symmetric along the contact length L. Figure 3.9(a) and 3.9(b) show that the voltage drop increases and the tunneling current density decreases with increasing W_2. Figure 3.9(c) and 3.9(d) show that the voltage drop increases and the tunneling current density reduces significantly when the permittivity of the insulating layer increases from 1 to 3.9. Analytical solutions obtained by assuming constant tunneling resistivity along the contact length are also included, similar to the previous cases of Fig. 3.7. In general, for the chosen value of $D = 0.5$ nm, the ohmic approximations using Eq. 3.11 do not yield accurate results. The constant tunneling resistivity approximation using Eq. 3.10 by setting $V_g = V_0$ could be a good approximation for the self-consistent TLM model (Eqs. 3.5, 3.6, and 3.10), for tunneling layers with higher permittivity ε_r.

Figure 3.10 shows the contact resistance (in Ω) for various contact metals and tunneling films for CNT-insulator-metal contacts. Contact resistance increases with insulating layer thickness D, insulating layer permittivity ε_r and work function of contacting member W_2. It decreases with contact length L, as in the similar contacts in Fig. 3.8. The potential barrier in the insulating layer increases with the increase of work function of the contact metal, resulting in lower tunneling current and higher contact resistance.

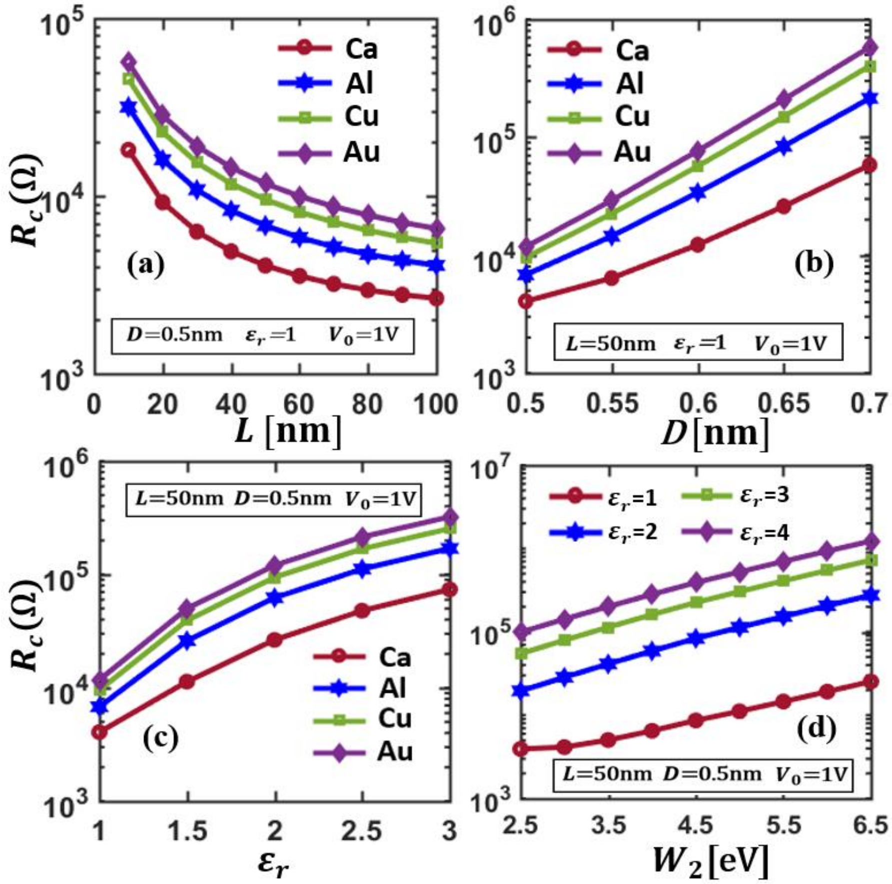

Figure 3.10 The total contact resistance R_c of the CNT-insulator-metal parallel contact. Contact resistance is plotted as a function of (a) contact length L, (b) insulator layer thickness D and (c) insulator layer permittivity ε_r, for CNT-insulator-metal contacts for different contacting metals (Ca, Al, Cu, Au). (d) Contact resistance as a function of work function of contacting member 2 (W_2). The material properties and dimensions for (a)-(c) are specified in the text (the same as in Fig. 3.9). For (d), the resistivity of contacting member 2 is assumed to be $2.0 \times 10^{-8}\ \Omega m$. The results are from the self-consistent numerical calculations using Eqs. 3.5, 3.6, and 3.10. [1]

3.4 Concluding Remarks

In this chapter, we proposed a self-consistent model to characterize partially overlapped parallel contacts. Our model considers the spatial variation of contact resistivity along the contact structure. We solved the TLM equations for three cases: 1) constant specific contact resistivity, 2) linearly varying specific contact resistivity, and 3) spatial dependent specific contact resistivity along the contact length due to current tunneling. Our study provides a thorough understanding of the contact tunneling resistance, current and voltage distributions across nano and sub-nano scale MIM junctions in parallel electrical contacts. The effects of contact geometry (i.e. dimension of the contact, and distance between the contact electrodes), and material properties (i.e. work function, sheet resistance of the contact members, and permittivity of the insulating layer) on the spatial distributions of currents and voltages across these contacts, and the overall contact resistance are studied in detail. While predominately classical in nature, the inclusion of tunneling current starts to address quantum effects in these small scale objects.

It is found that in general the ohmic approximation of tunneling junctions (Eq. 3.11) is not reliable for predicting the contact resistance of parallel tunneling contacts. The one-dimensional (1D) tunneling junction models (Eq. 3.10 with constant voltage across the whole junction) are good approximations of the parallel contacts only when the thickness D or the permittivity ε_r of the tunneling film is relatively large, or the applied voltage across the contact V_0 is relatively small. When the 1D models become unreliable for small D or ε_r, or large V_0, the self-consistent TLM equations coupled with the tunneling current (Eqs. 3.5, 3.6 and 3.10) need to be used to accurately characterize the parallel tunneling contacts.

The parallel tunneling contact in this work may be considered as the basic building block to better understand the macroscopic electrical conductivity of CNT fibers, which contains a very large number of such parallel contacts between individual CNTs. Furthermore, our study elucidates key parameters for parallel electrical contacts over a wide range of spatially dependent contact resistivity, which paves the way to strategically design of contact structures with controlled current distribution profiles and contact resistance, by spatially varying the contact layer properties and geometry.

In this formulation, we have ignored the effects of space charge and exchange-correlation inside the tunneling gap. We have also ignored possible charge trapping inside contact junctions. The model is assumed two-dimensional, where the effects of the transverse dimension are neglected. These issues will be the subjects of future studies. It is important to note that the transmission line model (TLM) is only a simplified approximation of the 2D electrical contacts, where the current crowding and the fringing fields near the contact corners cannot be fully accounted for. In order to accurately evaluate these effects as well as the impact of finite thickness in the contact members and the contact junction, field solution methods need to be used [12], [50], [51], [59].

REFERENCES

REFERENCES

[1] S. Banerjee, J. Luginsland, and P. Zhang, “A Two Dimensional Tunneling Resistance Transmission Line Model for Nanoscale Parallel Electrical Contacts,” *Sci Rep*, vol. 9, no. 14484, pp. 1–14, Oct. 2019, doi: 10.1038/s41598-019-50934-2.

[2] M. Rokni and Y. Levinson, “Joule heat in point contacts,” in *Proceedings International Workshop on Physics and Computer Modeling of Devices Based on Low-Dimensional Structures*, Nov. 1995, pp. 14–20, doi: 10.1109/PCMDLS.1995.494461.

[3] S. K. Thangaraju and K. M. Munisamy, “Electrical and Joule heating relationship investigation using Finite Element Method,” *IOP Conference Series: Materials Science and Engineering*, vol. 88, p. 012036, Sep. 2015, doi: 10.1088/1757-899X/88/1/012036.

[4] P. Zhang, S. B. Fairchild, T. C. Back, and Y. Luo, “Field emission from carbon nanotube fibers in varying anode-cathode gap with the consideration of contact resistance,” *AIP Advances*, vol. 7, no. 12, p. 125203, Dec. 2017, doi: 10.1063/1.5008995.

[5] E. Pop, “The role of electrical and thermal contact resistance for Joule breakdown of single-wall carbon nanotubes,” *Nanotechnology*, vol. 19, no. 29, p. 295202, 2008, doi: 10.1088/0957-4484/19/29/295202.

[6] F. Antoulinakis, D. Chernin, P. Zhang, and Y. Y. Lau, “Effects of temperature dependence of electrical and thermal conductivities on the Joule heating of a one dimensional conductor,” *Journal of Applied Physics*, vol. 120, no. 13, p. 135105, Oct. 2016, doi: 10.1063/1.4964112.

[7] P. Zhang *et al.*, “Temperature Comparison of Looped and Vertical Carbon Nanotube Fibers during Field Emission,” *Applied Sciences*, vol. 8, no. 7, p. 1175, Jul. 2018, doi: 10.3390/app8071175.

[8] E. H. Rhoderick, “Metal-semiconductor contacts,” *IEE Proceedings I - Solid-State and Electron Devices*, vol. 129, no. 1, pp. 1-, Feb. 1982, doi: 10.1049/ip-i-1.1982.0001.

[9] N. Braslau, J. B. Gunn, and J. L. Staples, “Metal-semiconductor contacts for GaAs bulk effect devices,” *Solid-State Electronics*, vol. 10, no. 5, pp. 381–383, May 1967, doi: 10.1016/0038-1101(67)90037-8.

[10] W. Mönch, “Metal-semiconductor contacts: electronic properties,” *Surface Science*, vol. 299–300, pp. 928–944, Jan. 1994, doi: 10.1016/0039-6028(94)90707-2.

[11] P. Zhang, “Scaling for quantum tunneling current in nano- and subnano-scale plasmonic junctions,” *Scientific Reports*, vol. 5, p. 9826, May 2015, doi: 10.1038/srep09826.

[12] P. Zhang and Y. Y. Lau, “An exact field solution of contact resistance and comparison with the transmission line model,” *Appl. Phys. Lett.*, vol. 104, no. 20, p. 204102, May 2014, doi: 10.1063/1.4878841.

[13] K. Choi *et al.*, “A Focused Asymmetric Metal–Insulator–Metal Tunneling Diode: Fabrication, DC Characteristics and RF Rectification Analysis,” *IEEE Transactions on Electron Devices*, vol. 58, no. 10, pp. 3519–3528, Oct. 2011, doi: 10.1109/TED.2011.2162414.

[14] S. Jung *et al.*, “Giant Electroresistance in Edge Metal-Insulator-Metal Tunnel Junctions Induced by Ferroelectric Fringe Fields,” *Scientific Reports*, vol. 6, p. 30646, Aug. 2016, doi: 10.1038/srep30646.

[15] B. K. Kaushik and M. K. Majumder, *Carbon Nanotube Based VLSI Interconnects: Analysis and Design*. Springer India, 2015.

[16] N. Behabtu *et al.*, “Strong, Light, Multifunctional Fibers of Carbon Nanotubes with Ultrahigh Conductivity,” *Science*, vol. 339, no. 6116, pp. 182–186, Jan. 2013, doi: 10.1126/science.1228061.

[17] Q. W. Li *et al.*, “Structure-Dependent Electrical Properties of Carbon Nanotube Fibers,” *Advanced Materials*, vol. 19, no. 20, pp. 3358–3363, 2007, doi: 10.1002/adma.200602966.

[18] A. Nieuwoudt and Y. Massoud, “On the Optimal Design, Performance, and Reliability of Future Carbon Nanotube-Based Interconnect Solutions,” *IEEE Transactions on Electron Devices*, vol. 55, no. 8, pp. 2097–2110, Aug. 2008, doi: 10.1109/TED.2008.926733.

[19] J. Tang *et al.*, “Flexible CMOS integrated circuits based on carbon nanotubes with sub-10 ns stage delays,” *Nature Electronics*, vol. 1, no. 3, pp. 191–196, Mar. 2018, doi: 10.1038/s41928-018-0038-8.

[20] L.-M. Peng, “A new stage for flexible nanotube devices,” *Nature Electronics*, vol. 1, no. 3, pp. 158–159, Mar. 2018, doi: 10.1038/s41928-018-0045-9.

[21] X. He *et al.*, “Wafer-scale monodomain films of spontaneously aligned single-walled carbon nanotubes.,” *Nat Nanotechnol*, vol. 11, no. 7, pp. 633–638, Jul. 2016, doi: 10.1038/nnano.2016.44.

[22] J. Zaumseil, “Single-walled carbon nanotube networks for flexible and printed electronics,” *Semicond. Sci. Technol.*, vol. 30, no. 7, p. 074001, 2015, doi: 10.1088/0268-1242/30/7/074001.

[23] S. Banerjee and P. Zhang, “A generalized self-consistent model for quantum tunneling current in dissimilar metal-insulator-metal junction,” *AIP Advances*, vol. 9, no. 8, p. 085302, Aug. 2019, doi: 10.1063/1.5116204.

[24] C. Li, E. T. Thostenson, and T.-W. Chou, “Dominant role of tunneling resistance in the electrical conductivity of carbon nanotube–based composites,” *Appl. Phys. Lett.*, vol. 91, no. 22, p. 223114, Nov. 2007, doi: 10.1063/1.2819690.

[25] A. Buldum and J. P. Lu, “Contact resistance between carbon nanotubes,” *Physical Review B*, vol. 63, no. 16, Apr. 2001, doi: 10.1103/PhysRevB.63.161403.

[26] B. E. Kilbride *et al.*, “Experimental observation of scaling laws for alternating current and direct current conductivity in polymer-carbon nanotube composite thin films,” *Journal of Applied Physics*, vol. 92, no. 7, pp. 4024–4030, Sep. 2002, doi: 10.1063/1.1506397.

[27] M. S. Fuhrer, A. K. L. Lim, L. Shih, U. Varadarajan, A. Zettl, and P. L. McEuen, “Transport through crossed nanotubes,” *Physica E: Low-dimensional Systems and Nanostructures*, vol. 6, no. 1–4, pp. 868–871, Feb. 2000, doi: 10.1016/S1386-9477(99)00228-3.

[28] W. Liu, C. Hierold, and M. Haluska, “Electrical contacts to individual SWCNTs: A review,” *Beilstein Journal of Nanotechnology*, vol. 5, no. 1, pp. 2202–2215, Nov. 2014, doi: 10.3762/bjnano.5.229.

[29] Y. Chai *et al.*, “Low-Resistance Electrical Contact to Carbon Nanotubes With Graphitic Interfacial Layer,” *IEEE Transactions on Electron Devices*, vol. 59, no. 1, pp. 12–19, Jan. 2012, doi: 10.1109/TED.2011.2170216.

[30] M. Foygel, R. D. Morris, D. Anez, S. French, and V. L. Sobolev, “Theoretical and computational studies of carbon nanotube composites and suspensions: Electrical and thermal conductivity,” *Physical Review B*, vol. 71, no. 10, Mar. 2005, doi: 10.1103/PhysRevB.71.104201.

[31] N. Chiodarelli *et al.*, “Measuring the electrical resistivity and contact resistance of vertical carbon nanotube bundles for application as interconnects,” *Nanotechnology*, vol. 22, no. 8, p. 085302, Feb. 2011, doi: 10.1088/0957-4484/22/8/085302.

[32] C. Lan, P. Srisungsitthisunti, P. B. Amama, T. S. Fisher, X. Xu, and R. G. Reifenberger, “Measurement of metal/carbon nanotube contact resistance by adjusting contact length using laser ablation,” *Nanotechnology*, vol. 19, no. 12, p. 125703, Mar. 2008, doi: 10.1088/0957-4484/19/12/125703.

[33] P. Wilhite, A. A. Vyas, and C. Y. Yang, “Metal-CNT contacts,” in *2014 12th IEEE International Conference on Solid-State and Integrated Circuit Technology (ICSICT)*, Oct. 2014, pp. 1–6, doi: 10.1109/ICSICT.2014.7021185.

[34] Q. Ngo *et al.*, “Electron Transport Through Metal-Multiwall Carbon Nanotube Interfaces,” *IEEE Transactions on Nanotechnology*, p. 311, 2004.

[35] B. G. Cook, W. R. French, and K. Varga, “Electron transport properties of carbon nanotube–graphene contacts,” *Appl. Phys. Lett.*, vol. 101, no. 15, p. 153501, Oct. 2012, doi: 10.1063/1.4756693.

[36] W. Shim, Y. Kwon, S.-Y. Jeon, and W.-R. Yu, "Optimally conductive networks in randomly dispersed CNT:graphene hybrids," *Scientific Reports*, vol. 5, p. 16568, Nov. 2015, doi: 10.1038/srep16568.

[37] J. G. Simmons, "Generalized Formula for the Electric Tunnel Effect between Similar Electrodes Separated by a Thin Insulating Film," *Journal of Applied Physics*, vol. 34, no. 6, pp. 1793–1803, Jun. 1963, doi: 10.1063/1.1702682.

[38] J. G. Simmons, "Electric Tunnel Effect between Dissimilar Electrodes Separated by a Thin Insulating Film," *Journal of Applied Physics*, vol. 34, no. 9, pp. 2581–2590, Sep. 1963, doi: 10.1063/1.1729774.

[39] J. G. Simmons, "Conduction in thin dielectric films," *Journal of Physics D: Applied Physics*, vol. 4, no. 5, pp. 613–657, May 1971, doi: 10.1088/0022-3727/4/5/202.

[40] I. E. Hashem, N. H. Rafat, and E. A. Soliman, "Theoretical Study of Metal-Insulator-Metal Tunneling Diode Figures of Merit," *IEEE Journal of Quantum Electronics*, vol. 49, no. 1, pp. 72–79, Jan. 2013, doi: 10.1109/JQE.2012.2228166.

[41] P. Zhang, Á. Valfells, L. K. Ang, J. W. Luginsland, and Y. Y. Lau, "100 years of the physics of diodes," *Applied Physics Reviews*, vol. 4, no. 1, p. 011304, Mar. 2017, doi: 10.1063/1.4978231.

[42] P. Zhang and Y. Y. Lau, "Ultrafast and nanoscale diodes," *Journal of Plasma Physics*, vol. 82, no. 5, Oct. 2016, doi: 10.1017/S002237781600091X.

[43] H. Murrmann and D. Widmann, "Current crowding on metal contacts to planar devices," *IEEE Transactions on Electron Devices*, vol. 16, no. 12, pp. 1022–1024, Dec. 1969, doi: 10.1109/T-ED.1969.16904.

[44] H. H. Berger, "Contact Resistance and Contact Resistivity," *J. Electrochem. Soc.*, vol. 119, no. 4, pp. 507–514, Apr. 1972, doi: 10.1149/1.2404240.

[45] D. K. Schroder, *Semiconductor Material and Device Characterization*. Wiley-Blackwell, 1998.

[46] "COMSOL Multiphysics® Modeling Software." https://www.comsol.com/.

[47] Y. S. Ang and L. K. Ang, "Current-Temperature Scaling for a Schottky Interface with Nonparabolic Energy Dispersion," *Phys. Rev. Applied*, vol. 6, no. 3, p. 034013, Sep. 2016, doi: 10.1103/PhysRevApplied.6.034013.

[48] Y. S. Ang, H. Y. Yang, and L. K. Ang, "Universal Scaling Laws in Schottky Heterostructures Based on Two-Dimensional Materials," *Phys. Rev. Lett.*, vol. 121, no. 5, p. 056802, Aug. 2018, doi: 10.1103/PhysRevLett.121.056802.

[49] S. Sun, L. K. Ang, D. Shiffler, and J. W. Luginsland, “Klein tunnelling model of low energy electron field emission from single-layer graphene sheet,” *Appl. Phys. Lett.*, vol. 99, no. 1, p. 013112, Jul. 2011, doi: 10.1063/1.3609781.

[50] P. Zhang, Y. Y. Lau, and R. M. Gilgenbach, “Analysis of current crowding in thin film contacts from exact field solution,” *J. Phys. D: Appl. Phys.*, vol. 48, no. 47, p. 475501, Oct. 2015, doi: 10.1088/0022-3727/48/47/475501.

[51] P. Zhang, D. M. H. Hung, and Y. Y. Lau, “Current flow in a 3-terminal thin film contact with dissimilar materials and general geometric aspect ratios,” *J. Phys. D: Appl. Phys.*, vol. 46, no. 6, p. 065502, Feb. 2013, doi: 10.1088/0022-3727/46/6/065502.

[52] A. Rose, “Space-Charge-Limited Currents in Solids,” *Phys. Rev.*, vol. 97, no. 6, pp. 1538–1544, Mar. 1955, doi: 10.1103/PhysRev.97.1538.

[53] R. I. Frank and J. G. Simmons, “Space-Charge Effects on Emission-Limited Current Flow in Insulators,” *Journal of Applied Physics*, vol. 38, pp. 832–840, Feb. 1967, doi: 10.1063/1.1709421.

[54] X. Ho and J. Wei, “Films of Carbon Nanomaterials for Transparent Conductors,” *Materials*, vol. 6, no. 6, pp. 2155–2181, May 2013, doi: 10.3390/ma6062155.

[55] X. Ho *et al.*, “Scaling Properties in Transistors That Use Aligned Arrays of Single-Walled Carbon Nanotubes,” *Nano Letters*, vol. 10, no. 2, pp. 499–503, Feb. 2010, doi: 10.1021/nl903281v.

[56] W. S. Su, T. C. Leung, and C. T. Chan, “Work function of single-walled and multiwalled carbon nanotubes: First-principles study,” *Phys. Rev. B*, vol. 76, no. 23, p. 235413, Dec. 2007, doi: 10.1103/PhysRevB.76.235413.

[57] D. R. Lide, G. Baysinger, S. Chemistry, L. I. Berger, R. N. Goldberg, and H. V. Kehiaian, *CRC Handbook of Chemistry and Physics*. 2003.

[58] C. Kittel, *Introduction to Solid State Physics*, Seventh Edition. 1996.

[59] P. Zhang, Y. Y. Lau, and R. M. Gilgenbach, “Minimization of thin film contact resistance,” *Appl. Phys. Lett.*, vol. 97, no. 20, p. 204103, Nov. 2010, doi: 10.1063/1.3517497.

CHAPTER 4

CIRCULAR TUNNELING ELECTRICAL CONTACTS

This chapter is based on the published journal paper "Contact resistance and current crowding in tunneling type circular nano-contacts," *J. Phys. D: Appl. Phys.*, vol. 53, no. 35, p. 355301, Jun. 2020, doi: 10.1088/1361-6463/ab8fe0, by **S. Banerjee,** P. Y. Wong and P. Zhang [1]. It is presented here with the permission of the copyright holder.

4.1 Introduction

In this chapter, we extend our previous work to demonstrate a 2D circular transmission line model (CTLM) for circular and annular nanocontacts. Circular tunneling contacts may be formed between two thin films or between a thin film substrate and a standing cylindrical nanorod (or nanofiber) as in the configuration of field emitters [2], [3]. Similar to Chapter 3 [4], this model is two-dimensional in the sense that we consider radial variation in the contact resistivity ρ_c, which may be introduced by a variety of factors. For instance, the inherent non-linearity of the current density-voltage ($J - V$) profiles of tunneling [5], [6] and Schottky junctions [7] may lead to strong radial dependence of the electrical properties in practical 2D contacts. Radial variation of the interfacial layer thickness for tunneling type contacts and nonuniform distribution of contaminants or impurities in the contact layer for ohmic or Schottky contacts can also cause radially changing ρ_c. Our model can be applied to characterize electrical properties in nanoscale thin film contacts, circular gate transistors (CGTs) [8], nanorod [9], nanowire [10], nano-fiber [2], and novel 2D material based devices [11].

The tunneling type of nanocontacts, where a thin (in nanometer or sub-nanometer range) interfacial layer (vacuum or insulator) exists between the two contact members [4], [12], [13], are ubiquitous. The local tunneling dependent ρ_c was calculated from the Simmons formula [14], [15] in Chapter 3 (Ref. [4]). Although the Simmons tunneling current formulas [14], [15] reveal basic scaling and parametric dependence of the $J - V$ profiles in metal-insulator-metal (MIM) nanogaps for low voltages, they ignore the effects of exchange correlation potential and the space charge potential inside the gap, which can modify the tunneling current density by several orders of magnitude as we have seen in Chapter 2 [5], [6]. Here we incorporate a more accurate quantum analysis based on the self-consistent Schrödinger-Poisson solutions [5], [6], into the 2D circular TLM to calculate the local voltage dependent tunneling resistivity along the radial contact length. We find that the contact resistance is voltage dependent, and for intermediate voltages when the tunneling junction is operated in the field emission regime [5], [6], the dependence is the strongest. We also find that the radial current distribution is highly nonhomogeneous. This non-homogeneity can be manipulated by engineering the contact layer properties and geometry radially.

In Sec. 4.2, the formulation of our 2D CTLM is presented. Results and discussions are presented in Sec. 4.3, where we consider two cases. Firstly, we assume constant specific contact resistivity along the radial contact length and obtain analytical expressions for the local voltage, currents, and total contact resistance. Secondly, we perform numerical calculations for nanocontacts with spatially dependent contact resistivity induced by local quantum tunneling phenomenon (Chapter 2) [5], [6]. Summary and suggestions for future research are given in Section 4.4. Although we focus on tunneling type electrical contacts here, the proposed 2D CTLM is general and can be used for other types of circular and annular electrical contacts, such as nanoscale ohmic contacts and Schottky contacts based on 2D materials heterostructure [16]–[18].

4.2 The 2D-Circular Transmission Line Model

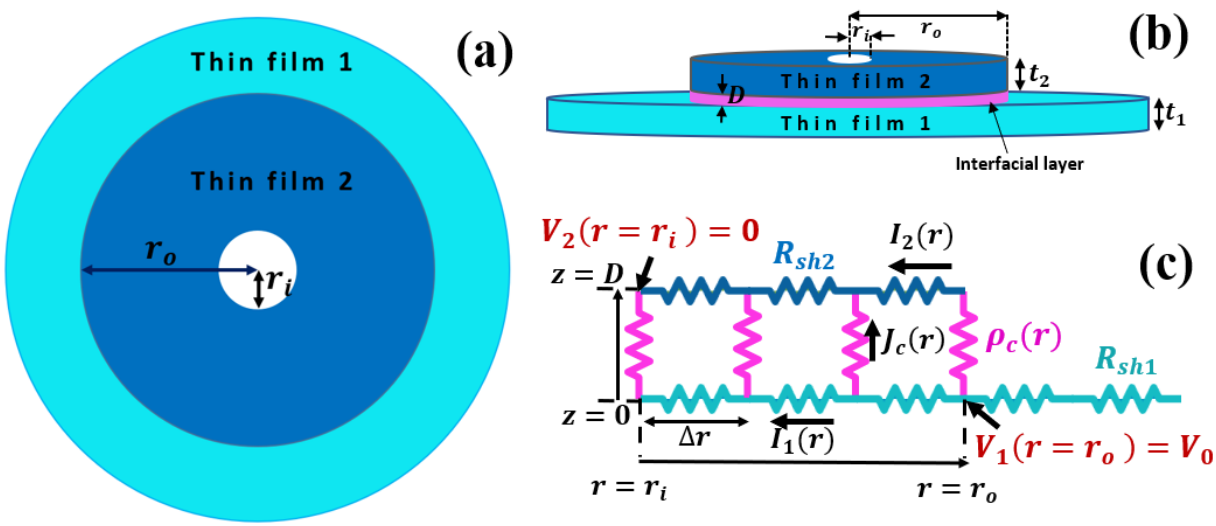

Figure 4.1 Electrical contact between two circular thin films: (a) top view; (b) side view; (c) its transmission line model. In (a), (b) and (c) a thin resistive interface layer (or a tunneling layer of permittivity ϵ_r) of thickness D is sandwiched between the two contacting members. The thicknesses of thin film 1 and 2 are t_1 and t_2, respectively. [1]

Consider a circular (ring) contact formed between two conducting thin films or layers, as shown in Figs. 4.1(a) and 4.1(b). The outer radius of thin film 2 is r_o and the inner radius of both the films is r_i. A thin resistive interface layer of thickness D is sandwiched between them. Following Reeves [19]–[21], we modified the basic Cartesian geometry lumped circuit transmission line model (TLM) [22]–[25] for circular structures, as shown in Fig. 4.1(c). The sheet resistance of the two conductors is R_{sh1} and R_{sh2}, respectively. The radially dependent specific interfacial resistivity (also termed specific contact resistivity) is $\rho_c(r)$, which is either predefined or calculated from the local tunneling current in the case of an insulating tunneling layer [14], [15], [26].

In the contact region in Fig. 4.1(c), when $\Delta r \to 0$, Kirchhoff's laws for current and voltage give the following equations,

$$\frac{dI_1(r)}{dr} = 2\pi r\, J_c(r), \tag{4.1a}$$

$$\frac{dV_1(r)}{dr} = \frac{I_1(r)R_{sh1}}{2\pi r}, \tag{4.1b}$$

$$\frac{dI_2(r)}{dr} = -\,2\pi r\, J_c(r), \tag{4.1c}$$

$$\frac{dV_2(r)}{dr} = \frac{I_2(r)R_{sh2}}{2\pi r}, \tag{4.1d}$$

where $I_1(r)$ and $I_2(r)$ represent the currents flowing at r along the radial direction of thin films 1 and 2, respectively, and $V_1(r)$ and $V_2(r)$ are the local voltages at r along the radial direction of thin films 1 and 2, respectively. $J_c(r) = V_g(r)/\rho_c(r)$ and $V_g(r) = V_1(r) - V_2(r)$ are the local current density and the local voltage drop across the contact interface at r, respectively.

From Eqs. 4.1(a) and 4.1(c), $I_1(r) + I_2(r) = I_{tot} = \text{constant}$, where I_{tot} is the total current in the circuit to be determined from the following boundary conditions for Eq. (4.1),

$$V_1(r = r_o) = V_o,\, I_1(r = r_i) = 0,\; I_2(r = r_o) = 0,\, V_2(r = r_i) = 0, \tag{4.2}$$

where we assume the voltage of the upper contact member at $r = r_i$ is 0 and the external voltage V_0 is applied at $r = r_o$ to the lower contact member. Note that $I_1(r = r_o) = I_{tot}$, $I_2(r = r_i) = I_{tot}$, and $I_{tot} = \int_{r_i}^{r_o} 2\pi r\, J_c(r)\, dr$. From Eqs. (4.1) and (4.2), we get $V_1'(r = r_o) = I_{tot}R_{sh1}/2\pi r_o$, $V_1'(r = r_i) = 0$, $V_2'(r = r_o) = 0$, $V_2'(r = r_i) = I_{tot}R_{sh2}/2\pi r_i$, where a prime denotes a derivative with respect to r. For the contact model in Fig. 4.1(c), the contact resistance is defined as,

$$R_c = \frac{V_1(r_o) - V_2(r_i)}{I_{tot}} = \frac{V_o}{I_{tot}}\,. \tag{4.3}$$

For convenience, we introduce non-dimensional quantities, $\bar{r} = r/r_o$, $\beta = r_i/r_o$, $\bar{\rho}_c(\bar{r}) = \rho_c(r)/R_{sh1}r_o^2$, $\overline{R_{sh2}} = R_{sh2}/R_{sh1}$, $\overline{J_c}(\bar{r}) = J_c(r)R_{sh1}r_o^2/V_o$, $\overline{V_1}(\bar{r}) = V_1(r)/V_o$, $\overline{V_2}(\bar{r}) = V_2(r)/V_o$, $\overline{V_g}(\bar{r}) = V_g(r)/V_o$, $\overline{R_c} = R_c 2\pi/R_{sh1}$, and $\alpha = I_{tot}/I$, where $I = 2\pi V_o/R_{sh1}$. In normalized forms, Eq. (4.1) can be written into the following coupled second order differential equations,

$$\frac{d^2\overline{V_1}(\bar{r})}{d\bar{r}^2} + \frac{1}{\bar{r}}\frac{d\overline{V_1}(\bar{r})}{d\bar{r}} - \frac{\overline{V_1}(\bar{r}) - \overline{V_2}(\bar{r})}{\overline{\rho_c}(\bar{r})} = 0, \tag{4.4a}$$

$$\frac{d^2\overline{V_2}(\bar{r})}{d\bar{r}^2} + \frac{1}{\bar{r}}\frac{d\overline{V_2}(\bar{r})}{d\bar{r}} + \overline{R_{sh2}}\frac{\overline{V_1}(\bar{r}) - \overline{V_2}(\bar{r})}{\overline{\rho_c}(\bar{r})} = 0. \tag{4.4b}$$

Note that $\overline{V_g}(\bar{r}) = \overline{V_1}(\bar{r}) - \overline{V_2}(\bar{r})$ and $\overline{J_c}(\bar{r}) = \overline{V_g}(\bar{r})/\overline{\rho_c}(\bar{r})$. The corresponding boundary conditions to Eqs. (4.4) are,

$$\overline{V_1}(\bar{r} = 1) = 1\ , \overline{V_1}'(\bar{r} = 1) = \alpha, \overline{V_1}'(\bar{r} = \beta) = 0, \tag{4.5a}$$

$$\overline{V_2}(\bar{r} = \beta) = 0, \overline{V_2}'(\bar{r} = 1) = 0, \overline{V_2}'(\bar{r} = \beta) = \frac{\alpha\overline{R_{sh2}}}{\beta}, \tag{4.5b}$$

and the normalized total current,

$$\alpha = I_{tot}/I = \int_{\beta}^{1} \bar{r}\,\overline{J_c}(\bar{r})d\bar{r}. \tag{4.5c}$$

Equations (4.4) and (4.5) are solved to give the voltage distribution along and across the contact interface as well as the total contact resistance, for a given electrical contact (Fig. 4.1) with radially dependent interface specific contact resistivity $\overline{\rho_c}(\bar{r})$, following a similar procedure as described in Chapter 3. Equations (4.4) and (4.5) can be solved numerically for arbitrary radial dependence of specific contact resistivity $\overline{\rho_c}(\bar{r})$. Here, we focus on two special cases of practical importance. We first consider the case of constant $\overline{\rho_c}$, where analytical solutions can be obtained (Sec. 4.3.1). This serves to validate our numerical approach. We then consider the effects of radially dependent $\overline{\rho_c}(\bar{r})$ on the tunneling type electrical contacts (4.3.2). The one-dimensional MIM quantum tunneling equations developed in Chapter 2 [5] are coupled with Eqs. (4.4), (4.5) and are solved self-consistently.

4.3 Results and Discussion

4.3.1 Constant specific contact resistivity along the contact length

For the special case of constant specific contact resistivity ρ_c, Eq. (4.4) can be rewritten as,

$$\frac{d^2\overline{V_g}(\bar{r})}{d\bar{r}^2} + \frac{1}{\bar{r}}\frac{d\overline{V_g}(\bar{r})}{d\bar{r}} - (1+\overline{R_{sh2}})\frac{\overline{V_g}(\bar{r})}{\overline{\rho_c}} = 0. \tag{4.6}$$

The corresponding boundary conditions from Eqs. 4.5(a) and 4.5(b) are,

$$\overline{V_g}'(\bar{r}=1) = \alpha, \overline{V_g}'(\bar{r}=\beta) = -\frac{\alpha\overline{R_{sh2}}}{\beta}. \tag{4.7}$$

Using Eq. (4.7), the solution to Eq. (4.6) is,

$$\overline{V_g}(\bar{r}) = aI_0(\lambda\bar{r}) + bK_0(\lambda\bar{r})\ , \quad \bar{r} > 0 \tag{4.8}$$

where I_0 and K_0 are the zeroth order modified Bessel functions of the first and second kind respectively and $\lambda = \sqrt{(1+\overline{R_{sh2}})/\overline{\rho_c}}$. The constants a and b are calculated from the boundary conditions as, $a = C/(CX+DY)$, $b = D/(CX+DY)$. The expressions of X, Y, C, and D are,

$$X = I_0(\lambda\beta) - \frac{I_0(\lambda\beta)-I_0(\lambda)}{\overline{\rho_c}\lambda^2} + \frac{\beta I_1(\lambda\beta)\ln\beta}{\overline{\rho_c}\lambda},$$

$$Y = K_0(\lambda\beta) - \frac{K_0(\lambda\beta)-K_0(\lambda)}{\overline{\rho_c}\lambda^2} - \frac{\beta K_1(\lambda\beta)\ln\beta}{\overline{\rho_c}\lambda},$$

$$C = \frac{\overline{R_{sh2}}K_1(\lambda)+\beta K_1(\lambda\beta)}{\lambda\beta\left(K_1(\lambda\beta)I_1(\lambda)-K_1(\lambda)I_1(\lambda\beta)\right)}, \text{ and}$$

$$D = \frac{\overline{R_{sh2}} I_1(\lambda) + \beta I_1(\lambda\beta)}{\lambda\beta\big(K_1(\lambda\beta) I_1(\lambda) - K_1(\lambda) I_1(\lambda\beta)\big)},$$

where I_1 and K_1 are the first order modified Bessel functions of the first and second kind respectively.

The normalized contact resistance is,

$$\overline{R_c} = \frac{\overline{V_1}(1) - \overline{V_2}(\beta)}{\alpha} = 1/\alpha = (CX + DY). \tag{4.9}$$

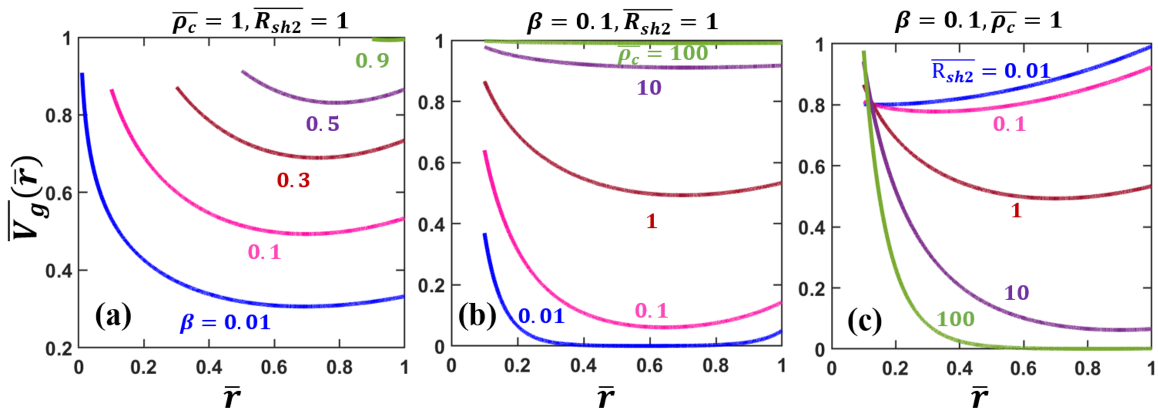

Figure 4.2 Normalized voltage drop across the contact interface $\overline{V_g}(\bar{r})$, along the radial direction of an annular contact with uniform contact resistivity, for different values of (a) inner radius to outer radius ratio β, with $\overline{\rho_c} = 1$ and $\overline{R_{sh2}} = R_{sh2}/R_{sh1} = 1$, (b) specific contact resistivity $\overline{\rho_c}$, with $\beta = 0.1$ and $\overline{R_{sh2}} = 1$, (c) sheet resistance ratio $\overline{R_{sh2}}$, with $\beta = 0.1$ and $\overline{\rho_c} = 1$. All the quantities are in their normalized forms defined in Sec. 4.2.

Figure 4.2 shows the profiles of voltage drop $\overline{V_g}(\bar{r})$ along the radial contact length $\bar{r}$ for a parallel annular thin film contact (Fig. 4.1) for different inner to outer radius ratio β (Fig. 4.2(a)), specific contact resistivity $\overline{\rho_c}$ (Fig. 4.2(b)), and sheet resistance ratio $\overline{R_{sh2}}$ (Fig. 4.2(c)). Note that, since $\overline{\rho_c}$ is constant along $\bar{r}$ here, the profiles of contact current density $\overline{J_c}(\bar{r}) = \overline{V_g}(\bar{r})/\overline{\rho_c}$ follow those of $\overline{V_g}(\bar{r})$. The voltage drop across the contact interface increases with increasing inner radius to outer radius ratio β and specific contact resistivity ρ_c. For similar contacting members ($\overline{R_{sh2}} = R_{sh2}/R_{sh1} = 1$) the maximum voltage drop occurs at the inner edge ($r = r_i$) of the annular contact (c.f. Figs. 4.2a and b). This is because the modified Bessel function of the second kind (K_0 term in Eq. (4.8)) increases sharply near the center. Physically this means the current in the contact interface is mostly crowded near $r = r_i$. The current spreads out as it flows away from the center through the least resistive path. Figure 4.2(c) shows a similar trend in $\overline{V_g}(\bar{r})$ for dissimilar contacting members with $\overline{R_{sh2}} > 1$. In fact, the current crowding at the inner edge ($r = r_i$) increases with increasing $\overline{R_{sh2}}$. The voltage drop (and the contact current density) at the outer edge ($r = r_o$) increases with decreasing $\overline{R_{sh2}}$. For $\overline{R_{sh2}} \leq 0.1$, the majority of the contact current flows near $r = r_o$. It is interesting to note from Fig. 4.2(a) that the voltage drop profiles are highly asymmetric at the two edges ($r = r_i$, $r = r_o$) of the annular contact under study (Fig. 4.1) when β is small, and the asymmetry reduces as β increases. For the limiting case of $\beta \to 1$ (i.e. $r_i \approx r_o$), CTLM reduces to the planar limit (Chapter 3) [4], where the maximum voltage drop occurs at both the edges ($V_g(r = r_i) \approx V_g(r = r_o)$) and the minimum occurs at $(r_i + r_o)/2$, making the profiles symmetric.

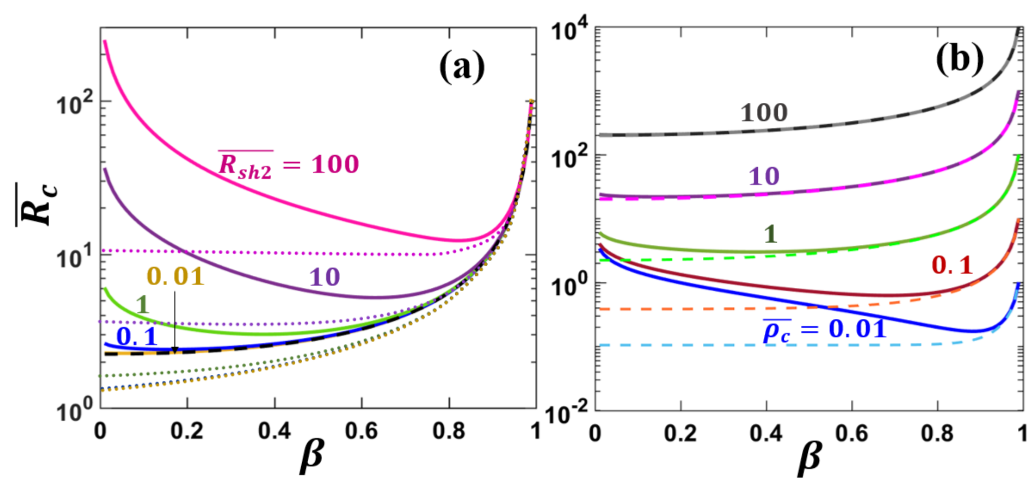

Figure 4.3 Normalized contact resistance $\overline{R_c}$ of the annular contact (Fig. 4.1) as a function of inner radius to outer radius ratio β for different (a) normalized sheet resistance of contacting member 2, $\overline{R_{sh2}}$, and (b) normalized specific contact resistivity $\overline{\rho_c}$. The dotted lines in (a) are calculated from Eq. (3.8) of Chapter 3, that is, for Cartesian parallel electrical contacts. Dashed lines are for Eq. (4.10), the limiting case of $\overline{R_{sh2}} \to 0$.

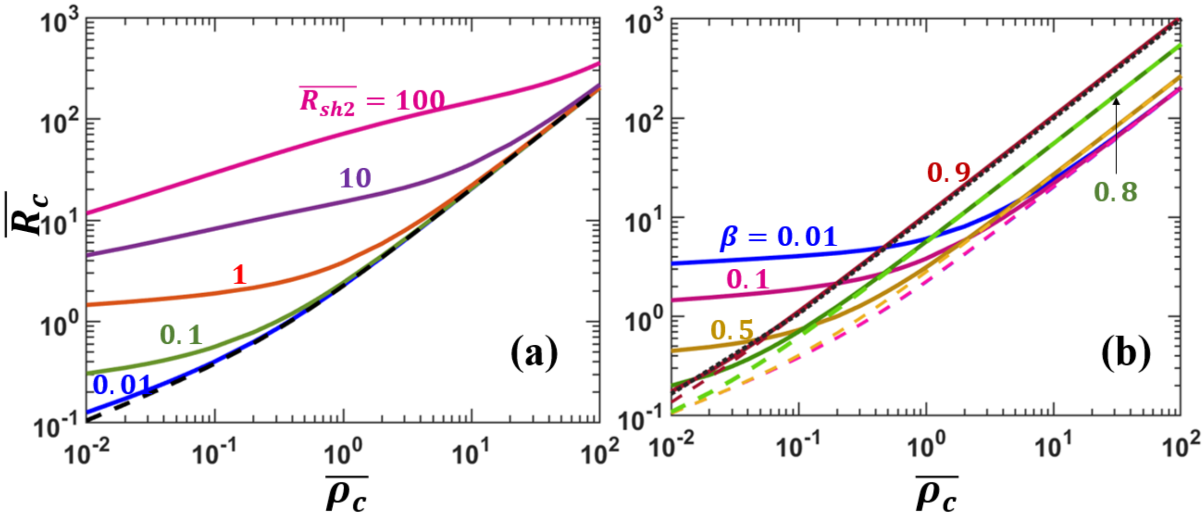

Figure 4.4 Normalized contact resistance $\overline{R_c}$ of the annular contact (Fig. 4.1) as a function of normalized specific contact resistivity $\overline{\rho_c}$ for different (a) normalized sheet resistance of contacting member 2, $\overline{R_{sh2}}$, and (b) inner radius to outer radius ratio β. In (a), β = 0.1, and in (b), $\overline{R_{sh2}}$=1. Dashed lines are for Eq. (4.10), the limiting case of $\overline{R_{sh2}} \rightarrow 0$. The black dotted line in (b) The dotted lines in (a) are calculated from Eq. (3.8) of Chapter 3, that is, for Cartesian parallel electrical contacts.

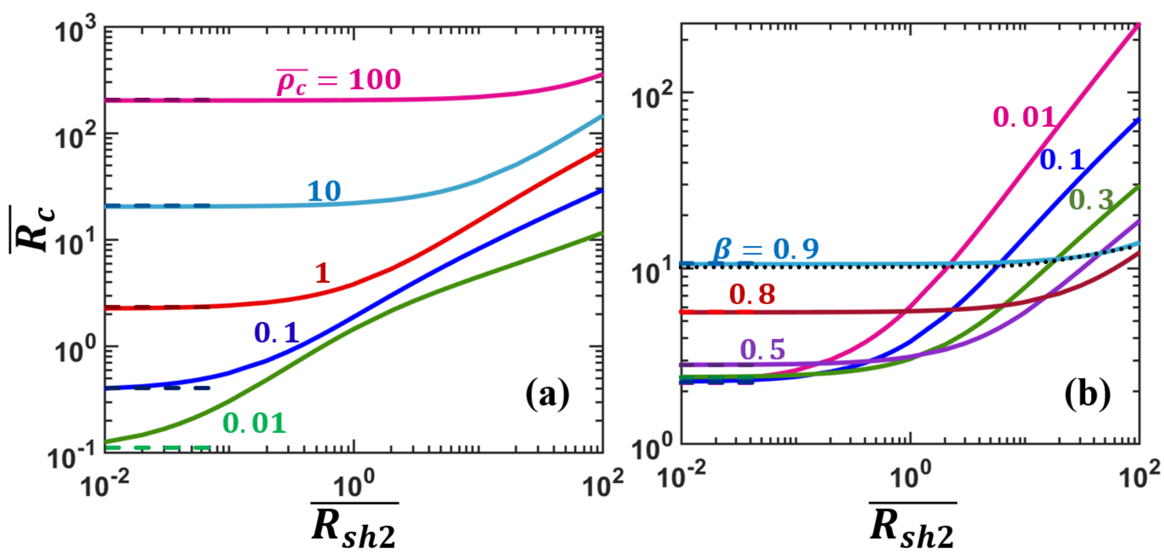

Figure 4.5 Normalized contact resistance $\overline{R_c}$ of the annular contact (Fig. 4.1) as a function of sheet resistance ratio $\overline{R_{sh2}}$ for different (a) normalized specific contact resistivity $\overline{\rho}_c$ and (b) inner radius to outer radius ratio β. In (a), β = 0.1, and in (b), $\overline{\rho_c}$ = 1. Dashed lines are for Eq. (4.10), the limiting case of $\overline{R_{sh2}} \rightarrow 0$. The black dotted line in (b) is calculated from Eq. (3.8) of Chapter 3, that is, for Cartesian parallel electrical contacts.

The normalized contact resistance $\overline{R_c}$ is calculated from Eq. (4.9) and plotted in Figs. 4.3, 4.4, and 4.5 as functions of inner radius to outer radius ratio β, normalized specific contact resistivity $\overline{\rho_c}$, and sheet resistance ratio of the two contacting members $\overline{R_{sh2}}$, respectively. Figures 4.3(a) and (b) show that for $\beta < 0.8$, $\overline{R_c}$ decreases with β when $\overline{R_{sh2}}$ is high or $\overline{\rho_c}$ is low. Figures 4.4(b) and 4.5(b) also confirm this behavior. However, when β is increased above 0.8, R_c increases drastically with β. Larger β means shorter radial contact length $r_o - r_i$ (for a fixed r_i or r_o), resulting in higher total contact resistance for the annular contact structure. In general, $\overline{R_c}$ increases with the specific contact resistivity ρ_c or the sheet resistance ratio $\overline{R_{sh2}}$. Profiles of total contact resistance for the case of $\overline{R_{sh2}} = 0$ are also plotted in Figs. 4.3, 4.4 and 4.5 as dashed lines. When $\overline{R_{sh2}} \rightarrow 0$, Eq. (4.9) becomes,

$$\overline{R_c} = \frac{K_1(\lambda\beta)I_0(\lambda)+I_1(\lambda\beta)K_0(\lambda)}{\lambda\left(K_1(\lambda\beta)I_1(\lambda)-K_1(\lambda)I_1(\lambda\beta)\right)}, \tag{4.10}$$

with $\lambda = \sqrt{1/\overline{\rho_c}}$. Note that Eq. (4.10) is identical to the expression typically used for metal-semiconductor contact [24], [25]. The difference between solid lines (Eq. 4.9) and dashed lines (Eq. 4.10) decreases when $\overline{\rho_c}$ or β is large, as shown in Figs. 4.3(b) and 4.4(b).

The dotted lines in Figs. 4.3(a), 4.4(b), and 4.5(b) are calculated from the contact resistance for parallel Cartesian contacts, that is, Eq. (3.8) of Chapter 3 [4]. Note that the spatial dimensions were normalized by the contact length L (= $r_o - r_i$ in circular case) in Sec. 3.2 [4], whereas they are normalized by the outer radius r_o for the circular case here. To make the normalization consistent for direct comparison, we multiply the normalized specific contact resistivity by $1/(1-\beta)^2$ before inserting into Eq. (3.8), which is multiplied by $(1-\beta)$ to obtain the dotted lines in Figs. 4.3(a), 4.4(b), and 4.5(b). For $\beta > 0.9$, the profiles of annular and Cartesian contact resistance match exceptionally well, as CTLM approaches the limit of Cartesian TLM.

4.3.2 Tunneling dependent contact resistivity

Next, we consider the case where the parallel annular contacts are formed through a tunneling interface layer between the two annular contact members. In this case, due to the nonlinear current density-voltage ($J-$V) characteristic of metal-insulator-metal (MIM) tunnel junctions, specific contact resistivity ρ_c varies radially. For simplicity, we have made the following assumptions: 1) the thickness of the interfacial insulating film in the contact area is uniform and 2) the insulating film is sufficiently thin (in the nano- or subnano-meter scale) so that charge trappings are ignored (Chapter 2, Sec. 2.2).

The local contact current density $J_c(r)$ at any location r from contact member 1 to contact member 2 is calculated based on the self-consistent 1D Schrödinger-Poisson solutions in the MIM junction developed in Chapter 2, Sec. 2.2 [5]. For given values of the work function of the two contact members $W_{1,2}$, electron affinity X, thickness D, and relative permittivity ϵ_r of the insulator layer, the local contact current density $J_c(r)$ can be calculated from this 1D quantum model for an input of the contact voltage drop $V_g(r)$ at any location r [5], [6]. The calculation of this $J_c(r)$-$V_g(r)$ relation is coupled with CTLM, Eqs. (4.4), (4.5), and solved self-consistently.

We keep the normalization consistent. Since solving the coupled quantum tunneling model and CTLM is time expensive, we calculate the one dimensional tunneling current density separately for the given MIM parameters (W_1, W_2, D, ϵ_r, X), over a wide range of bias voltages. The obtained $J-V$ curves are normalized (as in Sec. 4.2) and then fitted with polynomials. Those curve-fitted equations are used to find the specific contact resistivity $\bar{\rho}_c(\bar{r}) = \overline{V_g}(\bar{r})/\overline{J_c}(\bar{r}) = (\overline{V_1}(\bar{r}) - \overline{V_2}(\bar{r}))/\overline{J_c}(\bar{r})$, which is then inserted into the CTLM equations, Eqs. (4.4) and (4.5), to give a self-consistent solution to the voltage and current profiles, as well as the contact resistance for the circular (annular) tunneling contact.

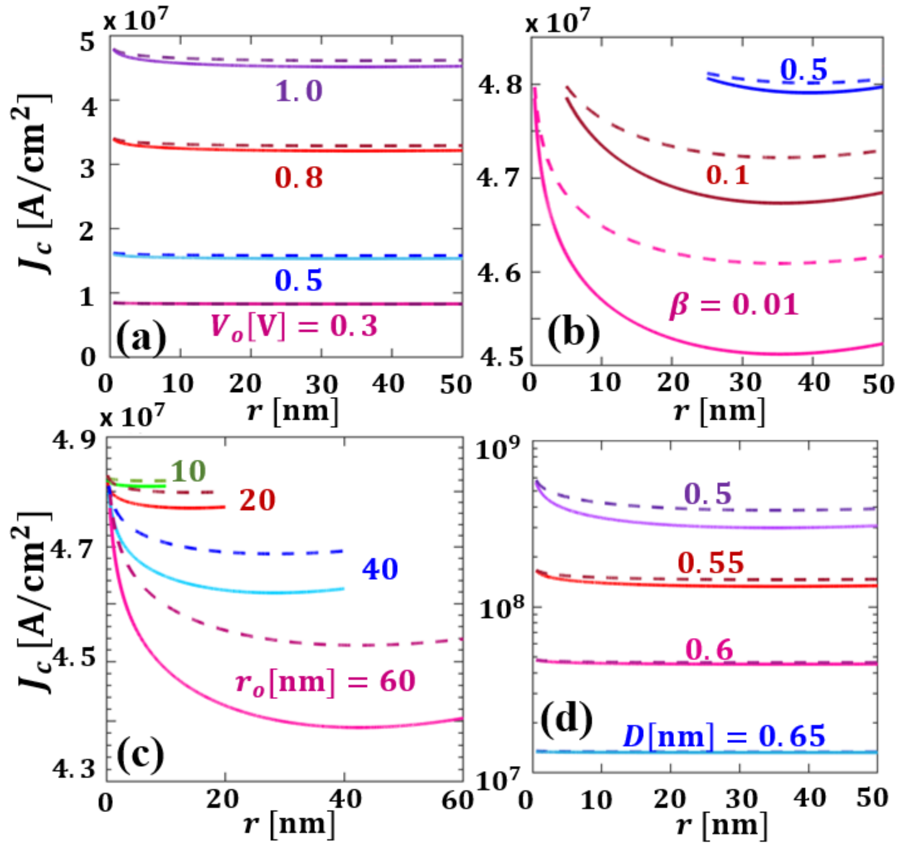

Figure 4.6 Tunneling current density across the contact interface $J_c(r)$ for different (a) input voltage V_0, with fixed $r_0 = 50$ nm, $\beta = 0.01$, and $D = 0.6$ nm; (b) inner radius to outer radius ratio β, with fixed $r_0 = 50$ nm, $V_0 = 1$ V, and $D = 0.6$ nm; (c) outer radius r_0, with fixed $V_0 = 1$ V, $\beta = 0.01$, and $D = 0.6$ nm; (d) interfacial layer thickness D, with fixed $r_0 = 50$ nm, $\beta = 0.01$, and $V_0 = 1$ V. All the material properties are specified in the main text. Solid lines are for self-consistent numerical calculations using Eqs. (4.4), (4.5), and MIM quantum tunneling formulations (Chapter 2, Sec. 2.2) [5]. Dashed lines are for analytical calculations from Eq. (4.8) with ρ_c being constant, calculated using $V_g = V_0$ in the MIM quantum model.

As an example, we consider Cu-vacuum-Cu circular thin film contacts. For our calculations, sub-nanometer scale interfacial layer thicknesses are assumed for the tunneling type of electrical contacts [12], [27], [28]. The dimensions of the contacting members are assumed to be in nanoscale. We considered a wide range of electrode diameter, 10 – 160 nm, as electrodes of this range are common in transistors [29], [30], nanowire, nanofiber, and nanorod based novel devices [31]–[33]. Sheet resistance of both the contact members is estimated as $R_{sh1} = R_{sh2} = 18\ \Omega/\square$ [34], where the unit of the sheet resistance $\Omega/\square$ means "ohm per square". The work function of Cu thin films is $W_1 = W_2 = 4.56$ eV [34]. The interfacial layer is assumed to be vacuum (relative permittivity ϵ_r = 1.0 and electron affinity $X = 0$ eV). The tunneling current density $J_c(r)$ through the contact interface is shown in Fig. 4.6 for various input voltages V_0 (Fig. 4.6(a)), inner radius to outer radius ratios β (Fig. 4.6(b)), outer radii r_0 (Fig. 4.6(c)), and interfacial layer thicknesses D (Fig. 4.6(d)). The profiles of $J_c(r)$ are asymmetric and current crowding occurs mainly at the inner edge, as expected for similar contact members (similar to Fig. 4.2 above). As shown in Fig. 4.6(a), because of the strong nonlinearity in the $J - V$ characteristics of a tunneling junction, $J_c(r)$ increases and exhibits a stronger radial dependence when the applied voltage V_o increases. This strong voltage dependence of electrical properties of the tunneling junction is in sharp contrast with those of ohmic contacts (Sec. 4.3.1), where the profiles of $J_c(r)$ and the total contact resistance is independent of the applied voltage and the current density scales linearly with the voltage drop. Figure 4.6(b) shows that, as β decreases, that is, the contact length $r_o - r_i$ increases, the tunneling current density $J_c(r)$ decreases. The influence of outer radius r_o for a fixed β is shown in Fig. 4.6(c). The tunneling current density $J_c(r)$ decreases when r_o increases. However, the total current in the contact structure, $I_{tot} = \int_{r_i}^{r_o} 2\pi r\, J_c(r) dr$, increases with r_o because the total contact resistance of the tunneling junction decreases with r_o (c.f. Fig. 4.7(a) below). In Figure 4.6(d), when the gap distance D increases, the current density $J_c(r)$ decreases quickly because the tunneling junction becomes more resistive [5], [6].

Dashed lines in Fig. 4.6 are the analytical results calculated from Eq. (4.8) assuming constant tunneling contact resistivity ρ_c across the radial contact length, which is the typically assumed one-dimensional tunneling contact. This ρ_c is calculated from the $J - V$ curve of the metal-insulator-metal tunneling junction by setting $V_g(r) = V_o$ everywhere along the contact length. The constant contact resistivity assumptions are inadequate, especially when the tunneling thickness D or inner radius to outer radius ratio β decreases, or the applied voltage V_o or outer radius r_o increases. For these cases, one should solve the coupled TLM equations, Eqs. (4.4) and (4.5), and the localized MIM tunneling equation (Sec. 2.2) self-consistently to give more reliable predictions.

The total contact resistance R_c of the Cu-vacuum-Cu circular thin film contact is shown in Fig. 4.7 as functions of applied voltage V_0 and inner to outer radius ratio β. The total contact resistance R_c decreases with r_o, as shown in Fig. 4.7(a). As r_o increases, the dependence of contact resistance on r_o becomes less significant. The dashed lines are for analytical solutions of the 1D tunneling model with constant ρ_c calculated from Eqs. (4.8) and (4.9) as previously stated. The difference between the 1D model (Eq. (4.9)) and self-consistent numerical calculations (Eqs. (4.4), (4.5)) is significant when D or β is small, or when r_o or V_0 is large. In these regimes where the 1D tunneling model with constant ρ_c approximations fail to provide reliable predictions, it is necessary to use the self-consistent numerical model.

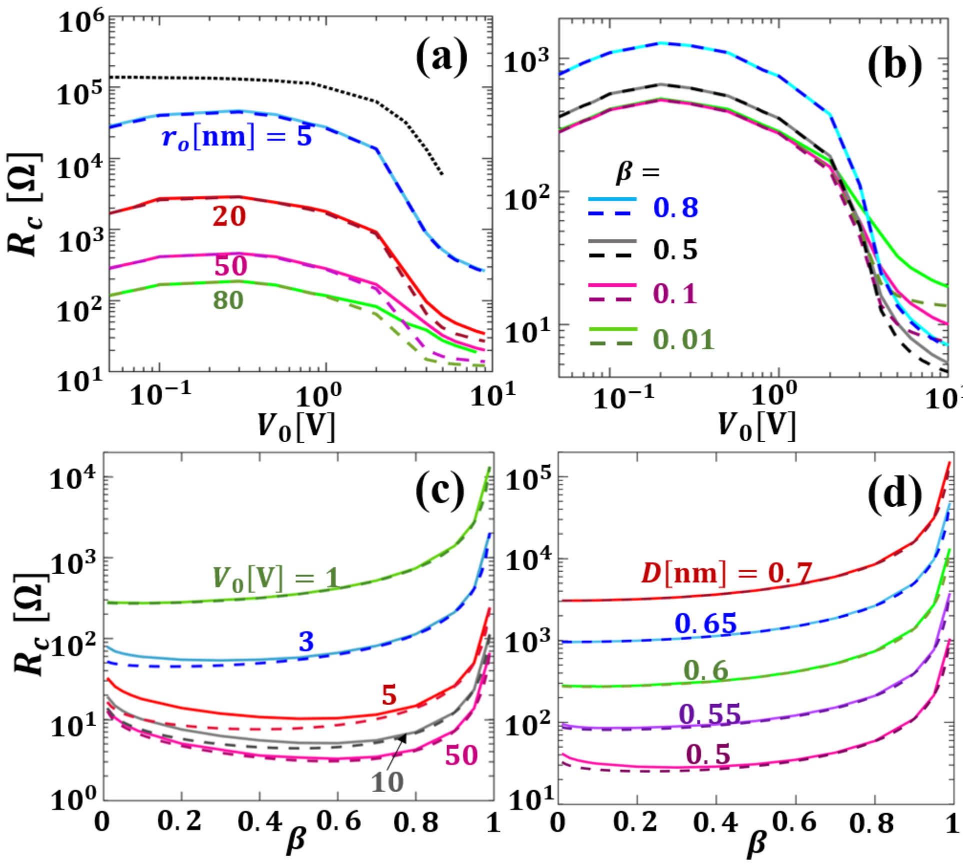

Figure 4.7 The total contact resistance R_c across the Cu-vacuum-Cu contact interface as functions of input voltage V_0 for different (a) outer radius r_0, with fixed $\beta = 0.01$ and $D = 0.6$ nm; (b) inner radius to outer radius ratio β, with fixed $r_0 = 50$ nm and $D = 0.6$ nm. R_c as functions of β for different (c) input voltage V_0, with fixed $r_0 = 50$ nm and $D = 0.6$ nm; (d) interfacial layer thickness D, with fixed $r_0 = 50$ nm and $V_0 = 1$ V. All of the material properties are specified in the main text. Solid lines are for self-consistent numerical calculations using Eqs. (4.4), (4.5), and MIM quantum tunneling formulations (Chapter 2, Sec. 2.2) [5], [6]. The black dotted line in (a) is calculated using Simmons tunneling current formula [5], [14], [15] and Eqs. (4.4), (4.5) for $r_o = 5$ nm. Dashed lines are for analytical calculations from Eqs. (4.8) and (4.9) with ρ_c calculated using $V_g = V_0$ in the 1D MIM tunneling model.

The black dotted line in Fig. 4.7(a) is calculated using Simmons' tunneling current formula [4], [14], [15] and Eqs. (4.4), (4.5) for $r_o = 5$ nm. Clearly, the difference between the quantum based self-consistent calculations and Simmons' formula is substantial. Simmons' formulas, which are widely used for these kinds of studies [4], [12], are inadequate in sub-nm scale (see Fig. 3(a) of Ref. [6]). For low applied voltages, in the direct tunneling regime, the MIM junction behaves ohmically, thus R_c varies slightly with V_0, as shown in Figs. 4.7(a) and 4.7(b). When the applied voltage is increased into the field emission regime (> 1 V), R_c decreases sharply with V_0. This is because the junction is no longer ohmic and the tunneling resistivity ρ_c decreases rapidly and nonlinearly with the junction voltage, which is a function of position along the radial contact length. As V_0 approaches 10 V, space charge effects become important [5], [6], [35], [36], and R_c saturates, increasing only slightly with V_0.

The effect of the inner radius to outer radius ratio of the upper contact member (β) on the total contact resistance (R_c) is shown in Figs. 4.7(b), (c), and (d), showing similar trends to Fig. 4.3(b) above for the case of constant contact resistivity ρ_c. Figure 4.7(d) shows that reducing the insulator layer thickness D even slightly can affect the contact resistance substantially.

Next, we extend our calculations for Cu thin film contacts to different metals: magnesium (Mg), aluminum (Al), gold (Au), and platinum (Pt). The resistivity of a metal thin film ρ_{film} is usually different than the metal's bulk resistivity ρ_{bulk}. ρ_{film} for the metals mentioned above are calculated from $\rho_{film}/\rho_{bulk} = 4/[3(t/l)\log(l/t)]$ for $t < l$ and $\rho_{film}/\rho_{bulk} = 1 + 3/8(l/t)$ for $t > l$ [37], [38] , where l is the electron mean free path and t is the thickness of the thin film (Fig. 4.1). The work function [39], bulk resistivity ρ_{bulk}, and electron mean free path l [37], [40], [41] for the metals are given in Table 4.1. The film thickness is assumed to be $t = 10$ nm for all the cases.

Table 4.1 Material parameters for the Cu-insulator-Metal contacts.

Metal	$\boldsymbol{W_2}$ [eV]	$\boldsymbol{\rho_{bulk}}$ $[\boldsymbol{\Omega m}]$	$\boldsymbol{l}$ [nm]
Mg	3.68 [42]	4.46×10^{-8} [43]	22.3 [40]
Al	4.08 [42]	2.65×10^{-8} [44]	18.9 [40]
Au	5.1 [6]	2.24×10^{-8} [43]	38 [37]
Pt	6.35 [42]	10.6×10^{-8} [44]	12 [41]

Figure 4.8 shows the effects of the work function of contacting member 2 (W_2) and the permittivity of the thin insulating layer (ϵ_r) on the electrical characteristics of Cu-insulator-metal contacts. Figure 4.8(a) shows that the tunneling current density $J_c(r)$ decreases with increasing W_2. Figure 4.8(b) shows that $J_c(r)$ reduces significantly when the permittivity of the insulating layer increases from 1 to 2.5. Figures 4.8(c) and (d) show the contact resistance (in Ω) for various contact metals and tunneling films for Cu-insulator-metal contacts as functions of β. Contact resistance increases with insulating layer permittivity ϵ_r and work function of contacting member 2, W_2. The potential barrier in the insulating layer increases with the increase of the work function of the contact metal, resulting in lower tunneling current and higher contact resistance. On the other hand, ϵ_r greatly influences the image charge potential and space charge potential [5], [6] in the contact interface.

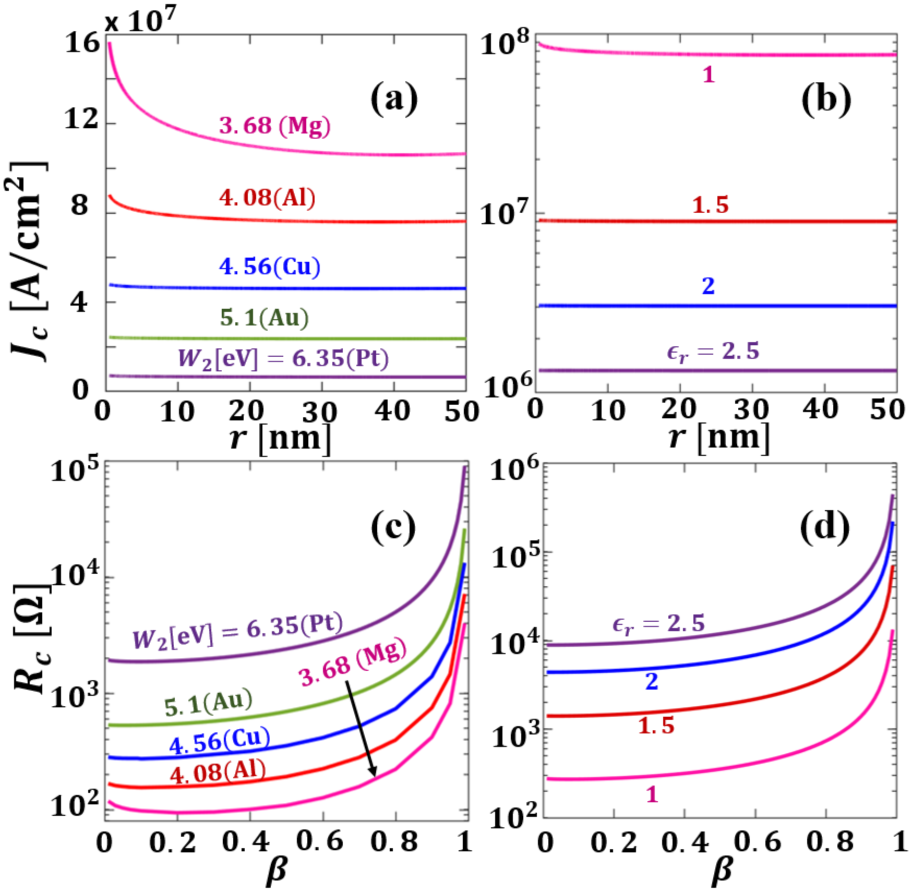

Figure 4.8 Tunneling current density across the Cu-insulator-Metal contact interfaces $J_c(r)$ for different (a) contacting metals with work functions W_2 for fixed $\epsilon_r = 1$, $r_0 = 50$ nm, $\beta = 0.01$, $D = 0.6$ nm, and $V_0 = 1$ V; (b) insulator layer permittivity ϵ_r for fixed $W_2 = 4.08$ (Al), $r_0 = 50$ nm, $\beta = 0.01$, $D = 0.6$ nm, and $V_0 = 1$ V. The total contact resistance R_c across the Cu-insulator-Metal contact interfaces as functions of inner radius to outer radius ratio β for different: (c) W_2 for fixed $\epsilon_r = 1$, $r_0 = 50$ nm, $D = 0.6$ nm, and $V_0 = 1$ V; (d) ϵ_r, for fixed $W_2 = 4.08$ (Al), $r_0 = 50$ nm, $D = 0.6$ nm, and $V_0 = 1$ V. All of the material properties are specified in the main text.

4.4 Concluding Remarks

In this chapter, we presented a self-consistent tunneling model to characterize parallel electrical contacts between two annular thin films. Our model considers the radial variation of contact resistivity along the contact length. We solved the CTLM equations for constant specific contact resistivity and radially varying, tunneling dependent specific contact resistivity along the contact length. Our study provides a thorough understanding of the contact tunneling resistance, current, and voltage distributions across nano and sub-nano scale MIM junctions in circular ring type electrical contacts using an inexpensive model from which many general conclusions may be drawn. The effects of contact geometry (i.e. inner and outer radius of the ring contact, distance between the contact electrodes) and material properties (i.e. work function, sheet resistance of the contact members, and permittivity of the insulating layer) on the radial distributions of currents and voltages across these contacts and the overall contact resistance are studied in detail. The quantum tunneling model includes the effects of image charge, space charge, and exchange correlation potential.

It is found that the contact current density and voltage drop profiles are highly asymmetric at the two edges of the annular contact, even for similar contacting members. This is in sharp contrast to the current and voltage profiles of parallel Cartesian nanocontacts. However, the asymmetry reduces when inner radius to outer radius ratio β increases; for $\beta \rightarrow 1$, the profiles become almost symmetric. Our calculations for tunneling type contacts show that the contact resistance R_c is voltage dependent, increases sharply with D, and decreases with r_o. If β is increased above 0.9, the R_c of the annular contact increases dramatically. It is found that the analytical solutions of one-dimensional (1D) tunneling junction models (constant voltage across the whole junction) are good approximations of the actual circular (annular) contacts only when the thickness D or inner radius to outer radius ratio β is relatively large, or the applied voltage across the contact V_0 or outer radius r_o is relatively small. Otherwise, the 1D tunneling model of constant contact resistivity becomes unreliable, and the self-consistent CTLM equations coupled with the spatially dependent tunneling current need to be used to accurately characterize the electrical contacts.

In existing CTLM [19], [20], the interface contact resistivity is almost always assumed to be constant. Thus, the contact resistivity measured using the transmission line method (TLM) would consist of possible intrinsic errors when thin tunneling (e.g. oxide) layer at the contact interfaces is present. In this case, our model would give more accurate evaluation of contact resistivity. The work presented here may be used to better understand the electrical conductivity of nanofiber and nanorod based thin-film devices, where such circular (or annular) contacts naturally exist. Furthermore, our study reveals that, by varying the contact layer properties and geometry, one can strategically design the radially dependent contact resistivity in circular contacts to achieve desired current distribution. It is worth mentioning that while the work presented here is for tunneling type contacts, our modified CTLM equations with radially varying ρ_c can also be used for other types of contacts such as ohmic and Schottky contacts.

Although a TLM is less computationally expensive and easier to implement, it is a simplified approximation of practical 2D electrical contacts. Field solution methods need to be used in the future to accurately evaluate current crowding and fringing field effects, the impact of finite thickness (or length) in the contact members, and the possible parallel component of current flows in the interface layer [4], [25], [45]–[47]. The effects of reactive elements in the circuit, AC response, and imperfect insulator layer on the electrical properties of tunneling type contacts may also be studied in the future. Future studies may also consider the influence of properties of the materials forming the contact and the possible interaction of the semiconductor (or insulator) films under the contact region, such as Schottky barrier, band bending, charge redistribution, and material defects.

REFERENCES

REFERENCES

[1] S. Banerjee, P. Y. Wong, and P. Zhang, “Contact resistance and current crowding in tunneling type circular nano-contacts,” *J. Phys. D: Appl. Phys.*, vol. 53, no. 35, p. 355301, Jun. 2020, doi: 10.1088/1361-6463/ab8fe0.

[2] P. Zhang, S. B. Fairchild, T. C. Back, and Y. Luo, “Field emission from carbon nanotube fibers in varying anode-cathode gap with the consideration of contact resistance,” *AIP Advances*, vol. 7, no. 12, p. 125203, Dec. 2017, doi: 10.1063/1.5008995.

[3] S. B. Fairchild *et al.*, “Carbon Nanotube Fiber Field Emission Array Cathodes,” *IEEE Trans. Plasma Sci.*, vol. 47, no. 5, pp. 2032–2038, May 2019, doi: 10.1109/TPS.2019.2900219.

[4] S. Banerjee, J. Luginsland, and P. Zhang, “A Two Dimensional Tunneling Resistance Transmission Line Model for Nanoscale Parallel Electrical Contacts,” *Sci Rep*, vol. 9, no. 14484, pp. 1–14, Oct. 2019, doi: 10.1038/s41598-019-50934-2.

[5] S. Banerjee and P. Zhang, “A generalized self-consistent model for quantum tunneling current in dissimilar metal-insulator-metal junction,” *AIP Advances*, vol. 9, no. 8, p. 085302, Aug. 2019, doi: 10.1063/1.5116204.

[6] P. Zhang, “Scaling for quantum tunneling current in nano- and subnano-scale plasmonic junctions,” *Scientific Reports*, vol. 5, p. 9826, May 2015, doi: 10.1038/srep09826.

[7] S. Banerjee, L. Cao, Y. S. Ang, L. K. Ang, and P. Zhang, “Reducing contact resistance by roughness engineering in 2D-material-based electrical contacts,” *under review*.

[8] J. A. de Lima, S. P. Gimenez, and K. H. Cirne, “Modeling and Characterization of Overlapping Circular-Gate mosfet and Its Application to Power Devices,” *IEEE Transactions on Power Electronics*, 2012, doi: 10.1109/TPEL.2011.2117443.

[9] P.-E. Trudeau, M. Sheldon, V. Altoe, and A. P. Alivisatos, “Electrical Contacts to Individual Colloidal Semiconductor Nanorods,” *Nano Lett.*, vol. 8, no. 7, pp. 1936–1939, Jul. 2008, doi: 10.1021/nl080678t.

[10] S. B. Cronin *et al.*, “Making electrical contacts to nanowires with a thick oxide coating,” *Nanotechnology*, vol. 13, no. 5, pp. 653–658, Sep. 2002, doi: 10.1088/0957-4484/13/5/322.

[11] K. Khan *et al.*, “Recent developments in emerging two-dimensional materials and their applications,” *J. Mater. Chem. C*, vol. 8, no. 2, pp. 387–440, Jan. 2020, doi: 10.1039/C9TC04187G.

[12] C. Li, E. T. Thostenson, and T.-W. Chou, “Dominant role of tunneling resistance in the electrical conductivity of carbon nanotube–based composites,” *Appl. Phys. Lett.*, vol. 91, no. 22, p. 223114, Nov. 2007, doi: 10.1063/1.2819690.

[13] A. M. Lord *et al.*, “Controlling the Electrical Transport Properties of Nanocontacts to Nanowires,” *Nano Lett.*, vol. 15, no. 7, pp. 4248–4254, Jul. 2015, doi: 10.1021/nl503743t.

[14] J. G. Simmons, “Generalized Formula for the Electric Tunnel Effect between Similar Electrodes Separated by a Thin Insulating Film,” *Journal of Applied Physics*, vol. 34, no. 6, pp. 1793–1803, Jun. 1963, doi: 10.1063/1.1702682.

[15] J. G. Simmons, “Electric Tunnel Effect between Dissimilar Electrodes Separated by a Thin Insulating Film,” *Journal of Applied Physics*, vol. 34, no. 9, pp. 2581–2590, Sep. 1963, doi: 10.1063/1.1729774.

[16] M. R. Vazirisereshk, S. A. Sumaiya, A. Martini, and M. Z. Baykara, “Measurement of electrical contact resistance at nanoscale gold-graphite interfaces,” *Appl. Phys. Lett.*, vol. 115, no. 9, p. 091602, Aug. 2019, doi: 10.1063/1.5109880.

[17] E. Pop, “Energy dissipation and transport in nanoscale devices,” *Nano Res.*, vol. 3, no. 3, pp. 147–169, Mar. 2010, doi: 10.1007/s12274-010-1019-z.

[18] X. Hu and A. Martini, “Atomistic simulations of contact area and conductance at nanoscale interfaces,” *Nanoscale*, vol. 9, no. 43, pp. 16852–16857, Nov. 2017, doi: 10.1039/C7NR05326F.

[19] G. K. Reeves, “Specific contact resistance using a circular transmission line model,” *Solid-State Electronics*, vol. 23, no. 5, pp. 487–490, May 1980, doi: 10.1016/0038-1101(80)90086-6.

[20] C. Xu, J. Wang, M. Wang, H. Jin, Y. Hao, and C. P. Wen, “Reeves’s circular transmission line model and its scope of application to extract specific contact resistance,” *Solid-State Electronics*, vol. 50, no. 5, pp. 843–847, May 2006, doi: 10.1016/j.sse.2006.03.007.

[21] K. N. Patel, E. Stokes, J. Pagan, C. C. Burkhart, M. Hodge, and P. Batoni, “Circular Transmission Line Model (CTLM) Analysis for Non-Linear VI Characteristics on Mg doped GaN,” *ECS Trans.*, vol. 11, no. 5, pp. 203–208, Sep. 2007, doi: 10.1149/1.2783873.

[22] H. Murrmann and D. Widmann, “Current crowding on metal contacts to planar devices,” *IEEE Transactions on Electron Devices*, vol. 16, no. 12, pp. 1022–1024, Dec. 1969, doi: 10.1109/T-ED.1969.16904.

[23] H. H. Berger, “Contact Resistance and Contact Resistivity,” *J. Electrochem. Soc.*, vol. 119, no. 4, pp. 507–514, Apr. 1972, doi: 10.1149/1.2404240.

[24] D. K. Schroder, *Semiconductor Material and Device Characterization*. Wiley-Blackwell, 1998.

[25] P. Zhang and Y. Y. Lau, “An exact field solution of contact resistance and comparison with the transmission line model,” *Appl. Phys. Lett.*, vol. 104, no. 20, p. 204102, May 2014, doi: 10.1063/1.4878841.

[26] J. G. Simmons, “Conduction in thin dielectric films,” *Journal of Physics D: Applied Physics*, vol. 4, no. 5, pp. 613–657, May 1971, doi: 10.1088/0022-3727/4/5/202.

[27] L. Wu, H. Duan, P. Bai, M. Bosman, J. K. W. Yang, and E. Li, “Fowler-Nordheim tunneling induced charge transfer plasmons between nearly touching nanoparticles,” *ACS Nano*, vol. 7, no. 1, pp. 707–716, Jan. 2013, doi: 10.1021/nn304970v.

[28] M. S. Tsagarakis and J. P. Xanthakis, “Tunneling currents between carbon nanotubes inside the 3-dimensional potential of a dielectric matrix,” *AIP Advances*, vol. 7, no. 7, p. 075012, Jul. 2017, doi: 10.1063/1.4990971.

[29] M. Ieong, B. Doris, J. Kedzierski, K. Rim, and M. Yang, “Silicon device scaling to the sub-10-nm regime,” *Science*, vol. 306, no. 5704, pp. 2057–2060, Dec. 2004, doi: 10.1126/science.1100731.

[30] J. Zheng *et al.*, “Sub-10 nm Gate Length Graphene Transistors: Operating at Terahertz Frequencies with Current Saturation,” *Scientific Reports*, vol. 3, no. 1, Art. no. 1, Feb. 2013, doi: 10.1038/srep01314.

[31] M. S. Ghamsari and S. Dhara, *Nanorods and Nanocomposites*. 2020.

[32] M. A. Mackey, M. R. K. Ali, L. A. Austin, R. D. Near, and M. A. El-Sayed, “The Most Effective Gold Nanorod Size for Plasmonic Photothermal Therapy: Theory and In Vitro Experiments,” *J. Phys. Chem. B*, vol. 118, no. 5, pp. 1319–1326, Feb. 2014, doi: 10.1021/jp409298f.

[33] S. E. Wawra, L. Pflug, T. Thajudeen, C. Kryschi, M. Stingl, and W. Peukert, “Determination of the two-dimensional distributions of gold nanorods by multiwavelength analytical ultracentrifugation,” *Nature Communications*, vol. 9, no. 1, Art. no. 1, Nov. 2018, doi: 10.1038/s41467-018-07366-9.

[34] E. Schmiedl, P. Wissmann, and H.-U. Finzel, “The Electrical Resistivity of Ultra-Thin Copper Films,” *Zeitschrift für Naturforschung A*, vol. 63, no. 10–11, pp. 739–744, 2014, doi: 10.1515/zna-2008-10-1118.

[35] Y. Y. Lau, D. Chernin, D. G. Colombant, and P.-T. Ho, “Quantum extension of Child-Langmuir law,” *Physical Review Letters*, vol. 66, pp. 1446–1449, Mar. 1991, doi: 10.1103/PhysRevLett.66.1446.

[36] L. K. Ang, T. J. T. Kwan, and Y. Y. Lau, “New Scaling of Child-Langmuir Law in the Quantum Regime,” *Phys. Rev. Lett.*, vol. 91, no. 20, p. 208303, Nov. 2003, doi: 10.1103/PhysRevLett.91.208303.

[37] K. L. Chopra, L. C. Bobb, and M. H. Francombe, “Electrical Resistivity of Thin Single-Crystal Gold Films,” *Journal of Applied Physics*, vol. 34, no. 6, pp. 1699–1702, Jun. 1963, doi: 10.1063/1.1702662.

[38] K. Fuchs, “The conductivity of thin metallic films according to the electron theory of metals,” *Mathematical Proceedings of the Cambridge Philosophical Society*, vol. 34, no. 1, pp. 100–108, Jan. 1938, doi: 10.1017/S0305004100019952.

[39] D. R. Lide, G. Baysinger, S. Chemistry, L. I. Berger, R. N. Goldberg, and H. V. Kehiaian, *CRC Handbook of Chemistry and Physics*. 2003.

[40] D. Gall, “Electron mean free path in elemental metals,” *Journal of Applied Physics*, vol. 119, no. 8, p. 085101, Feb. 2016, doi: 10.1063/1.4942216.

[41] G. Fischer, H. Hoffmann, and J. Vancea, “Mean free path and density of conductance electrons in platinum determined by the size effect in extremely thin films,” *Phys. Rev. B*, vol. 22, no. 12, pp. 6065–6073, Dec. 1980, doi: 10.1103/PhysRevB.22.6065.

[42] P. A. Tipler and R. Llewellyn, *Modern Physics*, 6th ed. Freeman, 2012.

[43] “Resistivity and Conductivity - Temperature Coefficients for Common Materials.” https://www.engineeringtoolbox.com/resistivity-conductivity-d_418.html.

[44] D. C. Giancoli, *Physics*, 4th ed. Prentice Hall, 1995.

[45] P. Zhang, Y. Y. Lau, and R. M. Gilgenbach, “Analysis of current crowding in thin film contacts from exact field solution,” *J. Phys. D: Appl. Phys.*, vol. 48, no. 47, p. 475501, 2015, doi: 10.1088/0022-3727/48/47/475501.

[46] P. Zhang, D. M. H. Hung, and Y. Y. Lau, “Current flow in a 3-terminal thin film contact with dissimilar materials and general geometric aspect ratios,” *J. Phys. D: Appl. Phys.*, vol. 46, no. 6, p. 065502, Feb. 2013, doi: 10.1088/0022-3727/46/6/065502.

[47] P. Zhang, Y. Y. Lau, and R. M. Gilgenbach, “Minimization of thin film contact resistance,” *Appl. Phys. Lett.*, vol. 97, no. 20, p. 204103, Nov. 2010, doi: 10.1063/1.3517497.

CHAPTER 5

2D-MATERIAL-BASED SCHOTTKY CONTACTS

This chapter is based on the published journal paper “Reducing Contact Resistance in Two-Dimensional-Material-Based Electrical Contacts by Roughness Engineering”, Phys. Rev. Appl., vol. 13, no. 6, p. 064021, Jun. 2020, doi: 10.1103/PhysRevApplied.13.064021, by **S. Banerjee**, L. Cao, Y. S. Ang, L. K. Ang, and P. Zhang [1]. It is presented here with the permission of the copyright holder.

5.1 Introduction

The undesirably large contact resistance between two-dimensional (2D) semiconductor and three-dimensional (3D) metallic electrodes represent one of the major obstacles towards the development of practical 2D electronic and optoelectronic devices[2]. The engineering of better electrical contacts has become a key research objective in recent years. Extensive efforts have been made to improve current flow through contacts and device performance in 2D material based devices[3]–[8]. Recent experimental breakthroughs have demonstrated that the van der Waals metal contact to 2D semiconductor can significantly improve the quality of electrical contact[9], [10]. This advancement opens up exciting avenues for the exploration how 2D/3D electrical contacts can be further improved. This motivates the need of a physical model that comprehensively includes both the material properties of 2D semiconductors and the geometrical electrostatic effect in mixed-dimensional nanostructures, which remains rarely studied in the literature thus far.

In this chapter, we present a consistent model for calculating the contact resistance, which is important for realizing 2D-material-based electronics. The model is based on the self-consistent spatial-dependent transmission line model (TLM) developed in Chapter 3, the correct charge injected model for 2D material based electrical contacts, and the effects of roughness [1]. The recently developed thermionic charge injection model in 2D materials[11] is coupled with the 2D transmission line model (TLM) accounting for the varying specific contact resistivity along the contact length[12]. The profiles of current and voltage distribution along contact region and the total contact resistance are calculated for various input voltage, contact dimension, material properties, and temperature. It is found the one-dimensional (1D) models become less reliable when Schottky barrier height (SBH) becomes smaller or when the applied voltage becomes larger, where our self-consistent model is expected to provide an improved evaluation of the 2D-material-based electrical contacts. Our self-consistent calculation results have been compared with that using the classic Richardson-Dushman (RD) thermionic law. We found that RD law significantly underestimates the contact resistance and overestimates the contact current density for 2D-material-based contacts. We obtain excellent agreement by comparing our numerically calculated results with the reported experimental data [10], [13], [14].

We further incorporate the effects of interface roughness in the 3D/2D electrical contacts in our 2D TLM model. The interface roughness can be introduced (or engineered) by substrate doping[15] and is inherently present due to the inevitable presence of interfacial defects during the fabrication process. The impact of surface roughness on contact resistance for ohmic contacts have been studied previously[16]–[19]. Previous experiment has also demonstrated that substrate roughness can improve the mobility of 2D transition metal dichalcogenide (TMD) by several orders of magnitude[20]. In our model, the contact interface roughness is modelled as fluctuating Schottky barrier heights (SBH)[21] along the electrical contacts. Using experimental device parameters of Au/MoS_2 electrical contact[13], we show that the contact resistance at the 2D/3D Schottky contact can be reduced by more than one order of magnitude. The key finding that roughness can improve the 2D/3D electrical contact quality further highlights the technological importance of roughness engineering for improving the device performance of 2D electronics and optoelectronics. Our findings pave a theoretical foundation for the modeling of contact resistance in 2D/2D and 2D/3D electrical contact and establishes a new viable route towards the design of better electrical contacts to 2D materials using roughness engineering.

5.2 The Model

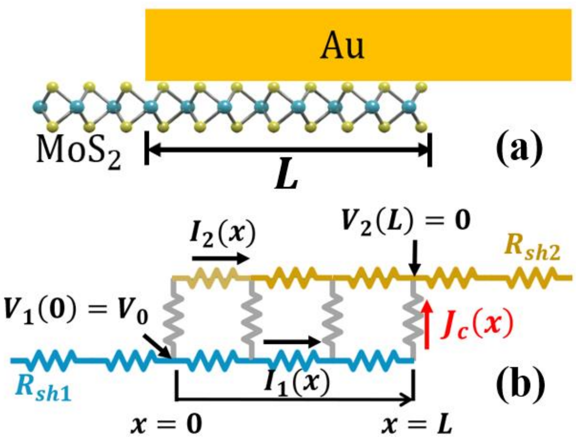

Figure 5.1 (a) A typical parallel contact between Au and MoS_2. (b) its transmission line model. The width (transverse dimension) of the two contact members is w.

Due to the reduced dimensionality and the exotic electronic properties of 2D materials, the electron emission physics deviates significantly from traditional 3D materials [11], [22]–[24]. The thermionic emission of charged carriers across a 2D-material-based metal/semiconductor Schottky contact is found to be universally governed by a simple current-temperature $(J - T)$ scaling law [11], $\ln(J/T^{\beta}) = A - B/T$, where A and B are materials/device-dependent parameters, and $\beta = 1$ (and 3/2) for a vertical (and lateral) Schottky contact. For 2D transition metal dichalcogenide (TMDC), such as atomically-thin MoS_2, the thermionic emission is governed by

$$J_{th}(V,T) = \frac{2e\Phi_{B0}k_BT}{\pi\tau\hbar^2 v_F^2}\left(1+\frac{k_BT}{\Phi_{B0}}\right)\exp\left(-\frac{\Phi_{B0}-\varepsilon_F}{k_BT}\right), \tag{5.1}$$

where Φ_{B0} is the intrinsic SBH, the Fermi velocity $v_F = 1.1 \times 10^6$ m/s for MoS_2, ε_F is the Fermi level, and $\tau \approx (0.1 \sim 10)$ ps is the carrier injection time determined experimentally [25]. Equation (5.1) deviates significantly from the classic Richardson-Dushman (RD) thermionic law for 3D materials, i.e. $\ln(J_{3D}/T^2) \propto 1/T$ [26]. The Shockley diode equation can thus be modified as

$$J_{2D}(V,T) = J_{th}(V,T)\left[\exp\left(\frac{eV}{k_BT}\right)-1\right], \tag{5.2}$$

which is obtained based on the detailed balance principle [26]. Equation (5.2) represents the generalized 2D Shockley diode equation for 2D electronic systems. For comparison, the Shockley diode equation based on the 3D classic RD thermionic law is $J_{3D}(V,T) = J_{RD}(V,T)\left[\exp\left(\frac{eV}{k_BT}\right)-1\right]$, where $J_{RD}(V,T) = \frac{4\pi m^* k_B^2 e}{h^3}T^2\exp\left(-\frac{\Phi_{B0}-\varepsilon_F}{k_BT}\right)$, $m^* = 0.54m_e$[27], m_e is the mass of an electron.

TLM equations developed in Chapter 3 (Eqs. 3.5 and 3.6) coupled with Eq. 5.2 are used to predict the profiles of current and voltage distributions, and the total contact resistance in nanoscale 2D/3D Schottky contacts (Fig. 5.1). The contact current density $J_c(x)$ in Fig. 5.1 is calculated iteratively from the coupled TLM with Eq. 5.2. Sheet resistance of MoS_2 under the contact can be calculated semi-empirically [13] as, $R_{sh} = 1/ne\mu(T)$, where n is the 2D carrier density with typical value of 5×10^{12} cm^{-2}, e is the electric charge, and $\mu(T) = \mu_0(T/300)^{-1.6}$ is the temperature-dependent mobility.

5.3 Results and Discussion

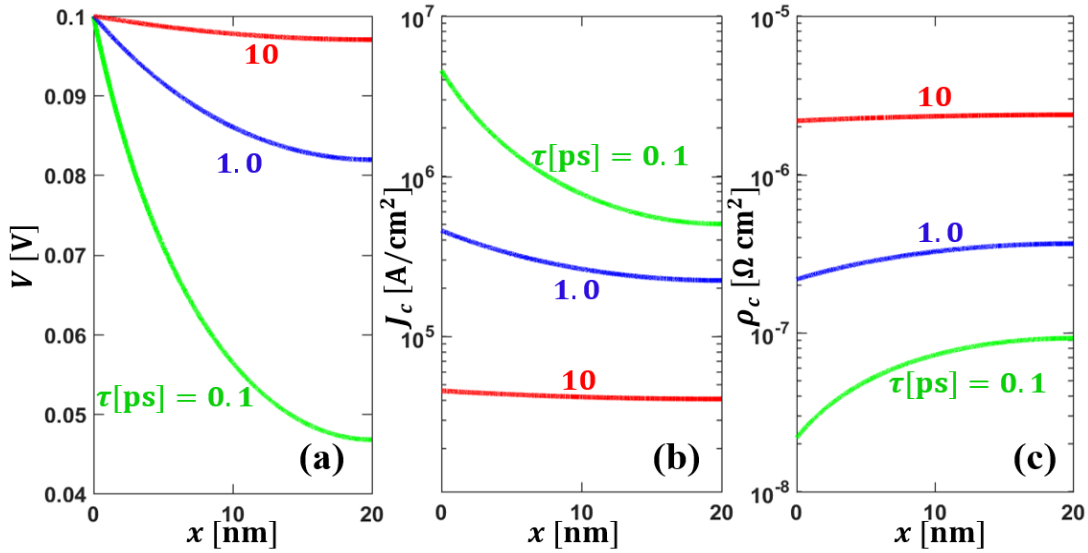

Figure 5.2 (a) Voltage drop $V(x)$, (b) current density $J_c(x)$, and (c) specific contact resistivity $\rho_c(x)$ across the contact interface for a monolayer MoS_2 (2D semiconductor) and gold (3D metal) contact for different carrier injection time τ with fixed applied voltage $V_0 = 0.1$ V, and contact length $L = 20$ nm. Here, $R_{sh1}(MoS_2) = 35714\ \Omega/\square$, $R_{sh2}(Au) = 4.4\ \Omega/\square$, $\phi_B = 0.1$ eV , $\varepsilon_F = 0.8$ eV and $T = 300$ K. [1]

In Fig. 5.2, we show the self-consistent calculation of the voltage drop $V(x)$, injection current density $J_c(x)$, and the contact resistivity $\rho_c(x)$ across the contact region for a fixed bias voltage of $V_0 = 0.1$ V with different interface charge injection time, τ, for a MoS_2/Au contact using the experimentally determined device parameter reported previously [13]. In Fig. 5.2(a), it is found that $V(x)$ is nonuniform across the contact length. The variation of the $V(x)$ increases with a decreasing charge injection time, which indicates a stronger current crowding effect in 2D/3D interface with high carrier injection efficiency, as shown in Fig. 5.2(b). This is consistent with previous studies that current crowding effect increases with more conductive contact interfaces[28], [29]. The spatial dependent contact resistivity is more evenly distributed across the contact region for contact with longer injection time [Fig. 5.2(c)].

In Figs. 5.3(a) and 5.3(b), the contact resistance R_c calculated from Eqs. (3.4) is shown as a function of the bias voltage for two different SBHs for 2D/3D contacts. The 2D/3D contact exhibits a transition from Schottky contact characteristic, in which R_c increases with decreasing temperature for $V_0 < \Phi_B$, to a Ohmic contact characteristic, in which R_c increases with increasing temperature for $V_0 > \Phi_B$. Such transition is due to the offset of the SBH by the external bias voltage. In Figs. 5.3(c) and 5.3(d), the temperature dependence of R_c further confirms the Schottky-to-ohmic transition at $V_0 \sim \Phi_B$ observed in Figs. 5.3(a) and 5.3(b), which is also consistent with the experiments [13].

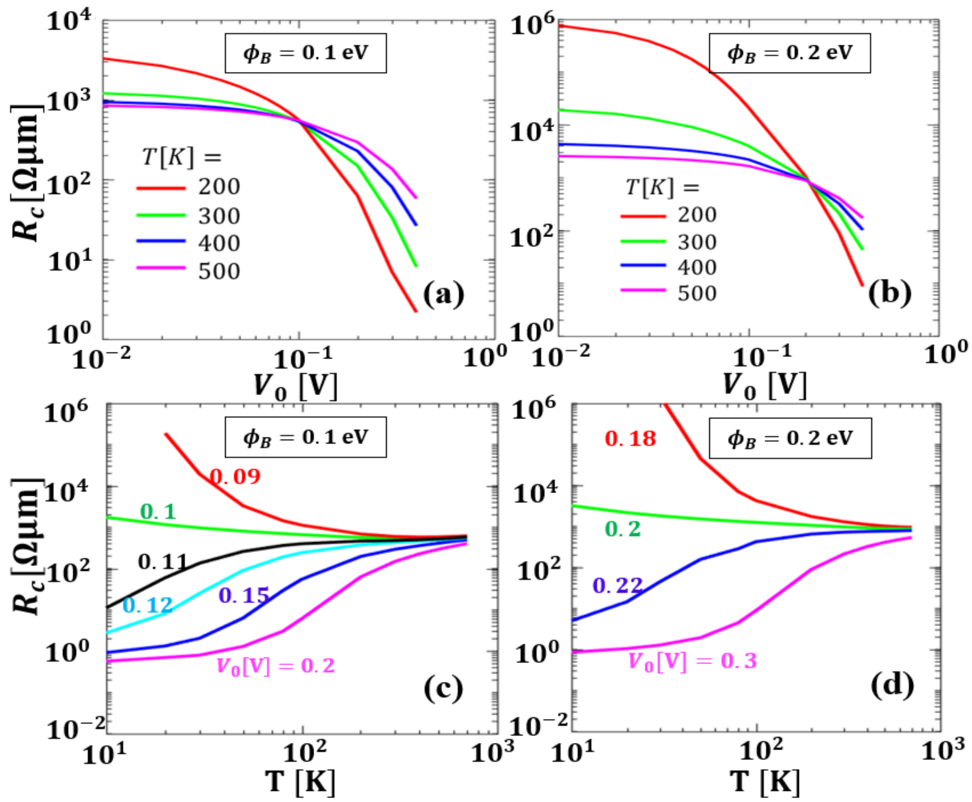

Figure 5.3 Contact resistance R_c as a function of applied voltage V_0 for different T, for (a) $\Phi_B = 0.1$ eV, (b) $\Phi_B = 0.2$ eV. R_c as a function of temperature T for different V_0, for (c) $\Phi_B = 0.1$ eV, (d) $\Phi_B = 0.2$ eV. Here, the contact is between a monolayer MoS_2 and Au, with $\tau = 0.1$ ps, and $L = 50$ nm. [1]

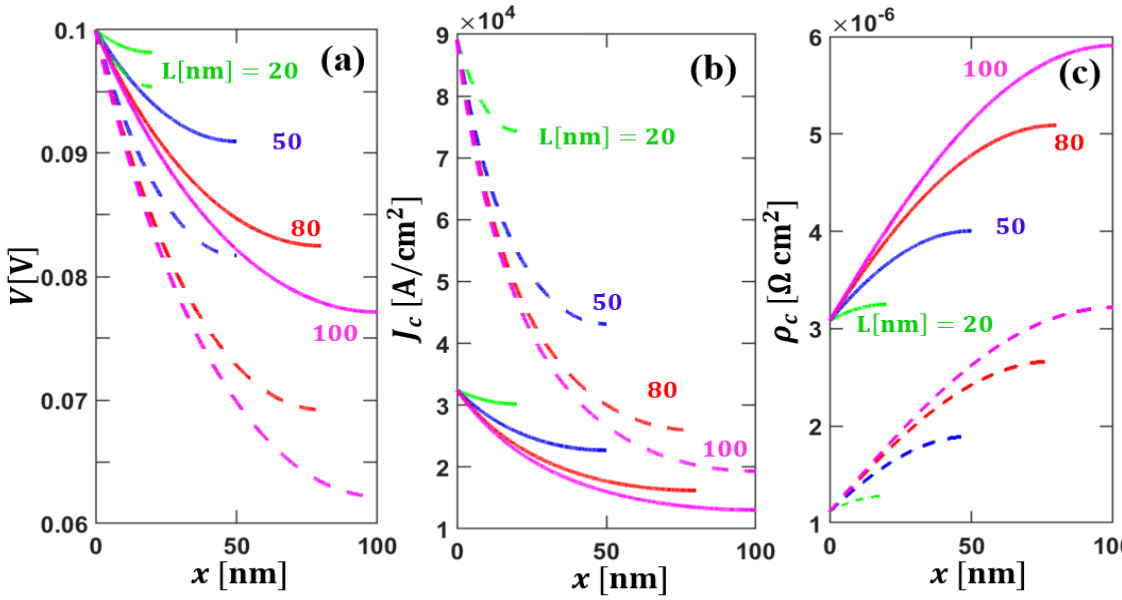

Figure 5.4 (a) Voltage drop $V(x)$, (b) current density $J_c(x)$, and (c) specific contact resistivity $\rho_c(x)$ across the contact interface for MoS_2/Ag contact for different contact length L with fixed applied voltage $V_0 = 0.1$ V. Solid lines are for the self-consistent calculations of Model (A), and dashed lines are for Model (C). See text for details. Here, $\tau = 0.1$ ps, $R_{sh1}(MoS_2) = 30000\ \Omega/\square$, $R_{sh2}(Ag) = 3.18\ \Omega/\square$, $\varepsilon_F = 0.249$ eV, $\phi_B = 0.212$ eV, and $T = 300$ K. [1]

In Fig. 5.4 the $V(x)$, $J_c(x)$, and $\rho_c(x)$ for MoS_2/Ag contact are shown for varying contact length L. The current crowding is strongly amplified in the case of long contact length, because the applied voltage is distributed over a longer resistive network, resulting in increased interface contact resistivity due to the voltage-dependent Schottky barriers. The influence of L on R_c is shown in Fig. 5.5 for different applied voltages. In Figs. 5.4 and 5.5, we calculate the results using four different approaches: Model (A): self-consistent calculations using Eqs. (3.5),(3.6) and (5.2) (solid lines); Model (B): analytical solution (3.7), assuming constant ρ_c, calculated using fixed $V = V_0$ in Eq. (5.2) (dotted lines); Model (C): calculations of Eq. (3.5),(3.6) with the 3D Richardson-Dushman injection model $J_{3D}(V,T)$ (dashed lines); and Model (D): analytical solution (3.7) assuming constant ρ_c, calculated using fixed $V = V_0$ in the Richardson-Dushman injection model $J_{3D}(V,T)$(dash-dotted lines). It is found that, for 2D-3D contacts, the classic Richardson-Dushman injection model significantly underestimates the contact resistance and overestimates the contact current density. We also found that, as V_0 increases, the analytical solutions [12] of the TLM with constant ρ_c calculated using $V = V_0$ in the charge injection model, which is almost always used in the literature[10], [13], [14], become less reliable; and our proposed self-consistent model may be used to obtain a more accurate evaluation of such contacts. This aspect is particularly important in the development of industrial-grade field-effect transistor based on 2D semiconductors. According to the International Roadmap of Devices and Systems (IRDS)[30], the required industry standard bias voltage is 0.65 V and 0.60 V, respectively, for year 2021 and 2030. At these bias-voltage values, we found that the analytical model with both constant ρ_c and Richardson thermionic injection model severely underestimate the contact resistance by at least 75% (Model (B)), 30% (Model (C)), and 83% (Model (D)) when compared to our self-consistent model combined with the 2D thermionic charge injection theory (Model (A)), over a wide range of contact length L of 20 nm – 100 nm.

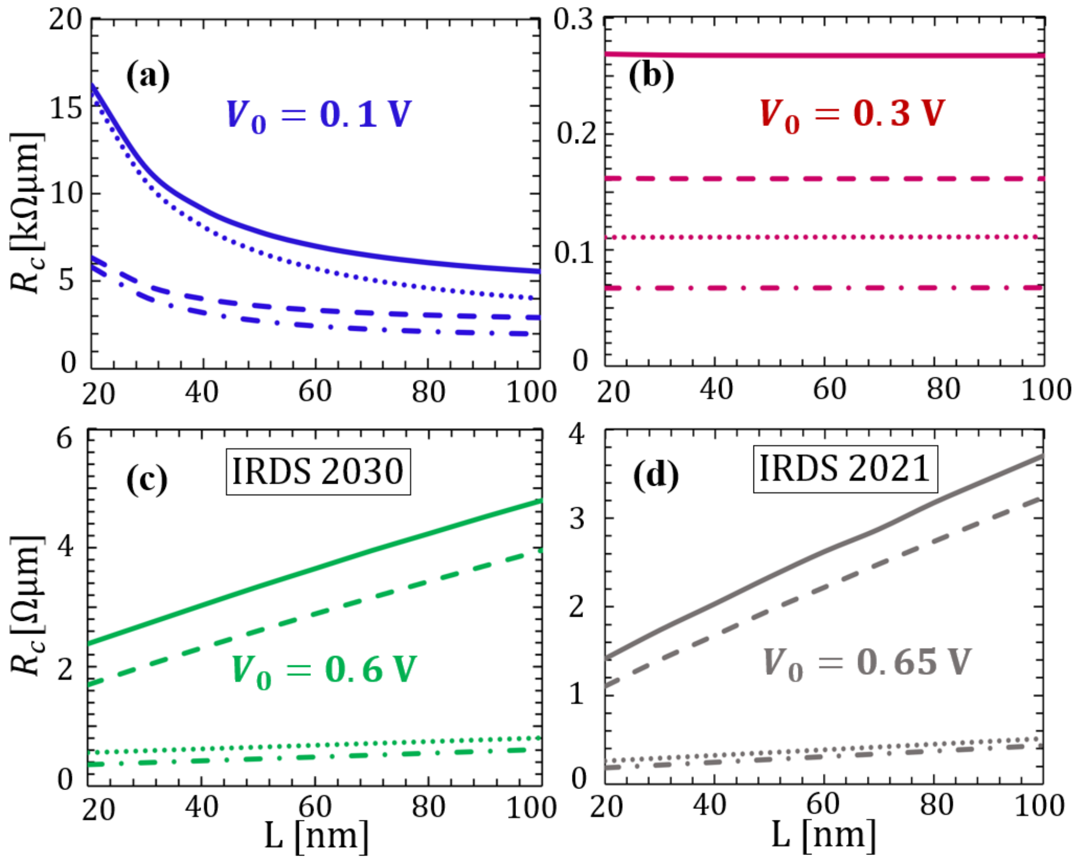

Figure 5.5 Contact resistance R_c for MoS_2/Ag contact as a function of contact length L for different applied bias V_0 = (a) 0.1 V, (b) 0.3 V, (c) 0.60 V, and (d) 0.65 V. The two bias voltages in (c) and (d) are the required industry standards according to the International Roadmap of Devices and Systems (IRDS) [30] for year 2030 and 2021, respectively. Solid lines are for the self-consistent calculations of Model (A), dotted lines are for Model (B), dashed lines are for Model (C), and dash-dotted lines are for Model (D). See text for details. Here, $\tau = 0.1$ ps, $R_{sh1}(MoS_2) = 30000\ \Omega/\square$, $R_{sh2}(Ag) = 3.18\ \Omega/\square$, $\varepsilon_F = 0.249$ eV, $\phi_B = 0.212$ eV, and $T = 300$ K. [1]

Next, we compare our self-consistent model with the existing experimental works (c.f. Figs. 5.6 and 5.7), for various 2D carrier density n, temperature, and MoS_2 − metal interface. With suitable values of V_0 and τ, the results from our self-consistent model are in excellent agreement with the experimental data. Figure 5.6 shows that for a given temperature T, the contact resistance R_c decreases with n, as it has been reported previously [10], [13], [14]. It is evident that, calculations from our self-consistent model provide much better fitting to the experimental data for 2D material-metal electrical contacts than models based on 3D Richardson-Dushman injection law.

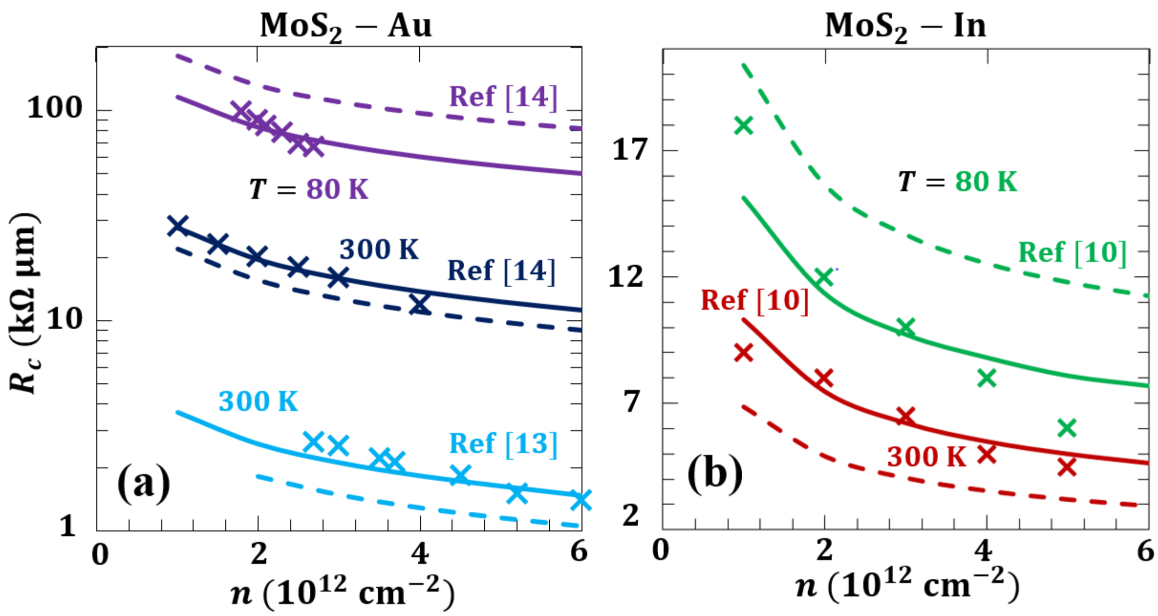

Figure 5.6 R_c **as a function of 2D carrier density** n **for different temperatures for (a)** $MoS_2 - Au$ **contacts, and (b)** $MoS_2 - In$ **contacts. Crossed symbols are from experiments [10], [13], [14]; solid lines are from our self-consistent model from Eqs. 3.5, 3.6 and 5.2, Model (A); and dashed lines are from Eqs. (3.5), (3.6) with the Richardson-Dushman injection model, Model (C). In the calculation, we used** $R_{sh}(Au) = 2.2\ \Omega/\square$, $R_{sh}(In) = 8.37\ \Omega/\square$, $\mu_0 = 20\ cm^2V^{-1}S^{-1}$ **for** $MoS_2 - Au$ **contacts [13], and** $\mu_0 = 170\ cm^2V^{-1}S^{-1}$ **for** $MoS_2 - In$ **contacts [10]. The parameters** $\varepsilon_F = 0.077$ **eV [31],** 0.6 **eV [10],** 0.5 **eV,** $\phi_B = 0.763$ **eV [31],** 0.3 **eV [10],** 0.15 **eV [13], and** $\tau = 0.1$ **ps,** 0.15 **ps,** 0.1 **ps are used to fit the experimental results in Refs. [14], [10] , [13] respectively. For different cases, from top to bottom, different input voltages** $V_0 = 0.731$ **V,** 0.7 **V,** 0.1 **V and** $V_0 = 0.271$ **V,** 0.17 **V are used in (a) and (b) respectively.** $L = 500$ **nm [13] is assumed for all the cases. [1]**

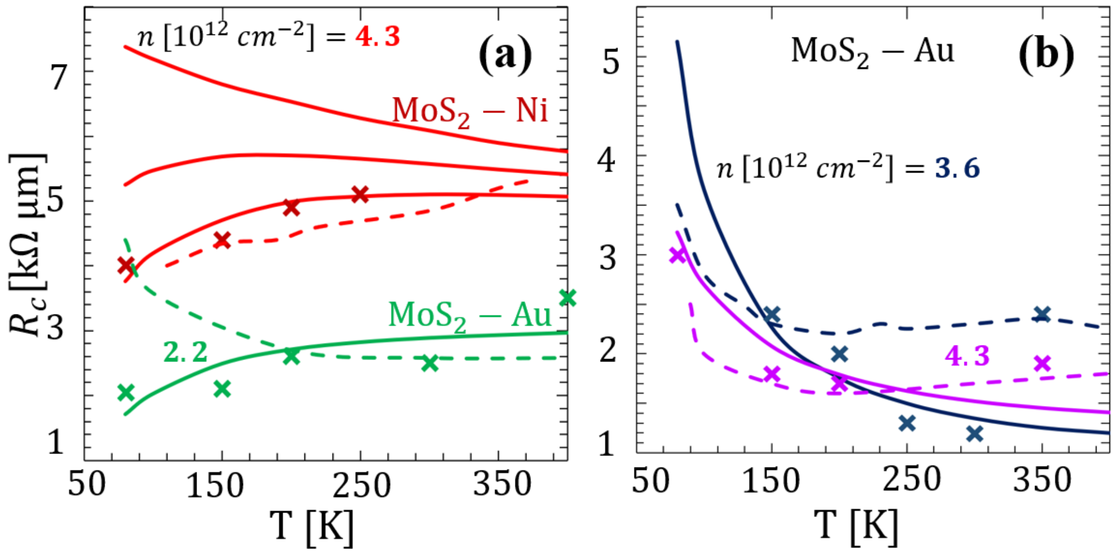

Figure 5.7 R_c as a function of temperature T with (a) an increasing trend, and (b) a decreasing trend, for $MoS_2 -$ metal contacts with different n. Crossed symbols are from experiments[10], [13], [14]; solid lines are from our self-consistent Model (A), and dashed lines are extracted from model calculations in Ref. [13]. In the calculation, we used $R_{sh}(Au) = 2.2\ \Omega/\square$, and $R_{sh}(Ni) = 13.8\ \Omega/\square$. The parameters $\varepsilon_F = 0.588$ eV, $\phi_b = 0.633$ eV [31], and $\varepsilon_F = 0.5$ eV, $\phi_b = 0.150$ eV [13] are used for $MoS_2 -$ Ni, Au contacts respectively. In (a), for the three solid red lines, from top to bottom, $V_0 = 0.635$ V, 0.64 V, 0.645 V, respectively, and all with $\tau = 0.45$ ps; for the green solid line, $V_0 = 0.165$ V, and $\tau = 0.7$ ps. In (b), $V_0 = 0.13$ V, 0.141 V and $\tau = 0.1$ ps, 0.2 ps for the blue and purple solid lines, respetively. The value of $\mu_0 = 20\ cm^2V^{-1}S^{-1}$ [13], and $L = 500$ nm [13] is assumed for all the cases. [1]

Figure 5.7 shows the comparison of our self-consistent model with experiments on R_c as a function of temperature T for different n, for $MoS_2 -$ metal contacts. For all the cases, our self-consistent calculation from Model (A) (solid lines) provides a much better fitting to the experimental data (symbols) compared to existing models [10], [13], [14] (dashed lines). The three red lines in Fig. 5.7(a), with input voltage $V_0 = 0.635$ V, 0.64 V, 0.645 V from top to bottom, show that the increasing (ohmic characteristic) or decreasing (Schottky characteristic) trends of R_c with temperature depends very sensitively on the input voltage V_0 to the contact, which is also evident in Fig. 5.3. This voltage dependence of the contact resistance has not been emphasized and is generally missing in the previous works [10], [13], [14]. Our model suggests that the input voltage must be specified in order to give a meaningful characterization of contact resistance for a given 2D material-metal contacts.

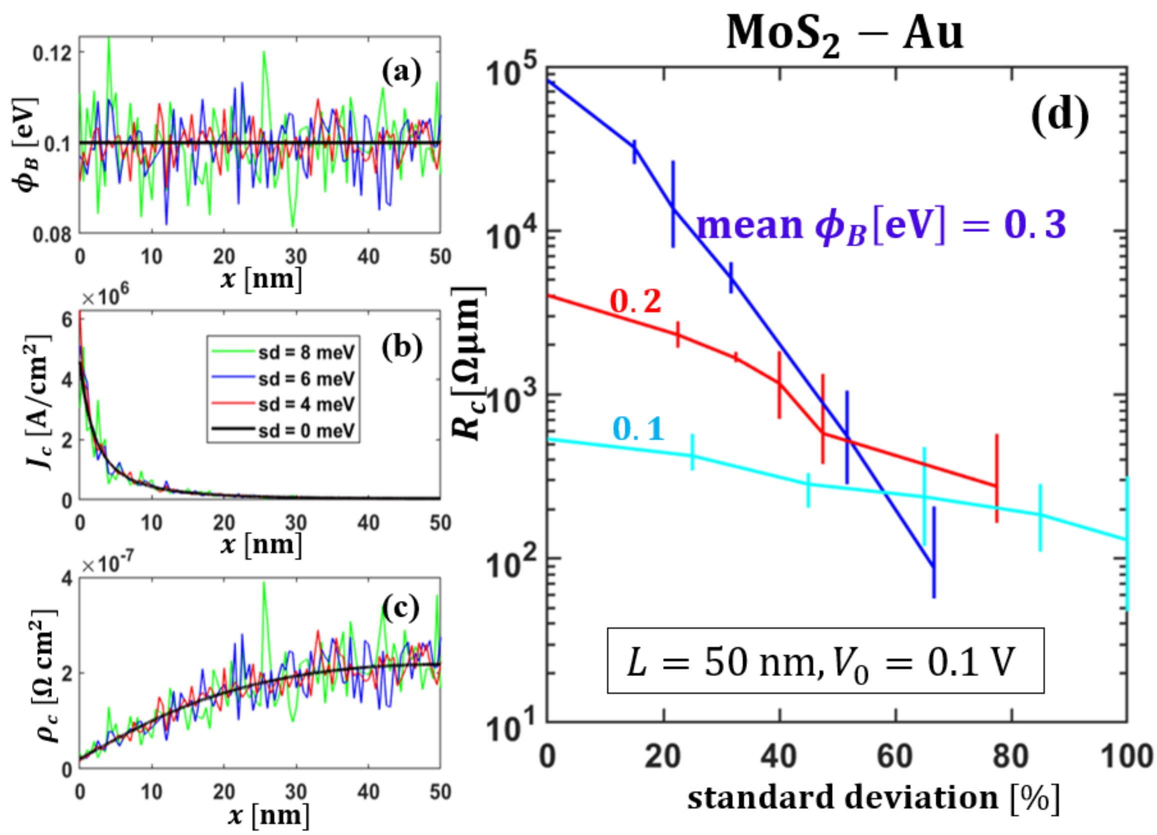

Figure 5.8 (a) Roughness in Schottky barrier height ϕ_B, the resulting (b) current density $J_c(x)$, and (c) specific contact resistivity $\rho_c(x)$ across the contact interface for a monolayer MoS_2-Au 2D/3D contact for different standard deviations (sd). (d) Contact resistance R_c as a function of surface roughness (standard deviation/ϕ_B) for different mean values of ϕ_B. Here, applied voltage $V_0 = 0.1$ V, and contact length $L = 50$ nm. [1]

We further model the effect of interface's roughness at the 2D/3D electrical contact by including a SBH fluctuation term, i.e. $\Phi_B \rightarrow \Phi_B + \Delta\Phi_B$, where $\Delta\Phi_B$ is calculated by assuming that the SBH fluctuation follows a Gaussian distribution. The fluctuation of the SBH, injection current and contact resistivity profiles are shown in Figs. 5.8(a)-5.8(c) respectively. As shown in Fig. 5.8(d), the SBH variation has a dramatic effect on the contact resistance. In general, R_c is reduced significantly in the presence of roughness. Such reduction is particularly effective for

MoS_2/Au contact with large SBH (e.g. 0.3 eV). Such roughness-induced contact resistance reduction is reminiscent to the previously reported mobility enhancement of 2D TMDs due to the presence of crested rough substrate [20]. Thus, the finding in Fig. 5.8(d) suggests that roughness not only improves the mobility but also decreases the contact resistance with 3D metals. The reduction of contact resistance with interface roughness is also achieved in 1D electrical contacts, i.e. both contact members with constant voltages applied uniformly across the contact region (not shown).

The reduction in contact resistance due to fluctuation of interface resistance can be easily understood from a general circuit theory. Consider a rough resistive interface presented between two conductors. Because of fluctuation of the conductivity along the interface, there will be local regions of highly conductive spots formed, whose resistance can be much smaller than that of a uniform interface. Such a resistive interface may be considered as a set of equivalent element resistors connected in parallel along the interface between the two contacting members, whose total interface resistance is $R_{total} = 1/\left(\frac{1}{R_1} + \frac{1}{R_2} + \cdots + \frac{1}{R_N}\right) \sim \{R_i\}_{minimum}$, which is determined by the smallest resistor in the parallel connection, i.e. the equivalent resistor at the highly conductive spots. As a result, this leads to a reduced overall interface resistance compared to a uniform interface. Note the interface "roughness" represents the variation or fluctuation in the conductivity along the interface (e.g. induced by doping, SBH, etc) and needs not be to physical roughness. Similar benefits of surface roughness are found to decrease the contact resistance in organic transistors [17] and to increase the mobility of charge carrier injection in organic and 2D transistors [17],[20].

5.4 Concluding Remarks

A self-consistent transmission line model to quantify and model the current distribution and contact resistance in 2D materials based contacts is constructed and validated with the existing experimental works. It is found that interface roughness can significantly reduce 2D/3D electrical contact resistance. Our findings provide a theoretical foundation for the modeling of 2D/2D and 3D/2D electrical contacts and further reveal a new route towards efficient 2D material electrical contact through roughness engineering.

REFERENCES

REFERENCES

[1] S. Banerjee, L. Cao, Y. S. Ang, L. K. Ang, and P. Zhang, "Reducing Contact Resistance in Two-Dimensional-Material-Based Electrical Contacts by Roughness Engineering," *Phys. Rev. Applied*, vol. 13, no. 6, p. 064021, Jun. 2020, doi: 10.1103/PhysRevApplied.13.064021.

[2] A. Allain, J. Kang, K. Banerjee, and A. Kis, "Electrical contacts to two-dimensional semiconductors," *Nat Mater*, vol. 14, no. 12, pp. 1195–1205, Dec. 2015, doi: 10.1038/nmat4452.

[3] S. Das, H.-Y. Chen, A. V. Penumatcha, and J. Appenzeller, "High Performance Multilayer MoS2 Transistors with Scandium Contacts," *Nano Lett.*, vol. 13, no. 1, pp. 100–105, Jan. 2013, doi: 10.1021/nl303583v.

[4] H.-Y. Chang *et al.*, "High-Performance, Highly Bendable MoS2 Transistors with High-K Dielectrics for Flexible Low-Power Systems," *ACS Nano*, vol. 7, no. 6, pp. 5446–5452, Jun. 2013, doi: 10.1021/nn401429w.

[5] Y. Xu *et al.*, "Contacts between Two- and Three-Dimensional Materials: Ohmic, Schottky, and *p* – *n* Heterojunctions," *ACS Nano*, vol. 10, no. 5, pp. 4895–4919, May 2016, doi: 10.1021/acsnano.6b01842.

[6] X. Ding *et al.*, "NbS2: A Promising p-Type Ohmic Contact for Two-Dimensional Materials," *Phys. Rev. Applied*, vol. 12, no. 6, p. 064061, Dec. 2019, doi: 10.1103/PhysRevApplied.12.064061.

[7] Y. Liu, P. Stradins, and S.-H. Wei, "Van der Waals metal-semiconductor junction: Weak Fermi level pinning enables effective tuning of Schottky barrier," *Science Advances*, vol. 2, no. 4, p. e1600069, Apr. 2016, doi: 10.1126/sciadv.1600069.

[8] F. Zhang, W. Li, Y. Ma, Y. Tang, and X. Dai, "Tuning the Schottky contacts at the graphene/WS2 interface by electric field," *RSC Adv.*, vol. 7, no. 47, pp. 29350–29356, Jun. 2017, doi: 10.1039/C7RA00589J.

[9] Y. Liu *et al.*, "Approaching the Schottky–Mott limit in van der Waals metal–semiconductor junctions," *Nature*, vol. 557, no. 7707, pp. 696–700, May 2018, doi: 10.1038/s41586-018-0129-8.

[10] Y. Wang *et al.*, "Van der Waals contacts between three-dimensional metals and two-dimensional semiconductors," *Nature*, vol. 568, no. 7750, pp. 70–74, Apr. 2019, doi: 10.1038/s41586-019-1052-3.

[11] Y. S. Ang, H. Y. Yang, and L. K. Ang, "Universal Scaling Laws in Schottky Heterostructures Based on Two-Dimensional Materials," *Phys. Rev. Lett.*, vol. 121, no. 5, p. 056802, Aug. 2018, doi: 10.1103/PhysRevLett.121.056802.

[12] S. Banerjee, J. Luginsland, and P. Zhang, “A Two Dimensional Tunneling Resistance Transmission Line Model for Nanoscale Parallel Electrical Contacts,” *Sci Rep*, vol. 9, no. 14484, pp. 1–14, Oct. 2019, doi: 10.1038/s41598-019-50934-2.

[13] C. D. English, G. Shine, V. E. Dorgan, K. C. Saraswat, and E. Pop, “Improved Contacts to MoS2 Transistors by Ultra-High Vacuum Metal Deposition,” *Nano Lett.*, vol. 16, no. 6, pp. 3824–3830, Jun. 2016, doi: 10.1021/acs.nanolett.6b01309.

[14] K. K. H. Smithe, C. D. English, S. V. Suryavanshi, and E. Pop, “Intrinsic electrical transport and performance projections of synthetic monolayer MoS 2 devices,” *2D Mater.*, vol. 4, no. 1, p. 011009, Nov. 2016, doi: 10.1088/2053-1583/4/1/011009.

[15] N. Kaushik *et al.*, “Schottky barrier heights for Au and Pd contacts to MoS2,” *Appl. Phys. Lett.*, vol. 105, no. 11, p. 113505, Sep. 2014, doi: 10.1063/1.4895767.

[16] F. Pennec, D. Peyrou, D. Leray, P. Pons, R. Plana, and F. Courtade, “Impact of The Surface Roughness Description on the electrical contact resistance of ohmic switches under low actuation forces,” *IEEE Transactions on Components and Packaging Technologies*, vol. 2, no. 1, pp. 85–94, Jan. 2012.

[17] Z. A. Lamport *et al.*, “A simple and robust approach to reducing contact resistance in organic transistors,” *Nat Commun*, vol. 9, Dec. 2018, doi: 10.1038/s41467-018-07388-3.

[18] Y. Gao, L. Liu, W. Ta, and J. Song, “Effect of surfaces similarity on contact resistance of fractal rough surfaces under cyclic loading,” *AIP Advances*, vol. 8, no. 3, p. 035319, Mar. 2018, doi: 10.1063/1.5025073.

[19] P. Zhang, “Effects of Surface Roughness on Electrical Contact, RF Heating and Field Enhancement.,” *PhD thesis, the University of Michigan, Ann Arbor*, 2012, Available: http://deepblue.lib.umich.edu/handle/2027.42/95929.

[20] T. Liu *et al.*, “Crested two-dimensional transistors,” *Nat. Nanotechnol.*, vol. 14, no. 3, pp. 223–226, Mar. 2019, doi: 10.1038/s41565-019-0361-x.

[21] S.-J. Liang, W. Hu, A. Di Bartolomeo, S. Adam, and L. K. Ang, “A modified Schottky model for graphene-semiconductor (3D/2D) contact: A combined theoretical and experimental study,” in *2016 IEEE International Electron Devices Meeting (IEDM)*, Dec. 2016, p. 14.4.1-14.4.4, doi: 10.1109/IEDM.2016.7838416.

[22] Y. S. Ang and L. K. Ang, “Current-Temperature Scaling for a Schottky Interface with Nonparabolic Energy Dispersion,” *Phys. Rev. Applied*, vol. 6, no. 3, p. 034013, Sep. 2016, doi: 10.1103/PhysRevApplied.6.034013.

[23] Y. S. Ang, Y. Chen, C. Tan, and L. K. Ang, “Generalized High-Energy Thermionic Electron Injection at Graphene Interface,” *Phys. Rev. Applied*, vol. 12, no. 1, p. 014057, Jul. 2019, doi: 10.1103/PhysRevApplied.12.014057.

[24] Y. S. Ang, S.-J. Liang, and L. K. Ang, “Theoretical modeling of electron emission from graphene,” *MRS Bulletin*, vol. 42, no. 7, pp. 505–510, Jul. 2017, doi: 10.1557/mrs.2017.141.

[25] D. Sinha and J. U. Lee, “Ideal Graphene/Silicon Schottky Junction Diodes,” *Nano Lett.*, vol. 14, no. 8, pp. 4660–4664, Aug. 2014, doi: 10.1021/nl501735k.

[26] M. Sze and K. K. Ng, *Physics of Semiconductor Devices*. John Wiley & Sons, 2006.

[27] E. S. Kadantsev and P. Hawrylak, “Electronic structure of a single MoS2 monolayer,” *Solid State Communications*, vol. 152, no. 10, pp. 909–913, May 2012, doi: 10.1016/j.ssc.2012.02.005.

[28] P. Zhang and Y. Y. Lau, “An exact field solution of contact resistance and comparison with the transmission line model,” *Appl. Phys. Lett.*, vol. 104, no. 20, p. 204102, May 2014, doi: 10.1063/1.4878841.

[29] P. Zhang, D. M. H. Hung, and Y. Y. Lau, “Current flow in a 3-terminal thin film contact with dissimilar materials and general geometric aspect ratios,” *J. Phys. D: Appl. Phys.*, vol. 46, no. 6, p. 065502, Feb. 2013, doi: 10.1088/0022-3727/46/6/065502.

[30] “International Roadmap for Devices and Systems (IRDS^{TM}) 2017.” https://irds.ieee.org/editions/2017.

[31] H. Zhong *et al.*, “Interfacial Properties of Monolayer and Bilayer MoS_2 Contacts with Metals: Beyond the Energy Band Calculations,” *Scientific Reports*, vol. 6, p. 21786, Mar. 2016, doi: 10.1038/srep21786.

CHAPTER 6

INTERFACE ENGINEERING OF ELECTRICAL CONTACTS

This chapter is based on the manuscript under review for a journal publication, "Interface engineering of electrical contacts," by **S. Banerjee**, J. Luginsland, and P. Zhang [1].

6.1 Introduction

Engineering electrical contacts to achieve desired interface current transport is crucial for next generation electronics [2], [3]. Several efforts have been made to reduce the current crowding and improve the current transport in electrical contacts by making the proper choice for electrode thickness [4], doping, electrode material and its geometry [5] [6], [7], optimizing the current spreading layer [8] and the gate bias voltage [9]. The existing studies give no hint on the variation of current along the contact length and the importance of interface layer engineering to diminish the current crowding effects. The crowding is especially strong for contacts with low specific contact resistivity [10][11], [12]. Increasing specific contact resistivity tends to reduce current crowding; however, it increases the total contact resistance that may lead to increased Joule heating and degradation of the contact. Because of this tradeoff, it is particularly challenging to design electrical interfaces to reduce current crowding without decreasing the total current in the circuit.

Our previous studies (Chapters 3, 4, and 5) [12]–[14] showed that current and voltage distribution along the contact length greatly depend on the interfacial layer properties and geometry. In this chapter, we demonstrate how to precisely customize their profiles along the contact length by interface engineering. We characterize ohmic, Schottky [14], [15] and tunneling type [12], [16]–[18] electrical contacts. Our goal is to maximize the control over electrical contact operation and heat distribution by strategically varying the specific contact resistivity ρ_c along the contact length. We use modified two-dimensional transmission line model (TLM) [12], [13], where ρ_c depends upon the local voltage drop and contact current density. The spatial variation of ρ_c may be achieved by varying the doping, thickness, or shape of the contact layer, or by introducing impurities, such as, resistive contaminants, oxides, or foreign objects along the interface. Electrical properties of the engineered interfaces are investigated for various input voltage, contact dimension and geometry, and material properties. Solving the TLM equations self-consistently, we find spatial profiles of ρ_c that can reduce current crowding, increase current transfer length, improve current transport, steer and redistribute current in the contact area. Most importantly, we find that the severe current crowding in highly conductive ohmic contacts can be eliminated by introducing a thin tunneling layer between the contact members. If the tunneling layer is sufficiently thin and the contact length is large, the change in the total contact resistance is found to be insignificant.

The methods used here can be applied to characterize various contact geometries shown in Fig. 6.1. Controlled current and voltage distribution can be achieved via engineered spatially varying contact layer properties and geometry (Fig. 6.1) [3]. Note that, the transmission-line model, in general, underestimates the extent of the current crowding, which may be more accurately accounted for by the field solution approaches [9]–[11]. However, such simplified models have been used successfully to capture the basic scalings and physics for the characterization of mesoscale and nanoscale electrical contacts [12], [13], [19]–[22]. In this chapter, we analyze nanoscale copper (Cu) thin film contacts and Gold-MoS_2 contacts as examples. The concepts, approaches, and results should be important to the design of any circuits where electrical contacts are of concern, such as semiconductor devices [20], [23], integrated circuits [24], low-dimensional materials based electronics [2], [25]–[27], and all solid-state batteries [28].

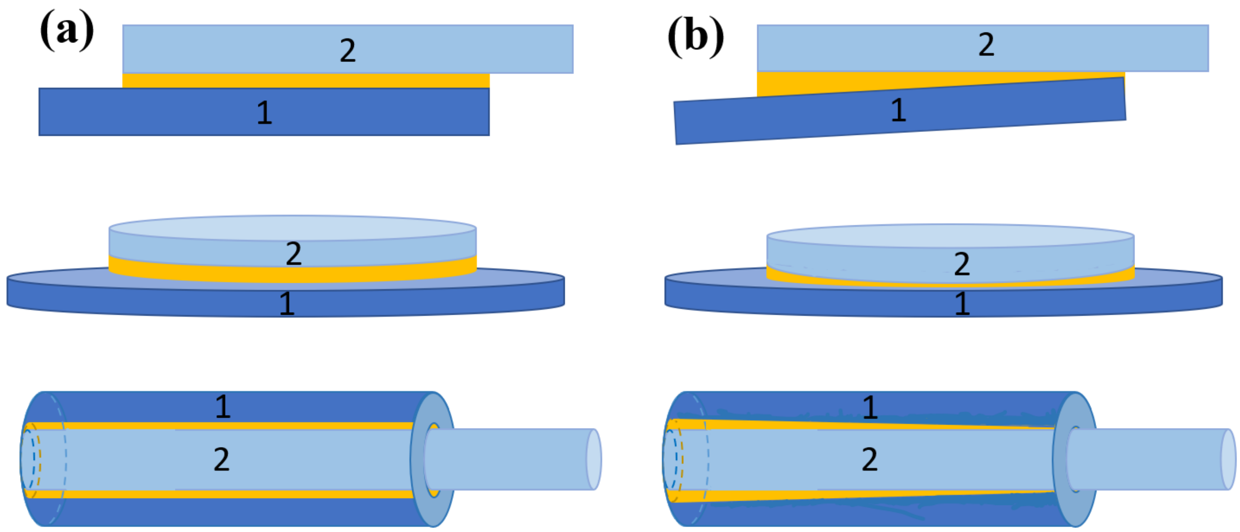

Figure 6.1 Electrical contact between contact member 1 and 2 for different electrode geometry. (a) Electrical contact with uniform contact interface, (b) electrical contact with a spatially varying engineered interfacial layer, which is used to control the voltage and current distribution.

6.2 The Model

The formulation is based on the modified transmission line model for Cartesian (Chapter 3) [12] and circular (Chapter 4) [13] contact structures, coupled with the improved thermionic emission current injection model for 2D materials [14], [15] (for 2D/3D Schottky contacts), or the self-consistent quantum model for one-dimensional MIM junctions (Chapter 2) [18], [29] (for tunneling type contacts). As shown in Fig. 6.2, the sheet resistance of the two contacting members is R_{sh1} and R_{sh2}, respectively. The spatially dependent specific interfacial resistivity (also termed specific contact resistivity) is $\rho_c(x)$ and $\rho_c(r)$ for the Cartesian and circular contacts, respectively. The goal is to engineer a spatial profile of $\rho_c(x)$ or $\rho_c(r)$ in order to suppress current crowding.

While the modified TLMs have been presented in Chapters 3 and 4 before [12], [13], the governing equations are given below for completeness.

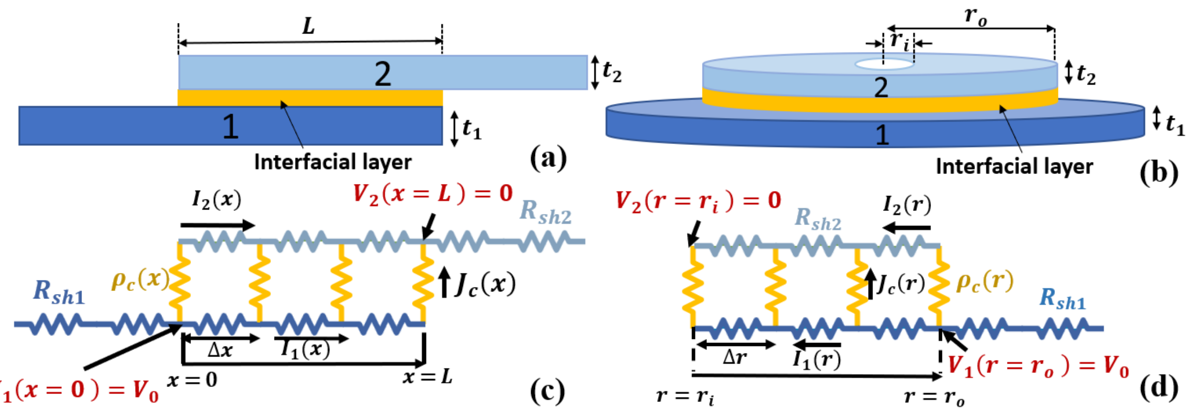

Figure 6.2 Electrical contact between two contacting members in (a) Cartesian, (b) circular geometry. (c), (d) its corresponding transmission line model. In (a) and (b), a thin interface layer (ohmic, Schottky, or tunneling type) is sandwiched between the two contacting members. The thicknesses of thin film 1 and 2 are t_1 and t_2, respectively.

For Cartesian electrical contacts in Fig. 6.2a, its TLM in Fig. 6.2c gives [12],

$$\frac{\partial I_1(x)}{\partial x} = -wJ_c(x), \frac{\partial V_1(x)}{\partial x} = -\frac{I_1(x)R_{sh1}}{w}, \frac{\partial I_2(x)}{\partial x} = wJ_c(x), \frac{\partial V_2(x)}{\partial x} = -\frac{I_2(x)R_{sh2}}{w}, \tag{6.1}$$

where $I_{1,2}(x)$ represents the current flowing at x through the lower or upper contact member respectively, and $V_{1,2}(x)$ is the local voltage at x along the lower or upper contact member, respectively, and w is the effective transverse dimension of the contacts, $J_c(x) = V_g(x)/\rho_c(x)$ and $V_g(x) = V_1(x) - V_2(x)$ are the local current density and the local voltage drop across the contact interface at x, respectively. Note that, from Eq. (1) $I_1(x) + I_2(x) = I_{tot} =$ constant, where I_{tot} is the total current in the circuit, to be determined from the boundary conditions,

$$V_1(x = 0) = V_o, I_2(x = 0) = 0, I_1(x = L) = 0, V_2(x = L) = 0\,, \tag{6.2}$$

where we assume the voltage of the upper contact member at $x = L$ is 0, and the externally applied voltage at $x = 0$ of the lower contact member is V_0. Note that $I_1(x = 0) = I_{tot}$, and $I_2(x = 0) = 0$. For the contact model in Fig. 6.2(b), the contact resistance is defined as,

$$R_c = \frac{V_1(0) - V_2(L)}{I_{tot}} = \frac{V_o}{I_{tot}}. \tag{6.3}$$

For circular (ring) electrical contacts shown in Fig. 6.2b with its TLM in Fig. 6.2d, we have [13],

$$\frac{\partial I_1(r)}{\partial r} = 2\pi r\, J_c(r), \frac{\partial V_1(r)}{\partial r} = \frac{I_1(r) R_{sh1}}{2\pi r}, \frac{\partial I_2(r)}{\partial r} = -\, 2\pi r\, J_c(r), \frac{\partial V_2(r)}{\partial r} = \frac{I_2(r) R_{sh2}}{2\pi r}, \tag{6.4}$$

where $I_{1,2}(r)$ represents the current flowing at r along the radial direction of thin films 1 and 2, respectively, and $V_{1,2}(r)$ is the local voltage at r along the radial direction of thin films 1 and 2, respectively. $J_c(r) = V_g(r)/\rho_c(r)$ and $V_g(r) = V_1(r) - V_2(r)$ are the local current density and the local voltage drop across the contact interface at r, respectively. From Eq. 6.4, $I_1(r) + I_2(r) = I_{tot} =$ constant, where I_{tot} is the total current in the circuit to be determined from the following boundary conditions,

$$V_1(r = r_o) = V_o, I_1(r = r_i) = 0, \; I_2(r = r_o) = 0, V_2(r = r_i) = 0, \tag{6.5}$$

where we assume the voltage of the upper contact member at $r = r_i$ is 0 and the external voltage V_0 is applied at $r = r_o$ to the lower contact member, r_o is the outer radius of thin film 2 and r_i is the inner radius of both the films. Note that $I_1(r = r_o) = I_{tot}$, $I_2(r = r_i) = I_{tot}$, and $I_{tot} = \int_{r_i}^{r_o} 2\pi r\, J_c(r)\, dr$. For the contact model in Fig. 6.1(c), the contact resistance is defined as,

$$R_c = \frac{V_1(r_o) - V_2(r_i)}{I_{tot}} = \frac{V_o}{I_{tot}}\,. \tag{6.6}$$

For ohmic contacts, $\rho_c(x)$ and $\rho_c(r)$ can be prescribed. For 2D-semiconductor/3D-metal Schottky contacts, the local contact current density $J_c(x)$ or $J_c(r)$ is calculated from the 2D thermionic emission model [14], [15] and for metal-insulator-metal (MIM) tunneling type contacts, it is calculated from the one-dimensional MIM quantum tunneling model including space charge effects (Chapter 2) [18], [29]. $\rho_c(x)$ and $\rho_c(r)$ are then determined from these contact current densities by $\rho_c = V_g/J_c$. The coupled equations are solved self-consistently, with more detailed descriptions in Chapters 3 and 4 [12] [13].

We first characterize both Cartesian and circular ohmic contacts with varying ρ_c along contact length or radius, respectively. We find varying $\rho_c(x)$ parabolically and $\rho_c(r)$ linearly can effectively reduce the current crowding effects in planar and circular ohmic contacts, respectively. Next, we analyze the 2D-semiconductor/3D-metal contacts to increase the current transfer length by varying the Schottky barrier height (SBH) along the contact length L. Finally, we introduce a thin (in sub-nanometer or nanometer) tunneling layer between the highly conductive contact members to reduce current crowding, without increasing the total contact resistance significantly.

6.3 Results and Discussion

We analyze Cartesian ohmic contacts in Fig. 6.3 and circular ohmic contacts in Fig. 6.4. The input voltage $V_o = 0.6$ V is the required industry standards according to the International Roadmap of Devices and Systems (IRDS) [30] for year 2030, which is given to contact member 1, at $x = 0$ for the planar structure and at $r = r_o$ for the circular structure. Upper contact members at $x = L$ (Fig. 6.2a, 6.2c) and $r = r_i$ (Fig. 6.2b, 6.2d) are grounded for the two structures under study. Thickness of both the contact members are assumed to be same, $t_1 = t_2 = 10$ nm. The spatial or radial variation of ρ_c can be realized by varying the doping or thickness or geometry of the contact layer, or by introducing impurities, such as, resistive contaminants, oxides, or foreign objects along the interface [12], [31]–[35]. In Figure 6.3, we explore the reduction of the severe current crowding (c.f. Fig. 6.3a, black dotted line) at the highly conductive planar (or Cartesian) Cu-Cu ohmic contacts by varying the interfacial layer resistivity parabolically along the contact length. For our calculations, we assume $\rho_c(x) = 18 \times 10^{-10} \left(\mathrm{B}\ \left(\frac{2x}{L} - 1\right)^2 + 0.01\right)\ \Omega\ \mathrm{cm}^2$ with the minimum at half of the contact length, where B is a constant. The sheet resistance of copper (Cu) is $R_{sh} = 18\ \Omega/\square$ [13], [36], where the unit of the sheet resistance $\Omega/\square$ means "ohm per square" [11], [20], [21]. Contact length $L = 100$ nm, and the width (transverse dimension) of the contact members $w = 10$ nm. Figure 6.3a shows that the profile of contact current density $J_c(x)$ strongly depends on B. The profiles of $J_c(x)$ can be explained by simple current transport theory in a circuit, where electric current flows through the least resistive path. When B is increased, the inhomogeneity of the contact current distribution decreases. At around $\mathrm{B} = 0.2$, the interfacial current becomes almost uniform along the contact length. The total contact resistance R_c as a function of B is plotted in Fig. 6.3b for different contact lengths. For all the contact lengths plotted here, R_c increases only slightly with B, e.g. for $L = 100$ nm, R_c is increased at most by 50% within the range of B. Hence, evidently, it is possible to eliminate current crowding effects and achieve uniform contact current distribution without sacrificing the total current in the circuit. In practical circuit design and fabrication where it might be difficult to control the shape of a parabola, one can use a step variation by just making the edges of a contact interface (of planar, similar contact members) more resistive than the rest of the contact area. The approach used here to minimize the current crowding effects can be extended to contacts with different electrode thickness, material, and geometry.

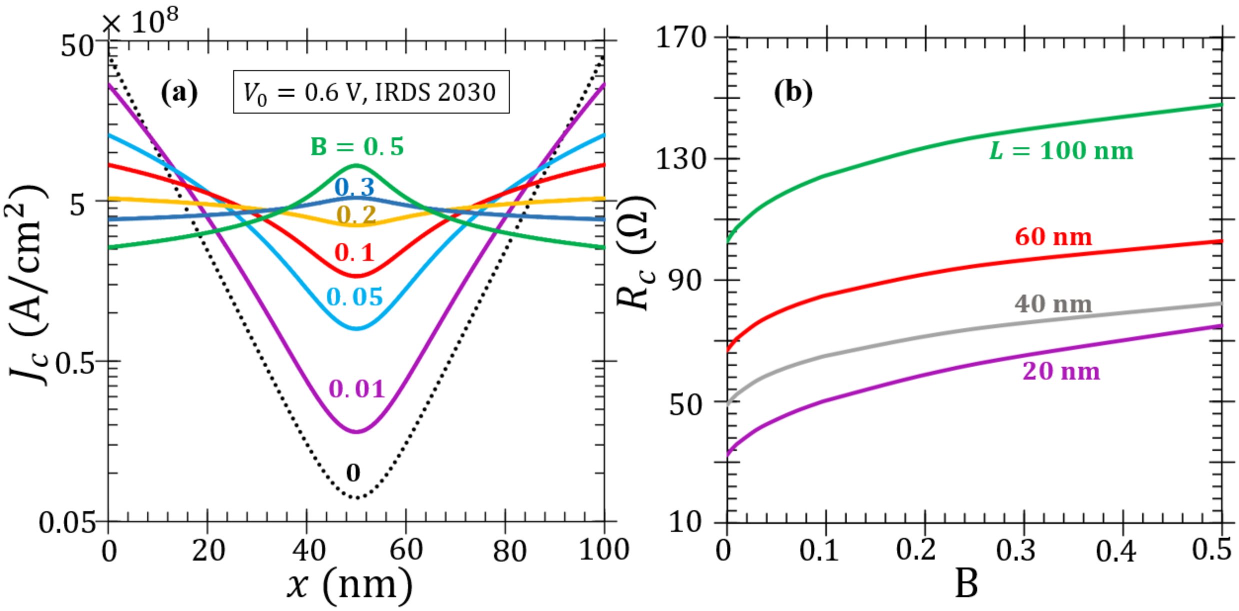

Figure 6.3 Engineered ohmic contact in Cartesian geometry (Fig. 6.2a) with specific contact resistivity $\rho_c(x) = 18 \times 10^{-10}\left(B\left(\frac{2x}{L} - 1\right)^2 + 0.01\right)$ Ω cm^2. (a) Contact current density $J_c(x)$ along the contact length for different values of B; (b) contact resistance as a function of B for different contact length L. The input voltages $V_0 = 0.6$ V is the required industry standards according to the International Roadmap of Devices and Systems (IRDS)[30] for year 2030. The thickness of both Cu contact members are 10 nm, with a resistivity of 18 μΩ cm [36], which gives sheet resistance $R_{sh1} = R_{sh2} = 18\ \Omega/\square$. Contact length $L = 100$ nm, and the width (transverse dimension) of the contact members $w =$ 10 nm.

In Fig. 6.4, we investigate the current transport for circular ohmic contacts with linearly varying specific contact resistivity along the contact radius. Note that linearly varying specific contact resistivity is found to strongly modify the current density profile for planar contacts [12]. Here, we assume radially varying $\rho_c(r) = 18 \times 10^{-10}(1 + \mathrm{A}r/r_o)\ \Omega\ \mathrm{cm}^2$, outer radius of the upper contact member (Fig. 6.2b) $r_o = 100$ nm, and the inner radius of both the contact members $r_i = 1$ nm. A is a linearization constant. The contact member 1 is assumed to be copper (Cu) with sheet resistance $R_{sh1} = 18\ \Omega/\square$ [13], [36].

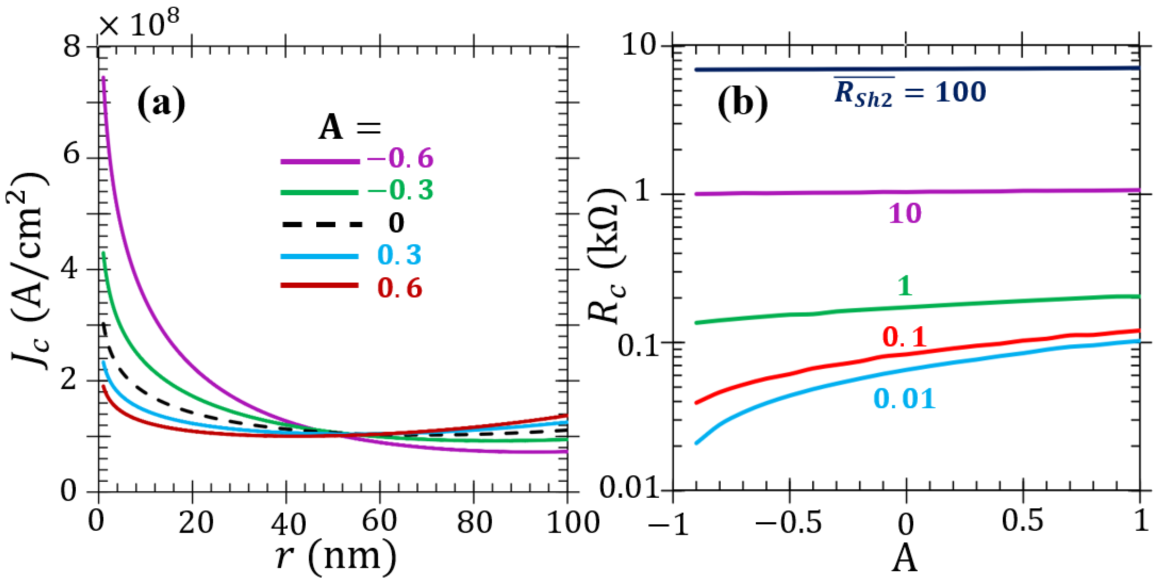

Figure 6.4 Ohmic contacts in circular geometry (Fig. 6.2b) with linearly varying specific contact resistivity. (a) Contact current density J_c along the contact length for different values of linear constant A. (b) Contact resistance as a function of A for different sheet resistance ratio $\overline{R_{sh2}}$. Here, we use $\rho_c(r) = 18 \times 10^{-10}(1 + Ar/r_o)\ \Omega\ \mathrm{cm}^2$. In (a) $\overline{R_{sh2}} = R_{sh2}/R_{sh1} = 1$. The input voltage $V_0 = 0.6$V is the required industry standards according to the International Roadmap of Devices and Systems (IRDS)[30] for year 2030. The contact member 1 is assumed to be copper (Cu) with sheet resistance $R_{sh1} = 18\ \Omega/\square$ [13], [36], outer radius of the upper contact member $r_o = 100$ nm, and the inner radius of both the contact members $r_i = 1$ nm.

As shown in Fig. 6.4a, linear variation of $\rho_c(r)$ can reduce the current crowding effects for circular contacts. In particular, current crowding at the inner edge reduces significantly when A is positive. Figure 6.4b shows that for circular contacts R_c increases with A rapidly for $\overline{R_{sh2}} < 1$ and remains almost constant when $R_{sh2} \gg R_{sh1}$. Therefore, one can get a desired interfacial current distribution profile without altering the overall contact resistance considerably. Hence, engineering the spatially varying interfacial contact resistivity can provide strategic thermal management of the integrated circuits and systems.

$$\phi_B\ (x) = 0.4(x/L)^2 - b(x/L) + 0.8\ \text{eV}$$

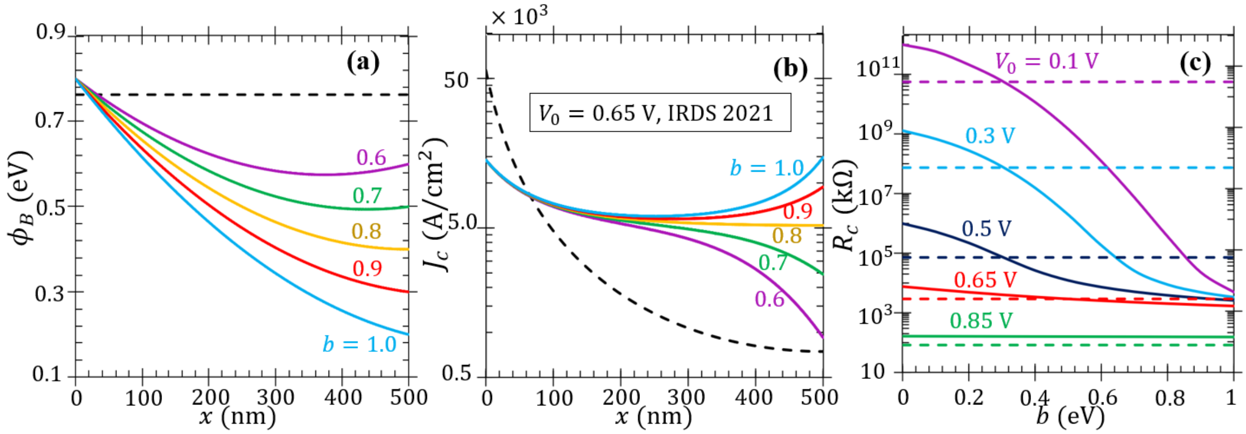

Figure 6.5 Engineered Schottky contacts in Cartesian geometry. (a) Schottky barrier height $\boldsymbol{\phi_B(x)}$, (b) the corresponding contact current density $\boldsymbol{J_c(x)}$ along the contact length for $\boldsymbol{MoS_2 - Au}$ contacts for different values of $\boldsymbol{b}$, and (c) contact resistance as a function of $\boldsymbol{b}$ for different input voltage $\boldsymbol{V_0}$. Dashed lines are for $\boldsymbol{MoS_2 - Au}$ contacts with uniform $\boldsymbol{\phi_B = 0.763}$ eV [37]. The Fermi level $\boldsymbol{\varepsilon_F = 0.077}$ eV [37], and carrier injection time $\boldsymbol{\tau = 0.1}$ ps. The bias voltage $\boldsymbol{V_0 = 0.65}$ in (b) is the required industry standards according to the International Roadmap of Devices and Systems (IRDS)[30] for year 2021. Here, $\boldsymbol{R_{sh1}(MoS_2) = 59171.6\ \Omega/\square}$, $\boldsymbol{R_{sh2}(Au) = 2.2\ \Omega/\square}$, $\boldsymbol{L = 500}$ nm and $\boldsymbol{T = 300}$ K.

Current crowding is an unavoidable consequence of geometrical confinement and resistivity mismatch at the 2D-semiconductor/3D-metal Schottky junctions, where the current transport between the semiconductor and the metal contact is concentrated at the front edge of the contact [38] [9], [14], [26], [39]–[41]. In Fig. 6.5, we study the engineering of such contacts by spatially varying the Schottky barrier height (SBH). We use the one-dimensional (1D) thermionic emission equation for 2D materials Eq. (5.2) [14], [15], coupled with the TLM equations, Eqs. (3.5) and (3.6) [12] to analyze such 2D/3D contacts. For 2D transition metal dichalcogenide (TMDC), such as atomically-thin MoS_2, the thermionic emission is governed by $J_{th}(V_g, T) = \frac{2e\Phi_{B0}k_BT}{\pi\tau\hbar^2 v_F^2}\left(1 + \frac{k_BT}{\Phi_{B0}}\right)\exp\left(-\frac{\Phi_{B0}-\varepsilon_F}{k_BT}\right)$, where $\Phi_{B0} = \phi_B + \varepsilon_F$ is the intrinsic Schottky barrier height (SBH), ε_F is the Fermi level, ϕ_B is the SBH, the Fermi velocity $v_F = 1.1 \times 10^6$ m/s for MoS_2, and $\tau \approx$

$(0.1 \sim 10)$ ps is the carrier injection time determined experimentally [42]. The local contact current density at any position x along the contact length is, $J_c(V_g, T) = J_{th}(V_g, T)\left[\exp\left(\frac{eV_g}{k_BT}\right) - 1\right]$.

We assume that the SBH is a function of x, $\phi_B\ (x) = 0.4(x/L)^2 - b(x/L) + 0.8$ eV, where b is a constant, as shown in Fig. 6.5a. The injection current density at the contact interface for different values of b is shown in Fig. 6.5b. It is found that the current crowding for uniform SBH (c. f. black dashed line in Fig. 6.5) can be reduced considerably by choosing the value of b (e.g. Fig. 6.5b, $b = 0.8$). The bias voltage $V_0 = 0.65$ V is the required industry standards according to the International Roadmap of Devices and Systems (IRDS)[30] for year 2021. Figure 6.5c shows the contact resistance as a function of b for different input voltage V_0. Dashed lines are for $\mathrm{MoS_2}-$ Au contacts with uniform $\phi_B = 0.763$ eV along the contact[37]. We see that the total contact resistance depends strongly on the parameter b and the input voltage V_0. The difference in contact resistance for engineered and uniform SBH is large for low bias voltages but becomes smaller for high bias voltages, for the chosen specific case here. Since the thermionic charge injection current for 2D materials sensitively depends on both the bias voltage and temperature [14], [15], [43], the engineered SBH profile requires a more detailed characterization for practical implementation.

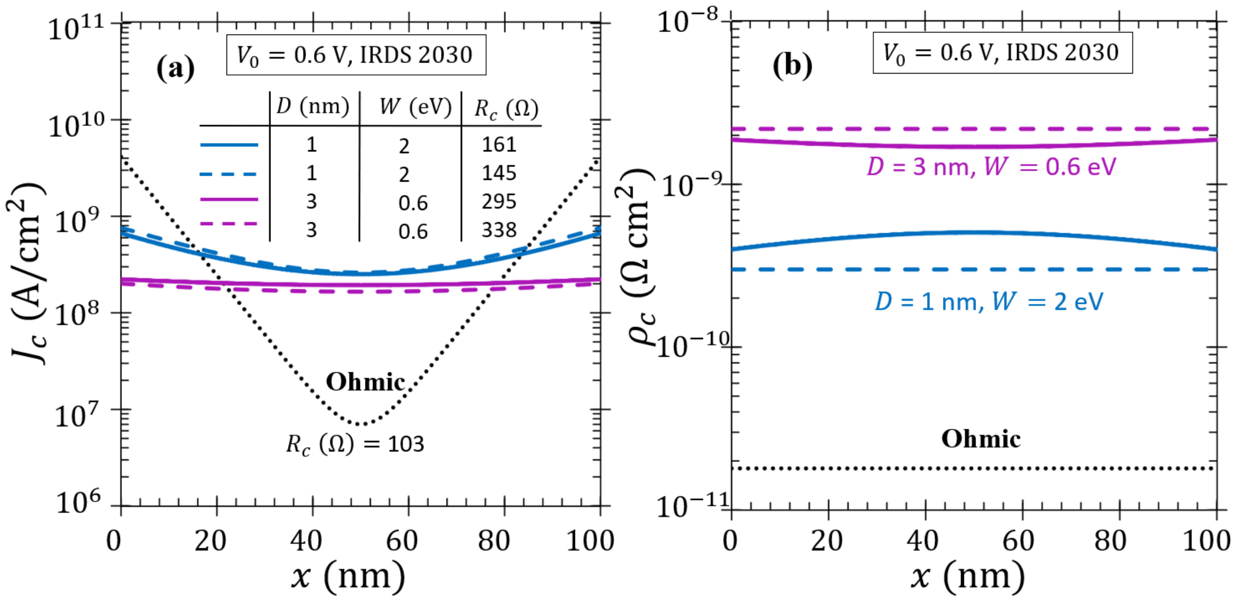

Figure 6.6 Tunneling type electrical contacts. (a) Contact current density $J_c(x)$, and (b) specific contact resistivity $\rho_c(x)$ along the contact length for Cartesian tunneling contacts. Solid lines are for self-consistent numerical calculations using Eqs. (3.5) and (3.6), and MIM quantum tunneling formulations (Chapter 2) [18], [29], for different values of gap distance D and work function of contact members W. Sheet resistance of both the contact members is assumed to be $R_{sh1} = R_{sh2} = 18\ \Omega/\square$. Dashed lines are calculated analytically with constant ρ_c calculated using $V_g = V_0$ in the 1D MIM tunneling model. Black dotted lines are for an ohmic contact with $\rho_c = 1.8 \times 10^{-11} \Omega\ \mathrm{cm}^2$, analytically calculated from the TLM equations. R_c is the total contact resistance.

Next, we investigate the reduction of current crowding for a highly conductive ($\rho_c \sim 10^{-11} \Omega\ cm^2$) ohmic contacts by tunneling engineering. We introduce a thin insulating layer of uniform thickness along the contact length between the contact members. Current transport in the contact region is no longer ohmic and is governed by the quantum tunneling phenomenon [16]–[18], [29]. We solve Eqs. (3.5) and (3.6) along with the metal-insulator-metal tunneling junction equation (Chapter 2) [18], [29]. The local contact current density $J_c(x)$ at any location x from contact member 1 to contact member 2 is calculated based on the coupled 1D Schrödinger-Poisson solutions in the MIM junction [18], [29]. Our quantum model of the junction (Chapter 2) includes emissions from both cathode (contacting member 2) and anode (contacting member 1), the effects of image charge potential [18], space charge, and exchange correlation potentials [44]. For given values of the work function of the two contact members $W_{1,2}$, electron affinity X, thickness D, and relative permittivity ϵ_r of the insulator layer, the local contact current density $J_c(x)$ can be calculated from this 1D quantum model for an input of the contact voltage drop $V_g(x)$ at any location x [18], [29]. The calculation of this $J_c(x)$- $V_g(x)$ relation is coupled with TLM, Eqs. (3.5), (3.6), and is solved self-consistently.

We consider nanometer and sub-nanometer scale tunneling layers in Fig. 6.6 and Fig. 6.7, respectively. The current fabrication technology can manufacture nodes as small as 3 nm [45], [46]. The International Roadmap of Devices and Systems (IRDS) [30] predicts that 1.0 nm nodes may be implemented tentatively within few years, and the scale is expected to go down even further, in sub-nanometers. Figure 6.6 shows the contact current density $J_c(x)$, and the specific contact resistivity $\rho_c(x)$ along the contact length for Cartesian contacts. For these calculations, the contact length is assumed to be 100 nm. Width and thickness of both the contact members are 10 nm. Solid lines are for self-consistent numerical calculations for the tunneling type contacts, using Eqs. (3.5), (3.6), and MIM quantum tunneling formulations (Chapter 2) [18], [29], for different values of gap distance (insulator layer thickness) D and work function of contact members W. Dashed lines are for analytical calculations (See Eq. (3.8) of Chapter 3) of tunneling contacts with constant ρ_c obtained using $V_g = V_0$ in the 1D MIM tunneling model. Sheet resistance of both the contact members is assumed to be $R_{sh1} = R_{sh2} = 18\ \Omega/\square$. We solved two cases, i) for $D = 1$ nm and $W_1 = W_2 = 2$ eV, and ii) for $D = 3$ nm and $W_1 = W_2 = 0.6$ eV. The interfacial layer is assumed to be vacuum (relative permittivity ϵ_r = 1.0 and electron affinity $X = 0$ eV). Black dotted lines are for an ohmic contact, calculated from Eq. (3.8) with specific contact resistivity $\rho_c = 1.8 \times 10^{-11} \Omega\ cm^2$, and sheet resistance ratio $R_{sh1}/R_{sh2} = 1$. We used 0.6 V as the input voltage, which is the required industry standards according to the International Roadmap of Devices and Systems (IRDS)[30] for year 2030.

It is clear that the interfacial current is much more evenly distributed for the contacts with a tunneling layer. The current crowding decreases significantly when the gap distance between two contact members is increased. The specific contact resistivity $\rho_c(x)$ along the contact length, plotted in Figs. 6.6b, is about 2 orders of magnitude higher for tunneling contacts for the two cases considered. However, the total contact resistance, shown in the table in Fig. 6.6a, is still within the same order of the ohmic contact. This is because the total current in the circuit (i.e. area under the curves in Fig. 6.6a) does not decrease significantly.

Similar calculations are done for Cu-vacuum-Cu contacts in Fig. 6.7 with a smaller gap distance (in sub-nanometer). The work function of Cu thin films is $W_1 = W_2 = 4.56$ eV [36]. For these calculations, the thickness of both Cu contact members are 10 nm, with a resistivity of 18 μΩ cm [36], which gives sheet resistance $\mathrm{R_{sh1}} = \mathrm{R_{sh2}} = 18\ \Omega/\square$. Contact length $L = 100$ nm, and width $w = 10$ nm, The interfacial layer is assumed to be vacuum (relative permittivity ϵ_r = 1.0 and electron affinity $X = 0$ eV).

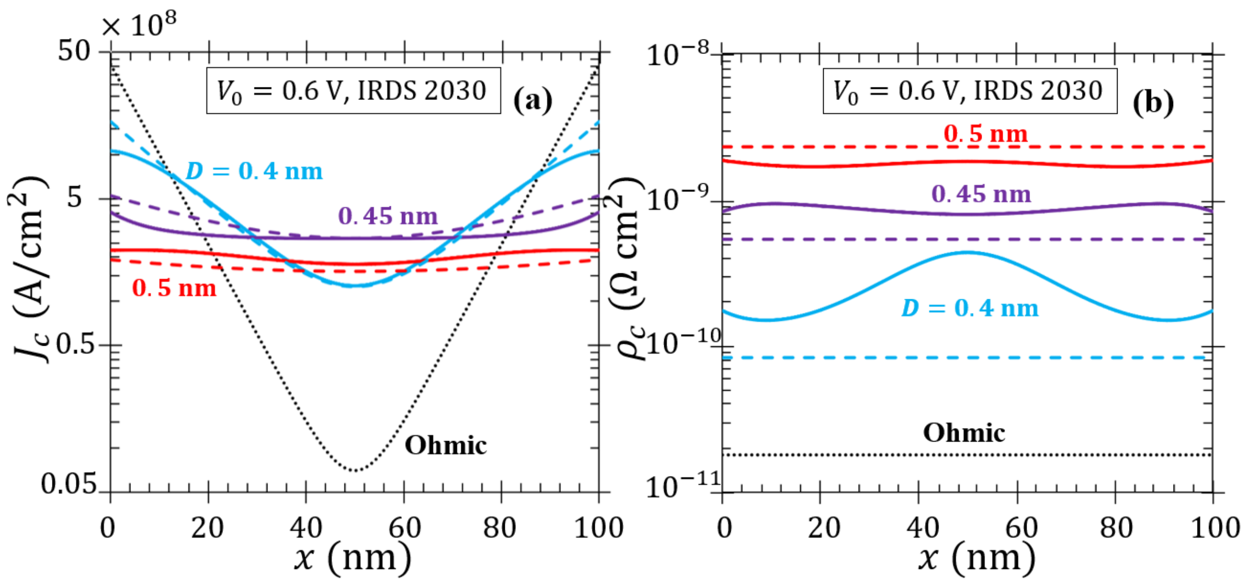

Figure 6.7 Tunneling type electrical contacts. (a) Contact current density $J_c(x)$, and (b) specific contact resistivity $\rho_c(x)$ along the contact length for Cartesian Cu-vacuum-Cu tunneling contacts. Solid lines are for self-consistent numerical calculations using Eqs. (3.5) and (3.6), and MIM quantum tunneling formulations (Chapter 2) [18], [29], for different values of gap distance *D*. Dashed lines are calculated analytically with constant ρ_c calculated using $V_g = V_0$ in the 1D MIM tunneling model. Black dotted lines are for an ohmic contact with $\rho_c = 1.8 \times 10^{-11} \Omega\, cm^2$, analytically calculated from the TLM equations.

Figure 6.7 shows similar trends to those in Fig. 6.6. The current crowding decreases significantly when D increases. Although, $\rho_c(x)$ (Fig. 6.7b) is orders of magnitude higher for tunneling contacts, the total contact resistance, plotted in Fig. 6.8a (crossed symbols) is still within the same order of the ohmic contact. Therefore, compared to a perfect ohmic contact with very small $\rho_c(x)$, tunneling type contacts with ultrathin insulator layer may help to achieve better contact current distribution and thermal management. Note that if the gap distance is increased for contacting members with high work function, then the junction will become highly resistive and the total current transport will be reduced severely.

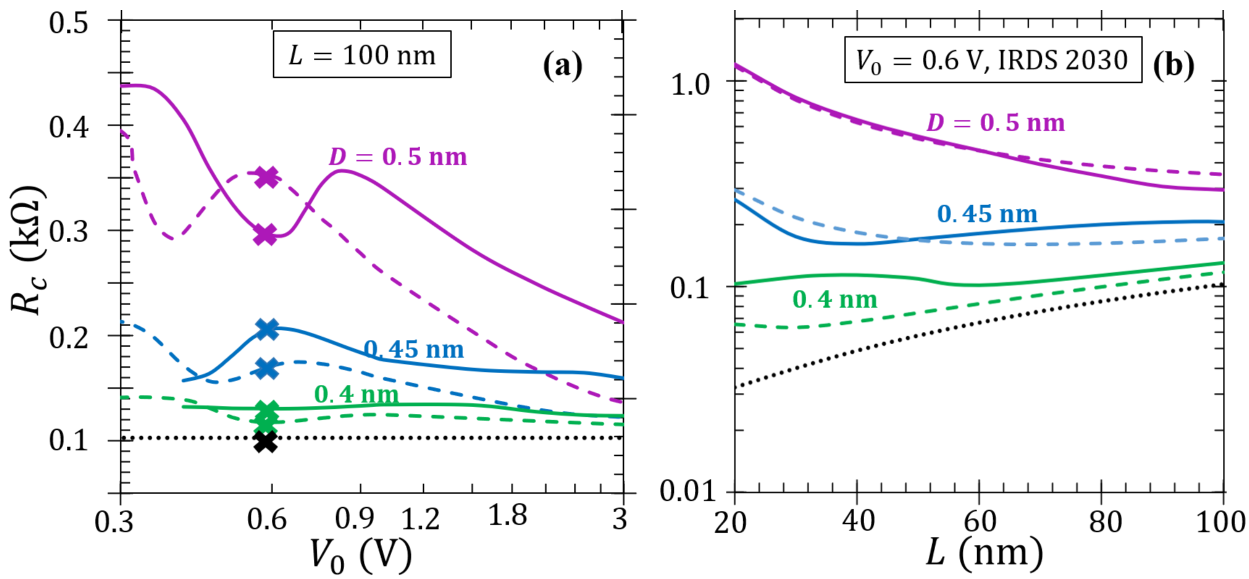

Figure 6.8 Contact resistance as a function of (a) input voltage V_0, and (b) contact length L for Cartesian Cu-vacuum-Cu tunneling contacts. Solid lines are self-consistent numerical calculations using Eqs. (3.5), (3.6), and MIM quantum tunneling formulations (Chapter 2) [18], [29], for different values of gap distance D. Dashed lines are calculated analytically with constant ρ_c calculated using $V_g = V_0$ in the 1D MIM tunneling model. Black dotted lines are for an ohmic contact with $\rho_c = 1.8 \times 10^{-11} \Omega\ cm^2$, analytically calculated the TLM equations. Crossed points in (a) are for the four cases shown in Fig. 6.7.

Figure 6.8 shows the tunneling contact resistance as functions of input voltage V_0 and contact length L. For low voltages, the difference between the contact resistance for the ohmic contact and the corresponding tunneling contact is prominent. However, as voltage increases, the difference becomes smaller, which is caused by the saturation of the tunneling current in metal-insulator-metal due to space-charge effects [18], [29]. As shown in Fig. 6.8b, as contact length increases, the increase of total contact resistance due to the tunneling layer becomes smaller. Thus, our proposed method reducing current crowding with a tunneling layer would become more effective for longer electrical contacts.

6.4 Concluding Remarks

In summary, we have proposed methods to effectively control current distribution and contact resistance in nanoscale electrical contacts. We have used the two dimensional TLM [12], [13] for ohmic contacts, and TLM coupled with the thermionic injection model [14], [15] for Schottky contacts and the quantum self-consistent model [18], [29] for tunneling type contacts. Our study shows that severe current crowding in highly conductive electrical contacts can be effectively reduced by spatially varying the contact layer properties and geometry, or by introducing a thin nanometer or sub-nanometer scale insulator layer between the contacting members. This theoretical study also provides insights for strategic current steering and redistribution at the contact interface, which can aid in better thermal management of the overall circuit. The local heating induced effects, such as thermal hotspots [47] and aggravation of electromigration [48], can be mitigated by manipulating the specific contact resistivity along the contact length.

It is worthwhile to note that the effects of the transverse dimension, possible charge trapping inside the contact layer, reactive elements and their effects on the time-dependent dynamics are ignored in the present study. Moreover, the transmission line model [12] cannot fully capture the current crowding and the fringing fields near the contact corners [9], [11], [21]. In future, field solution methods [11], [21], [49] may be used to have more accurate evaluation of these effects as well as the impact of finite thickness of the contact members and the interfacial layer.

REFERENCES

REFERENCES

[1] S. Banerjee, J. Luginsland, and P. Zhang, “Interface Engineering of Electrical Contacts,” *manuscript under review*, 2021.

[2] L.-M. Peng, “A new stage for flexible nanotube devices,” *Nat Electron*, vol. 1, no. 3, pp. 158–159, Mar. 2018, doi: 10.1038/s41928-018-0045-9.

[3] P. Zhang, S. Banerjee, and J. Luginsland, “Tunneling Electrical Contacts,” Patent US 10,755,975 B2, Aug. 25, 2020.

[4] C.-K. Wang, T.-H. Chiang, Y.-Z. Chiou, and S.-P. Chang, “Reducing the Current Crowding Effect on Nitride-Based Light-Emitting Diodes Using Modulated P-Extension Electrode Thickness,” *Jpn. J. Appl. Phys.*, vol. 52, no. 1S, p. 01AG05, Jan. 2013, doi: 10.7567/JJAP.52.01AG05.

[5] G. Kim, J. H. Kim, E. Park, and B.-G. Park, “Reduction of Current Crowding in InGaN-based Blue Light-Emitting Diodes by Modifying Metal Contact Geometry,” *JOURNAL OF SEMICONDUCTOR TECHNOLOGY AND SCIENCE*, Oct. 2014. https://www.dbpia.co.kr/Journal/articleDetail?nodeId=NODE02513912.

[6] N. Shamir and D. Ritter, “Reducing the current crowding effect in bipolar transistors by tunnel diode emitter design,” *Solid-State Electronics*, vol. 47, no. 1, pp. 127–130, Jan. 2003, doi: 10.1016/S0038-1101(02)00313-1.

[7] S.-S. Chee *et al.*, “Lowering the Schottky Barrier Height by Graphene/Ag Electrodes for High-Mobility MoS2 Field-Effect Transistors,” *Advanced Materials*, vol. 31, no. 2, p. 1804422, 2019, doi: https://doi.org/10.1002/adma.201804422.

[8] Y. Zhang, M. Sun, D. Piedra, J. Hennig, A. Dadgar, and T. Palacios, “Reduction of on-resistance and current crowding in quasi-vertical GaN power diodes,” *Appl. Phys. Lett.*, vol. 111, no. 16, p. 163506, Oct. 2017, doi: 10.1063/1.4989599.

[9] Q. Wang, X. Tao, L. Yang, and Y. Gu, “Current crowding in two-dimensional black-phosphorus field-effect transistors,” *Appl. Phys. Lett.*, vol. 108, no. 10, p. 103109, Mar. 2016, doi: 10.1063/1.4943655.

[10] P. Zhang, Y. Y. Lau, and R. S. Timsit, “On the Spreading Resistance of Thin-Film Contacts,” *IEEE Transactions on Electron Devices*, vol. 59, no. 7, pp. 1936–1940, Jul. 2012, doi: 10.1109/TED.2012.2195317.

[11] P. Zhang, Y. Y. Lau, and R. M. Gilgenbach, “Analysis of current crowding in thin film contacts from exact field solution,” *J. Phys. D: Appl. Phys.*, vol. 48, no. 47, p. 475501, 2015, doi: 10.1088/0022-3727/48/47/475501.

[12] S. Banerjee, J. Luginsland, and P. Zhang, “A Two Dimensional Tunneling Resistance Transmission Line Model for Nanoscale Parallel Electrical Contacts,” *Sci Rep*, vol. 9, no. 14484, pp. 1–14, Oct. 2019, doi: 10.1038/s41598-019-50934-2.

[13] S. Banerjee, P. Y. Wong, and P. Zhang, “Contact resistance and current crowding in tunneling type circular nano-contacts,” *J. Phys. D: Appl. Phys.*, vol. 53, no. 35, p. 355301, Jun. 2020, doi: 10.1088/1361-6463/ab8fe0.

[14] S. Banerjee, L. Cao, Y. S. Ang, L. K. Ang, and P. Zhang, “Reducing Contact Resistance in Two-Dimensional-Material-Based Electrical Contacts by Roughness Engineering,” *Phys. Rev. Applied*, vol. 13, no. 6, p. 064021, Jun. 2020, doi: 10.1103/PhysRevApplied.13.064021.

[15] Y. S. Ang, H. Y. Yang, and L. K. Ang, “Universal Scaling Laws in Schottky Heterostructures Based on Two-Dimensional Materials,” *Phys. Rev. Lett.*, vol. 121, no. 5, p. 056802, Aug. 2018, doi: 10.1103/PhysRevLett.121.056802.

[16] J. G. Simmons, “Generalized Formula for the Electric Tunnel Effect between Similar Electrodes Separated by a Thin Insulating Film,” *Journal of Applied Physics*, vol. 34, no. 6, pp. 1793–1803, Jun. 1963, doi: 10.1063/1.1702682.

[17] J. G. Simmons, “Electric Tunnel Effect between Dissimilar Electrodes Separated by a Thin Insulating Film,” *Journal of Applied Physics*, vol. 34, no. 9, pp. 2581–2590, Sep. 1963, doi: 10.1063/1.1729774.

[18] P. Zhang, “Scaling for quantum tunneling current in nano- and subnano-scale plasmonic junctions,” *Scientific Reports*, vol. 5, p. 9826, May 2015, doi: 10.1038/srep09826.

[19] H. Murrmann and D. Widmann, “Current crowding on metal contacts to planar devices,” *IEEE Transactions on Electron Devices*, vol. 16, no. 12, pp. 1022–1024, Dec. 1969, doi: 10.1109/T-ED.1969.16904.

[20] D. K. Schroder, *Semiconductor Material and Device Characterization*, 2nd Edition edition. New York: Wiley-Blackwell, 1998.

[21] P. Zhang and Y. Y. Lau, “An exact field solution of contact resistance and comparison with the transmission line model,” *Appl. Phys. Lett.*, vol. 104, no. 20, p. 204102, May 2014, doi: 10.1063/1.4878841.

[22] N. Chiodarelli *et al.*, “Measuring the electrical resistivity and contact resistance of vertical carbon nanotube bundles for application as interconnects,” *Nanotechnology*, vol. 22, no. 8, p. 085302, Feb. 2011, doi: 10.1088/0957-4484/22/8/085302.

[23] D. K. Schroder and D. L. Meier, “Solar cell contact resistance—A review,” *IEEE Transactions on Electron Devices*, vol. 31, no. 5, pp. 637–647, May 1984, doi: 10.1109/T-ED.1984.21583.

[24] K. N. Tu, Y. Liu, and M. Li, "Effect of Joule heating and current crowding on electromigration in mobile technology," *Applied Physics Reviews*, vol. 4, no. 1, p. 011101, Jan. 2017, doi: 10.1063/1.4974168.

[25] J. Tang *et al.*, "Flexible CMOS integrated circuits based on carbon nanotubes with sub-10 ns stage delays," *Nature Electronics*, vol. 1, no. 3, pp. 191–196, Mar. 2018, doi: 10.1038/s41928-018-0038-8.

[26] H. Yuan *et al.*, "Field effects of current crowding in metal-MoS2 contacts," *Appl. Phys. Lett.*, vol. 108, no. 10, p. 103505, Mar. 2016, doi: 10.1063/1.4942409.

[27] A. D. Franklin, D. B. Farmer, and W. Haensch, "Defining and Overcoming the Contact Resistance Challenge in Scaled Carbon Nanotube Transistors," *ACS Nano*, vol. 8, no. 7, pp. 7333–7339, Jul. 2014, doi: 10.1021/nn5024363.

[28] M. W. Swift and Y. Qi, "First-Principles Prediction of Potentials and Space-Charge Layers in All-Solid-State Batteries," *Phys. Rev. Lett.*, vol. 122, no. 16, p. 167701, Apr. 2019, doi: 10.1103/PhysRevLett.122.167701.

[29] S. Banerjee and P. Zhang, "A generalized self-consistent model for quantum tunneling current in dissimilar metal-insulator-metal junction," *AIP Advances*, vol. 9, no. 8, p. 085302, Aug. 2019, doi: 10.1063/1.5116204.

[30] "International Roadmap for Devices and Systems (IRDS^{TM}) 2017." https://irds.ieee.org/editions/2017.

[31] J. G. J. Chern and W. G. Oldham, "Determining specific contact resistivity from contact end resistance measurements," *IEEE Electron Device Letters*, vol. 5, no. 5, pp. 178–180, May 1984, doi: 10.1109/EDL.1984.25875.

[32] K. K. Ng and R. Liu, "On the calculation of specific contact resistivity on," *IEEE Transactions on Electron Devices*, vol. 37, no. 6, pp. 1535–1537, Jun. 1990, doi: 10.1109/16.106252.

[33] S. Gupta, P. Paramahans Manik, R. Kesh Mishra, A. Nainani, M. C. Abraham, and S. Lodha, "Contact resistivity reduction through interfacial layer doping in metal-interfacial layer-semiconductor contacts," *Journal of Applied Physics*, vol. 113, no. 23, p. 234505, Jun. 2013, doi: 10.1063/1.4811340.

[34] F. A. Chaves, D. Jiménez, A. W. Cummings, and S. Roche, "Physical model of the contact resistivity of metal-graphene junctions," *Journal of Applied Physics*, vol. 115, no. 16, p. 164513, Apr. 2014, doi: 10.1063/1.4874181.

[35] G. Shine and K. C. Saraswat, "Limits of specific contact resistivity to Si, Ge and III-V semiconductors using interfacial layers," in *2013 International Conference on Simulation of Semiconductor Processes and Devices (SISPAD)*, Sep. 2013, pp. 69–72, doi: 10.1109/SISPAD.2013.6650576.

[36] E. Schmiedl, P. Wissmann, and H.-U. Finzel, “The Electrical Resistivity of Ultra-Thin Copper Films,” *Zeitschrift für Naturforschung A*, vol. 63, no. 10–11, pp. 739–744, 2014, doi: 10.1515/zna-2008-10-1118.

[37] H. Zhong *et al.*, “Interfacial Properties of Monolayer and Bilayer MoS_2 Contacts with Metals: Beyond the Energy Band Calculations,” *Scientific Reports*, vol. 6, p. 21786, Mar. 2016, doi: 10.1038/srep21786.

[38] P. Karnatak, T. P. Sai, S. Goswami, S. Ghatak, S. Kaushal, and A. Ghosh, “Current crowding mediated large contact noise in graphene field-effect transistors,” *Nature Communications*, vol. 7, no. 1, Art. no. 1, Dec. 2016, doi: 10.1038/ncomms13703.

[39] K. Nagashio, T. Nishimura, K. Kita, and A. Toriumi, “Contact resistivity and current flow path at metal/graphene contact,” *Applied Physics Letters*, vol. 97, no. 14, p. 143514, Oct. 2010, doi: 10.1063/1.3491804.

[40] E. P. Vandamme and L. K. J. Vandamme, “Current crowding and its effect on 1/f noise and third harmonic distortion – a case study for quality assessment of resistors,” *Microelectronics Reliability*, vol. 40, no. 11, pp. 1847–1853, Nov. 2000, doi: 10.1016/S0026-2714(00)00091-3.

[41] K. L. Grosse, M.-H. Bae, F. Lian, E. Pop, and W. P. King, “Nanoscale Joule heating, Peltier cooling and current crowding at graphene–metal contacts,” *Nature Nanotechnology*, vol. 6, no. 5, Art. no. 5, May 2011, doi: 10.1038/nnano.2011.39.

[42] D. Sinha and J. U. Lee, “Ideal Graphene/Silicon Schottky Junction Diodes,” *Nano Lett.*, vol. 14, no. 8, pp. 4660–4664, Aug. 2014, doi: 10.1021/nl501735k.

[43] M. Javadi, A. Noroozi, and Y. Abdi, “Kinetics of Charge Carriers across a Graphene-Silicon Schottky Junction,” *Phys. Rev. Applied*, vol. 14, no. 6, p. 064048, Dec. 2020, doi: 10.1103/PhysRevApplied.14.064048.

[44] J. P. Perdew and Y. Wang, “Accurate and simple analytic representation of the electron-gas correlation energy,” *Phys. Rev. B*, vol. 45, no. 23, pp. 13244–13249, Jun. 1992, doi: 10.1103/PhysRevB.45.13244.

[45] “Making Chips At 3nm And Beyond,” *Semiconductor Engineering*, Apr. 16, 2020. https://semiengineering.com/making-chips-at-3nm-and-beyond/.

[46] “TSMC Details 3nm Process Technology: Full Node Scaling for 2H22 Volume Production.” https://www.anandtech.com/show/16024/tsmc-details-3nm-process-technology-details-full-node-scaling-for-2h22.

[47] X. Zhao, M. R. Scheuermann, and S. K. Lim, “Analysis and Modeling of DC Current Crowding for TSV-Based 3-D Connections and Power Integrity,” *IEEE Transactions on Components, Packaging and Manufacturing Technology*, vol. 4, no. 1, pp. 123–133, Jan. 2014, doi: 10.1109/TCPMT.2013.2276779.

[48] J. S. Huang, E. C. C. Yeh, Z. B. Zhang, and K. N. Tu, “The effect of contact resistance on current crowding and electromigration in ULSI multi-level interconnects,” *Materials Chemistry and Physics*, vol. 77, no. 2, pp. 377–383, Jan. 2003, doi: 10.1016/S0254-0584(02)00018-4.

[49] P. Zhang, D. M. H. Hung, and Y. Y. Lau, “Current flow in a 3-terminal thin film contact with dissimilar materials and general geometric aspect ratios,” *J. Phys. D: Appl. Phys.*, vol. 46, no. 6, p. 065502, Feb. 2013, doi: 10.1088/0022-3727/46/6/065502.

CHAPTER 7

CONCLUSION AND SUGGESTED FUTURE WORK

This thesis studies the current transport in nano-scale electrical junctions, characterizes the scaling of contact resistance, and provides better understanding of the underlying physics in nanoscale electrical contacts. This theoretical work also offers insights on the design and engineering of nanocontacts to reduce contact resistance and improve current transport.

7.1 On Metal-Insulator-Metal Tunneling Junctions

A self-consistent model has been developed to calculate tunneling current density in nano- and subnano-meter metal-insulator-metal (MIM) junctions with dissimilar metal electrodes [1]. The model is an extension of Zhang's work [2] on similar MIM junction. Quantum mechanical analysis has been done to include the effects of exchange correlation potential and space charge potential, by solving the coupled Schrodinger equation and Poisson equation self consistently. The current in dissimilar MIM is found to be polarity dependent. The forward (lower work function metal is positively biased) and reverse (lower work function metal is negatively biased) characteristics cross over at higher voltages. The influence of the work function of the two metal electrodes, thickness and relative permittivity of the insulator layer on the reverse and forward bias J-V curves, have been examined in detail in various regimes from direct tunneling, field emission, to space charge limited regime. It is found that the work function difference between the two electrodes influences the asymmetry of J-V characteristics more profoundly than their individual work functions. The asymmetry increases with increasing insulator layer thickness and relative permittivity.

Future works on the metal-insulator-metal tunneling junctions may include effects of electrode geometry. The present model is developed for Cartesian structure. In future, similar formulation may be done for the cylindrical structure as well. Our model is based on the assumption that the insulator layer is ideal, uniform and pristine. However, in real devices that may not be the case. There may be possible charge trapping inside the insulator film. In order to have a more accurate prediction of tunneling current density, the insulator layer imperfections need to be taken into account. In the future, frequency dependence of the tunneling junction may also be studied. Comparison of the theory and modelling with experiments may also be done. The application of the proposed model is widespread. Although developed for DC condition, it is applicable to nanojunctions operating up to Near Infrared frequency, since the transit time for electron tunneling through a barrier of nm-scale thickness is typically less than 1 fs [3]–[6]. Therefore, our model may be used to study the effects of tunneling resistance in several nanoscale electrical structures with time-varying excitations. For example, in split-ring resonator arrays, one may include tunneling conductivity in the nanogap to investigate the tunneling induced changes in the frequency response and absorption behavior. Our quantum self-consistent model can also be applied to characterize the rectification behavior of THz induced scanning tunneling microscopes (THz-STMs). The current profiles at STM tip-vacuum-sample junction can be studied for different THz peak fields, metal tips, sample metals and tip heights, and the basic scaling of the time dependent electron dynamics can be obtained.

7.2 On Current Distribution and Contact Resistance

The standard transmission line model (TLM) has been modified to include the effects of spatially varying specific contact resistivity ρ_c along the contact length. The current distribution and contact resistance in ohmic, tunneling and two-dimensional (2D) material-based Schottky contacts have been studied for a large parameter space. Self-consistent solutions have been obtained from the *two dimensional* TLM [7], [8] for ohmic contacts, and TLM coupled with the thermionic injection model [9], [10] for Schottky contacts and with the quantum self-consistent model [1], [2] for tunneling type contacts. Simple analytical solutions have been derived for the special case of uniform specific contact resistivity. Both Cartesian [7] and circular (or annular) [8] contacts are analyzed. It is found that the current and voltage distribution along the contacts and their overall contact resistance depend greatly on the input voltage, contact geometry, and material properties. For highly conductive ohmic contacts, the current distribution along the contact length is strongly nonhomogeneous [7], [8]. For tunneling contacts, the existing one-dimensional (1D) tunneling junction models become less reliable when the tunneling layer thickness becomes smaller or the applied voltage becomes larger. In these regimes, the proposed self-consistent model may provide a more accurate evaluation of the parallel tunneling contacts. On the other hand, a thorough study on the contact resistance of the novel 2D-material-based Schottky contacts showed that the junction characteristics transition from Schottky to ohmic regime when the input voltage (potential) is around the Schottky barrier height. We have also found that interface roughness can significantly reduce the electrical contact resistance for 2D material based contacts [9]. The results for ohmic contact are verified with finite element method (FEM) based simulations, and the 2D-material based calculations have been validated with existing theory and experiments.

Next, we have proposed methods to effectively control current distribution and contact resistance in nanoscale electrical contacts by strategically designing the specific contact resistivity along the contact length [11], [12]. Our study shows that severe current crowding in highly conductive electrical contacts can be effectively reduced by spatially varying the contact layer properties and geometry, or by introducing a thin nanometer or sub-nanometer scale insulator layer between the contacting members. Most importantly, we demonstrate that the current crowding effects in nanoscale electrical contacts can be mitigated while maintaining similar total contact resistance [11].

Future work on the current distribution and contact resistance may include the effects of various contact geometry, insulator layer non-uniformities and AC response. One may also investigate the role of capacitance and inductance in nano-scale contact structures. It would be interesting to study the time-dependent dynamics of such junctions, especially when a large contact resistance is coupled with the reactive elements. Our transmission line model is assumed to be two-dimensional, where the effects of transverse dimension are neglected. This issue might be included in future studies. Although widely used, TLM is only a simplified approximation of the practical electrical contacts, where the current crowding and fringing fields near the contact corners cannot be fully accounted for. The impacts of the finite interfacial layer thickness and the possible parallel current components in the interface layer, are also ignored. To accurately quantify these effects, field solution methods need to be incorporated. In the future, one may also extend this work to a contact structure with multiple interfacial layers with anisotropic material properties. Coupled electrical-thermal transport across nanoscale electrical contacts may also be analyzed with the effects of temperature-dependent electrical and/or thermal conductivities.

REFERENCES

REFERENCES

[1] S. Banerjee and P. Zhang, "A generalized self-consistent model for quantum tunneling current in dissimilar metal-insulator-metal junction," *AIP Advances*, vol. 9, no. 8, p. 085302, Aug. 2019, doi: 10.1063/1.5116204.

[2] P. Zhang, "Scaling for quantum tunneling current in nano- and subnano-scale plasmonic junctions," *Scientific Reports*, vol. 5, p. 9826, May 2015, doi: 10.1038/srep09826.

[3] P. Février and J. Gabelli, "Tunneling time probed by quantum shot noise," *Nature Communications*, vol. 9, no. 1, p. 4940, Nov. 2018, doi: 10.1038/s41467-018-07369-6.

[4] M. Uiberacker *et al.*, "Attosecond real-time observation of electron tunnelling in atoms," *Nature*, vol. 446, pp. 627–632, Apr. 2007, doi: 10.1038/nature05648.

[5] G. Nimtz, "Tunneling Confronts Special Relativity," *Foundations of Physics*, vol. 41, pp. 1193–1199, Jul. 2011, doi: 10.1007/s10701-011-9539-2.

[6] K. K. Thornber, T. C. McGill, and C. A. Mead, "The Tunneling Time of an Electron," *Journal of Applied Physics*, vol. 38, pp. 2384–2385, Apr. 1967, doi: 10.1063/1.1709888.

[7] S. Banerjee, J. Luginsland, and P. Zhang, "A Two Dimensional Tunneling Resistance Transmission Line Model for Nanoscale Parallel Electrical Contacts," *Sci Rep*, vol. 9, no. 14484, pp. 1–14, Oct. 2019, doi: 10.1038/s41598-019-50934-2.

[8] S. Banerjee, P. Y. Wong, and P. Zhang, "Contact resistance and current crowding in tunneling type circular nano-contacts," *J. Phys. D: Appl. Phys.*, vol. 53, no. 35, p. 355301, Jun. 2020, doi: 10.1088/1361-6463/ab8fe0.

[9] S. Banerjee, L. Cao, Y. S. Ang, L. K. Ang, and P. Zhang, "Reducing Contact Resistance in Two-Dimensional-Material-Based Electrical Contacts by Roughness Engineering," *Phys. Rev. Applied*, vol. 13, no. 6, p. 064021, Jun. 2020, doi: 10.1103/PhysRevApplied.13.064021.

[10] Y. S. Ang, H. Y. Yang, and L. K. Ang, "Universal Scaling Laws in Schottky Heterostructures Based on Two-Dimensional Materials," *Phys. Rev. Lett.*, vol. 121, no. 5, p. 056802, Aug. 2018, doi: 10.1103/PhysRevLett.121.056802.

[11] S. Banerjee, J. Luginsland, and P. Zhang, "Interface Engineering of Electrical Contacts," *manuscript under review*, 2021.

[12] P. Zhang, S. Banerjee, and J. Luginsland, "Tunneling Electrical Contacts," Patent US 10,755,975 B2, Aug. 25, 2020.